Imperial College London

Department of Electrical and Electronic Engineering

Ambient RF Energy Harvesting and Efficient DC-Load Inductive Power Transfer

Manuel Pinuela

July 2013

Supervised by Dr Stepan Lucyszyn

and Dr Paul D. Mitcheson

Submitted in part fulfilment of the requirements for the degree of

Doctor of Philosophy in Electrical and Electronic Engineering of Imperial College

London

and the Diploma of Imperial College London

Declaration

I herewith certify that all material in this dissertation which is not my own work has been properly acknowledged.

The copyright of this thesis rests with the author and is made available under a Creative Commons Attribution Non-Commercial No Derivatives licence. Researchers are free to copy, distribute or transmit the thesis on the condition that they attribute it, that they do not use it for commercial purposes and that they do not alter, transform or build upon it. For any reuse or redistribution, researchers must make clear to others the licence terms of this work.

Manuel Pinuela

To my (l/w)ife Holda

Acknowlegements

I want to thank my supervisors Dr Stepan Lucyszyn and Dr Paul D. Mitcheson for their, time, help and advice during my PhD. Thanks to their exceptional expertise and complementary skills I was able to get to where I am. I want to also thank them for inviting me to work on their projects and for giving me so many opportunities that have made my time at Imperial an enriching experience. Thanks to Dr David C. Yates for all his time and dedication to my research. I am greatful for their passion to discuss, even the smallest of details, ideas. I would like to thank them for their support on my extracurricular activities on trying to commercialise the technology we developed.

Special thanks to Lord Paul Drayson for believing in this technology and for his support and advice through the last part of my PhD. Also, for sharing his experience and for his dedication to drive our technology forward.

I want to express my gratitude to Dr Ahmad Munir, Dr Tzern Toh, Susan Brace, Pit , Taz, Dr Aifric Delahunty, Will, Mario, Dr Edward Davies, Dr Kaushal Choonee and the rest of the Optical and Semiconductor Devices Group for their technical and administrative help and, more importantly, for not losing hope that I would join them some days at the pub.

I am grateful to the Mexican Council of Science and Technology and Mexican taxpayers for providing financial support during my PhD.

I want to thank my parents for setting my education as a priority and dedicating all their efforts into my upbringing. I want to thank them for listening to my problems and for providing all the tools that I need to have a fruitful life. I am grateful to my brother, who has always believed in me and for reminding me about my passions

and commitments. I thank him for the time he has dedicated to be with me and his infinite insistence in making me a better engineer. Finally, I appreciate that he shares his dreams with me and invites me to be a part of his life.

Thanks to Gaby, Chango, Pedro, Jose Luis, Bea, Cesar and Esther for their friendship and for the great trips and parties we have shared. I also want to thank my grandparents and all my family (Piñuela Rangel / Purón Zepeda) for their continuous support during the last years.

Finally, I have been very lucky to find my wife Holda. I want to thank her for leaving the job she loved to pursue a PhD with me in a different continent, leaving friends and family behind. I appreciate her patience and always attentive ear with my never ending speech regarding wireless power transfer and harvesting. I thank her for being with me in the many difficult situations that I lived during the last years and for always helping me put things into perspective. I am grateful for her critic eye in every important step in my life and for motivating me to tackle bigger and bigger challenges. But most importantly, I thank her for the love and support which has taken me to where I am today.

Abstract

This thesis analyses in detail the technology required for wireless power transfer via radio frequency (RF) ambient energy harvesting and an inductive power transfer system (IPT). Radio frequency harvesting circuits have been demonstrated for more than fifty years, but only a few have been able to harvest energy from freely available ambient (i.e. non-dedicated) RF sources. To explore the potential for ambient RF energy harvesting, a city-wide RF spectral survey was undertaken in London. Using the results from this survey, various harvesters were designed to cover four frequency bands from the largest RF contributors within the ultra-high frequency (0.3 to 3 GHz) part of the frequency spectrum. Prototypes were designed, fabricated and tested for each band and proved that approximately half of the London Underground stations were found to be suitable locations for harvesting ambient RF energy using the prototypes.

Inductive Power Transfer systems for transmitting tens to hundreds of watts have been reported for almost a decade. Most of the work has concentrated on the optimization of the link efficiency and have not taken into account the efficiency of the driver and rectifier. Class-E amplifiers and rectifiers have been identified as ideal drivers for IPT applications, but their power handling capability at tens of MHz has been a crucial limiting factor, since the load and inductor characteristics are set by the requirements of the resonant inductive system. The frequency limitation of the driver restricts the unloaded Q-factor of the coils and thus the link efficiency. The system presented in this work alleviates the use of heavy and expensive field-shaping techniques by presenting an efficient IPT system capable of transmitting energy with high dc-to-load efficiencies at 6 MHz across a distance of 30 cm.

Contents

List of Figures

15

List of Tables

Table of Acronyms

Acronyms

3D	Three Dimensional
3G	Third Generation
4G	Fourth Generation
ac	Alternate Current
ADS	Advanced Design Software
AF	Antenna Factor
AM	Amplitude Modulation
ARPANSA	Australian Radiation Protection and Nuclear Safety Agency
BTx	Base Transmit
BW	Bandwidth
CD	Compact Disk
CDMA	Code Division Multiple Access
CEPT	European Conference of Postal and Telecommunications Administrations
CIE	International Commission on Illumination
CMOS	Complementary Metal Oxide Semiconductor
COTS	Commercial off-the-shelf
CUT	Coil Under Test
dBx	Decibel
dc	Direct Current
DCS	Digital Cellular System
DECT	Digital Enhanced Cordless Telecommunications
DTV	Digital Television

ESR	Effective Series Resistance
EV	Electric Vehicle
EIRP	Effective Isotropic Radiated Power
EMF	Electromagnetic Field
ERP	Effective Radiated Power
FCC	Federal Communications Commission
FEA	Finite Element Analysis
FM	Frequency Modulation
FP7	Framework Programme 7
GaAs	Gallium Arsenide
GIS	Geographical Information System
GPS	Global Positioning System
GSM	Global System for Mobile Communications or Group Special Mobile
HB	Harmonic Balance
HFSS	High Frequency Structural Simulator
HIPERLAN	High Performance Radio Local Area Network
HP	Hewlett Packard
IBM	International Business Machines
ICL	Imperial College London
ICNIRP	International Commission for Non-Ionizing Radiation Protection
IEC	International Electrotechnical Commission
IEEE	Institute of Electrical and Electronic Engineers
IGBT	Insulated Gate Bipolar Transistor
IPT	Inductive Power Transfer
IRPA	International Radiation Protection Agency
ISM	Industrial, Scientific, and Military Radio Band
KAIST	Korean Advanced Institute of Science and Technology
LCD	Liquid Crystal Display
LED	Light Emitting Diode
LTE	Long Term Evolution

MESFET	Metal Semiconductor Field Effect Transistor
MIT	Massachusetts Institute of Technology
MOBESENS	Mobile Water Quality Sensor System
MOS	Metal Oxide Semiconductor
MOSFET	Metal Oxide Semiconductor Field Effect Transistor
MPP	Maximum Power Point
MPPT	Maximum Power Point Tracking
MTHR	Mobile Telecommunication and Health Research Programme
MTx	Mobile Transmit
NCRP	National Council for Radiation Protection and Measurements
NMOS	N-Type Metal Oxide Semiconductor
NRPB	National Radiological Protection Board
OCV	Open Circuit Voltage
OLEV	On-line Electric Vehicle
PA	Power Amplifier
PCB	Printed Circuit Board
PDA	Personal Digital Assistant
PMM	Power Management Module
PMOS	P-Type Metal Oxide Semiconductor
PSU	Power Supply Unit
RCA	Radio Corporation of America
RF	Radio Frequency
RFID	Radio Frequency Identification
RX	Receiver
S	Switch
SMA	Sub-miniature A
SNR	Signal to Noise Ratio
SPS	Solar Power Satellite
SRF	Self-resonant Frequency
TEM	Transverse Electromagnetic

TET	Transcutaneous Energy Transfer
TETRA	Terrestrial Trunked Radio
TV	Television
TX	Transmitter
UAV	Unmanned Aerial Vehicle
UHF	Ultra High Frequency
UK	United Kingdom
UMC	University of Missouri Columbia
UMTS	Universal Mobile Telecommunications System
USA	United States of America
USV	Unmanned Surface Vehicle
v2	Version 2.0
VNA	Vector Network Analyser
WHO	World Health Organization
WiHD	Wireless High Definition
WiMAX	Worldwide Interoperability for Microwave Access
WLAN	Wireless Local Area Network
WPT	Wireless Power Transfer
WSN	Wireless Sensor Networks

List of Symbols

Table of Latin Symbols

a	conductor radius [m]
A	coil cross sectional area [m^2]
A_{link}	link gain
A_{real}	antenna aperture [m^2]
A_{TX}	voltage gain between receiver and transmitter
c_λ	circumference to wavelength ratio
C_g	gate MOS capacitor [F]
C_j	capacitor junction capacitance [F]
C_{oss}	MOSFET output capacitance [F]
C_p	parasitic capacitance [F]
C_{par}	parallel capacitor [F]
C_{resRX}	receiver resonant tank capacitor [F]
C_{RX}	receiver resonant parallel capacitor [F]
C_{ser}	series capacitor [F]
$C_{Smoothing}$	smoothing capacitor [F]
$C_{storage}$	storage capacitor [F]
C_x	voltage doubler MOS capacitor [F]
D	separation distance [m]
E	electric field strength [V/m]
f_o	centre frequency [Hz]
$G(fo)$	antenna gain at the centre frequency [dBi]

G_{TX}	transmitter antenna gain [dBi]
G_{RX}	receiver antenna gain [dBi]
k	coupling factor
k_1	coupling factor at Port 1 of VNA
k_2	coupling factor at Port 2 of VNA
I_s	saturation current [A]
I_{DS}	drain-to-source current [A]
l	coil length [m]
L	coil self inductance [H]
L_{app}	apparent inductance [H]
L_{choke}	choke inductance [H]
L_p	parasitic inductance [H]
L_{RX}	receiver self inductance [H]
L_{TX}	transmitter self inductance [H]
n_d	diode ideality factor
n_{Lcoil}	coil inductance ratio
n	link or transfer ratio
N	number of turns
P	power [W]
P_{dc}	average dc power [W]
P_{load}	power dissipated at the load [W]
P_{out}	output power [W]
P_{RF}	input rf power [W]
P_{RX}	power at the receiver [dBm]
P_{TX}	power at the transmitter [dBm]
Q	quality factor
Q_{cap}	capacitor quality factor
Q_L	loaded quality factor
Q_{Lopt}	optimal loaded quality factor

Q_o	unloaded quality factor
Q_{RX}	unloaded receiver quality factor
Q_T	total quality factor
Q_{TX}	unloaded transmitter quality factor
r	coil radius [m]
R	resistance [Ω]
R_{app}	apparent resistive load [Ω]
R_{eq}	receiver equivalent reflected resistance [Ω]
R_{load}	resistive load [Ω]
R_{ps}	total series resistance of TX coil [Ω]
R_{RAD}	coil radiation resistance [Ω]
R_{RX}	transmitter to receiver distance [m]
r_{RX}	receiver coil radius [m]
R_s	capacitor series resistance [Ω]
R_{skin}	coil skin and proximity effect resistance [Ω]
R_{thRX}	lumped thermal resistance of the receiver load [K/W]
r_{TX}	transmitter coil radius [m]
R_v	capacitor video or junction resistance [Ω]
S	power density [W/m^2]
S_{BA}	banded input RF power density [W/m^2]
S_{harv}	volumetric harvester power density [W/m^3]
T	temperature [K]
T_{amb}	ambient temperature [K]
t_c	charge time [s]
t_d	discharge time [s]
T_{ssRX}	receive heat sink state-state temperature [K]
t_{cycle}	charge-discharge cycle time [s]
U_{RF}	input RF energy [J]
U_{dc}	output dc energy [J]

V	voltage [V]	
V_c	capacitor voltage [V]	
V_{cc}	power supply voltage [V]	
V_{dc}	dc voltage [V]	
V_{DCin}	input dc voltage [V]	
V_{DS}	drain-to-source voltage [V]	
V_{gen}	generator voltage [V]	
V_{high}	high output dc voltage [V]	
V_j	junction voltage [V]	
V_{low}	low output dc voltage [V]	
v_{RX}	receiver voltage [V]	
V_{RX}	receiver coil voltage [V]	
V_t	thermal voltage [V]	
v_{TX}	transmitter voltage [V]	
V_{TX}	transmitter coil voltage [V]	
X_C	capacitive reactance [Ω]	
X_L	inductive reactance [Ω]	

Table of Greek Symbols

β_o	wave number [rad/m]
δ	skin depth [m]
η	RF-to-dc conversion efficiency
η_{amp}	amplifier efficiency
η_{ant}	antenna efficiency
$\eta_{dc-load}$	dc-to-load efficiency
η_{driver}	coil driver efficiency
η_{ee}	end-to-end efficiency
η_{e-e}	harvester end-to-end efficiency
η_{filter}	harvester output filter efficiency
η_{link}	link efficiency
η_o	free space impedance [Ω]
η_{PMM}	power management module efficiency
η_{PSU}	power supply unit efficiency
$\eta_{rectenna}$	rectenna efficiency
$\eta_{rectifier}$	rectifier efficiency
$\eta_{regulator}$	voltage regulator efficiency
η_{Zmatch}	impedance matching network efficiency
θ_{RX}	receiver angular misalignment [°]
λ	wavelength [m]
λ_L	wavelength of lowest frequency band antenna [m]
λ_o	free space wavelength [m]
μ	permeability [H/m]
μ_o	permeability of free space [H/m]
σ	conductivity [Ω m]
ΣI	multiband parallel or current summing rectenna array
ΣV	multi-band series or voltage summing rectenna array
ω	angular frequency [rad/s]

ω_d driver angular frequency [rad/s]

ω_o operating angular frequency [rad/s]

ω_{oRX} receiver resonant tank angular frequency [rad/s]

ω_{oTX} transmitter resonant tank angular frequency [rad/s]

Part I

Introduction

1 Introduction

Untethering electric and electronic devices completely, providing wireless data connectivity and power at a distance, would enhance existing technologies and enable future technologies for its widespread adoption. Providing wireless power at a distance would create a new generation of "true" wireless technologies that would increase quality of life. This work will cover radiative and inductive wireless power transfer technologies via ambient radio frequency energy harvesting and inductive resonant coupling, respectively.

1.1 Motivation

Although the advancement of communications and battery technology has allowed many devices to operate without cables, this is only possible for a limited period of time. All wireless devices either require cables to charge a storage unit or require battery replacement. This situation creates problems, such as regularly connecting the so-called wireless devices to the grid or incurring in high maintenance and running costs for changing and disposing batteries that inconveniently have degradation in performance with time. In many situations these problems have deeper repercussions, such as blocking technology adoption (*e.g.* electric vehicles and wireless sensors), or increasing the mortality of a person (*e.g.* implantable heart pumps).

It is clear that efficient ways of transferring power wirelessly at a distance is beneficial for many applications. Not only is it that these solutions need to be efficient, but they need to be convenient and cover a wide range of applications. For these reasons, this work tackles the challenge of providing power at a distance by the use of near and far-field electromagnetic systems. As will be outlined below,

this work will be divided in ultra-low power (tens to hundreds of microwatts) and relatively high power transmission (tens to hundreds of watts).

1.2 Research Questions and Scope

1.2.1 Radiative Wireless Power Transfer

In the radiative wireless power transfer area, work concentrates on harvesting ambient RF energy from already deployed sources and does not consider the use of dedicated transmitters. Therefore, the first question that this work aims to answer is: how much ambient RF energy is available in urban and semi-urban environments? Secondly, is there enough ambient energy to provide useful amounts of power to a load? The sources that are considered as ambient sources are television, mobile phone and WiFi stations or any other radio frequency transmitter available in an urban environment. Frequency bands outside 470-2500 MHz will not be considered due to size constraints and because sources inside this frequency spectrum are the most likely to be available around the world.

To solve these questions, this work starts by describing a city-wide RF spectral survey that was performed in London. The spectral survey covered all the London Underground stations and measurements were taken at a single street level exit. Time stamps and coordinates were also taken for each measurement. Using the measurement's dataset, the band power density across different locations was calculated and four bands with the highest power densities were selected for the design of suitable energy harvesters. In addition, www.londonrfsurvey.org was created to allow access to the dataset and to provide an interactive filter that allows to select the locations with a specific power density where suitable sensitive harvesters could be deployed.

The second question is approached by designing ambient RF energy harvesters that can operate efficiently at the selected bands. All the harvester system blocks need to be analysed and optimized to achieve not only an efficient operation, but to have a system that can start at low power levels and provide enough power to a

load. Given the fact that this work focuses on ambient RF energy harvesters, the system needs to be able to work dynamically at different bands and from fluctuating power levels.

A complete ambient RF harvester needs to be designed and characterized while being powered from already deployed sources. The design will cover all parts of the harvester, from the antenna to the power management module and load. This work will concentrate on measuring the overall system's efficiency and the available power at the load (*e.g.* an LED), therefore, its aim is not to design a full-working sensing node. The aim of this work is to answer the specific research questions that have been outlined above and have a working ambient RF harvesting prototype that can be deployed and work efficiently in an urban environment.

1.2.2 Inductive Wireless Power Transfer

In the inductive wireless power transfer area, work concentrates on providing tens to hundreds of watts to a load at a separation distance of 30 cm. The design constraints and research questions were defined by an FP7 project called MOBESENS. In this project, an unmanned surface vehicle (robotic kayak) should provide power wirelessly to a sensor buoy without the use of a complex mooring system. Based on this, the first questions that need to be solved are: can an inductive power transfer system be capable of transferring up to 100 W of power without a perfect alignment between the transmitter and receiver? Can this be achieved by a lightweight system that can be carried by a kayak? Can the wireless power system work when the transmitter and receiver dimensions are limited and the receiver needs to be smaller than the transmitter?

To solve these questions, this work starts by reviewing previous inductive power transfer designs and analyses all the blocks that form the wireless power transfer system. In contrast to many designs that are reviewed in this thesis, where only a specific building block is optimized, the research presented here will optimize the complete system. By doing this, this work aims to comply with specific design constraints and achieve high efficiencies, while transferring power at a distance.

A suitable coil design will be performed, having the weight and the operation conditions mentioned above as guidelines to achieve a lightweight, yet efficient wireless link design. In addition to the coil design, the power electronics required to transmit power efficiently will be considered and emphasis will be put into designing a circuit that not only achieves a high efficiency on it own, but a circuit that increases the efficiency of the complete system.

1.3 Structure

This thesis will be divided in two main parts to describe the analysis, design and optimization of ambient RF energy harvesters and lightweight and efficient inductive power transfer systems. The thesis is organized as follows:

Part II: Ambient RF Energy Harvesting

- Chapter 1: is an introduction to RF energy harvesting, with an analysis of the RF harvesting system and a literature review covering RF power density measurements, rectenna designs and applications. The rectenna designs will be divided in those working from dedicated sources and those working from already available sources.

- Chapter 2: discusses the London RF Survey methodology and results, defines the largest contributors and defines the power and frequency characteristics of the selected bands for operation.

- Chapter 3: describes single and multi-band RF harvesters that operate in the selected frequency bands. It discusses and analyses the pros and cons of different antennas, rectifying circuits and rectifying devices, as well as their operation from ambient sources. This part concludes with a comparison of ambient RF harvesters with other energy harvesting technologies and highlights the scenarios were RF harvesting could be an alternative for powering ultra-low power devices.

Part III: Inductive Power Transfer

- Chapter 1: covers the history of near-field wireless power transfer and provides a review of the state of the art in inductive power transfer systems. It also presents a system analysis and compares different inductive power transfer systems through several figures of merit highlighting the importance of a system optimization approach to achieve higher end-to-end efficiencies.

- Chapter 2: discusses the theory behind inductive power transfer systems and how to achieve efficient, lightweight and low cost coil designs. This chapter also presents the details of how to characterize high Q-factor coils.

- Chapter 3: This chapter describes the design of a high-frequency, high-power coil driver to maximize the link and overall efficiency of the system. In addition, it describes the integration of the driver and coils and its performance across different misalignment scenarios. Finally, this chapter compares previous systems with the one presented here and discusses the advantages of having a high-frequency inductive power transfer system over lower frequency systems that rely and field shaping techniques.

Finally, this thesis concludes with a summary of the major findings and future work recommendations on both technologies.

Part II

Ambient RF Energy Harvesting

2 Introduction

2.1 History of RF Energy Harvesting

For almost fifty years, far-field radio frequency technology has been used to remotely power systems from relatively large unmanned helicopters [42] to very small smart dust sensors [43] and contact lenses that measure eye pressure [44]. The first RF power transfer system was developed and tested by James C. Brown in a collaboration of Raytheon and NASA. James C. Brown and his team developed the first rectifying antenna, also called rectenna, and achieved an efficiency of 40% by delivering 100 W to an electric rotor at a distance of more than 20 m and a frequency of 3 GHz. This is the moment at which the concept of a rectifying antenna used to convert RF to dc power was born [42]. Fig. 2.1 shows the demonstration of the microwave-powered rotor in October 1964.

Figure 2.1: Electric rotor powered by a 400 W, 3 GHz transmitter at a distance of 20 m. [1].

Since that moment, RF far-field power transfer by radiating sources started to evolve to tackle high power wireless transfer and many different antennas have been

used, as shown in Figure 2.2. The Solar Power Satellite (SPS) concept was introduced in 1968 where power, generated by photovoltaic means in space, is to be transferred via microwaves to an array of rectennas on earth [45]. High power radiative transfer systems continued to be developed between the 70-90s, mainly in SPS and unmanned aerial vehicles (UAV) [46]. This technology evolved from high-power applications to be used, as shown in [47,48], in low power RF transfer with passive radio frequency identification (RFID) technologies [49].

With the development of Schottky diodes capable of operating efficiently without an external bias at tens of GHz, low power rectennas were designed during the 90s [10]. In this work, the GaAs diode was used and characterized at tens to hundreds of mW of input power. A 35 GHz patch antenna was designed and a rectenna efficiency of 29% was achieved for an input power of 120 mW at 35 GHz. Fig. 2.3 illustrates the experiment setup, where a Gunn oscillator was used as the power source. The antenna was placed at the end of a waveguide expander, which increased the cross section of the rectangular waveguide (WR-28).

In the majority of rectennas, a dedicated RF source is used, where the operator may have control over the effective isotropically radiated power (i.e. both transmit power and antenna characteristics), beam pointing and polarization of the RF source; ensuring optimal line-of-sight operation between the source transmitter (TX) and harvesting receiver (RX). Another solution however is to power these devices from ambient RF energy sources, such as television and mobile phone signals, thus removing the need for a dedicated source. As ambient RF levels are lower than those that can be provided by a dedicated RF source, the efficiency of the harvesting system and its minimum start-up power are of critical importance.

In order to assess the feasibility of deploying ambient RF energy harvesters, the available RF power needs to be measured in different locations. Such measurements, in conjunction with knowledge on harvester performance, can then be used to determine the locations at which RF harvester powered devices can be successfully deployed. Several RF spectral surveys, which measure ambient RF power levels from sources such as television and mobile phone base stations, have been previously
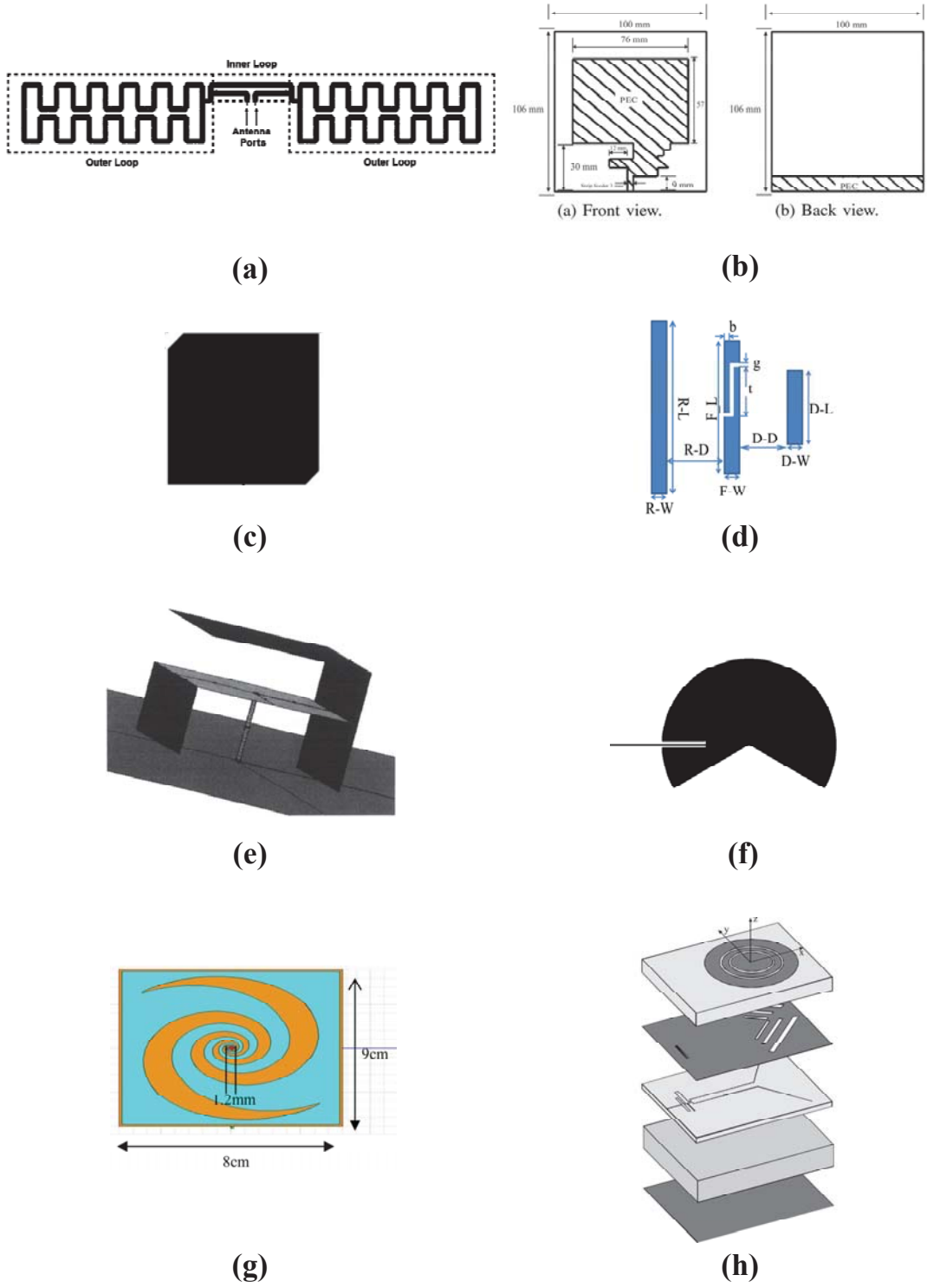
Figure 2.2: Antenna designs used for RF energy harvesting: (a) folded dipole [2], (b) UWB patch [3], (c) truncated patch [4], (d) plannar Yagi Uda [5], (e) folded patch [6], (f) circular sector patch [7], (g) spiral [8], (h) multiband rings [9].
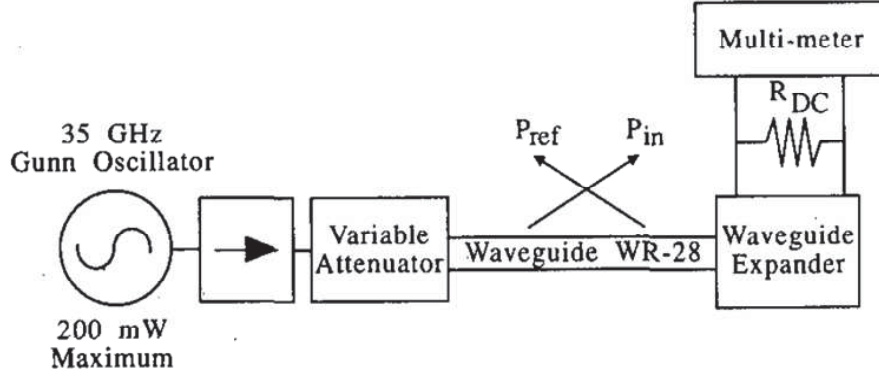
Figure 2.3: Experimental rectenna test setup at 35 GHz. [10].

reported. Many have been undertaken using personal exposimeters or spectrum analysers, where the exact location of each measurement is unknown and with RF power levels only being reported under general scenarios (*e.g.* outdoor, indoor, street, bus, etc.) [50–52]. While being of academic interest for health-related research [53], the lack of power level and specific time/location information limits their usefulness for exploitation in ambient RF energy harvesting applications [54].

Most rectennas (normally comprising an antenna, impedance matching network, rectifier, storage element and load) presented in the open literature have been tested using dedicated sources rather than harvesting from ambient RF energy [48]. In recent years, efficiencies as high as 78% [55] and 90% [56] have been demonstrated with relatively high input RF power levels (i.e. $> +10$ dBm). Moderate efficiencies have also been achieved using dedicated transmitters that provided relatively low input RF power levels; for example, an efficiency of 60% was achieved with -22.6 dBm input power [2]. In one demonstrator [57], designed to operate over a broad range of input RF power levels, (-30 to +30 dBm), the efficiency increased from 5% at a low input RF power to a peak of 80% at +25 dBm. Despite advancements in end-to-end efficiency (*i.e.* input RF to output dc power) at low input RF power levels (similar to those measured in the spectral surveys), only a few attempts at true ambient RF energy harvesting have been reported.

In the next section, the basic building blocks of a rectenna are presented, followed by the previous RF surveys that have been performed across the world. The results from these surveys will then be used to analyse different rectenna technologies pre-

sented in the open literature. Since the aim of this work is to design an efficient ambient RF harvester, the analysis on previous rectenna technologies will focus only on low-power designs. This analysis will be divided in two, rectennas operated by dedicated sources and ambient harvesting rectennas.

2.2 System Analysis

The basic RF harvester design consists of a rectenna, which is comprised of an antenna that acts as a transducer for harvesting electromagnetic radiation, an impedance matching stage, a diode to rectify the input signal and a filter to reject the RF signal from the load, a power management module (PMM) that provides maximum power point tracking (MPPT) and transforms the rectified voltage into a usable voltage levels, a storage element and a load. Fig. 2.4 illustrates the basic building blocks of a rectenna. As will be shown in the next sections, the PMM can be avoided during experiments by having a variable load that can be selected to achieve the maximum power transfer. It is important to highlight that, as in any energy harvesting system, the goal is to maximise the dc power to the load.
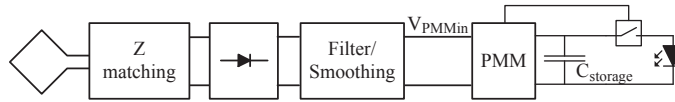
Figure 2.4: RF harvester building blocks.

To fully characterize the complete system shown in Fig. 2.4, the end-to-end efficiency $\eta_{e\text{-}e}$ of all the building blocks, from the available RF power to the load, can be considered as follows,

$$\eta_{e\text{-}e} = \eta_{rectenna}\eta_{PMM} \tag{2.1}$$

$$\text{where } \eta_{rectenna} = \eta_{ant}\eta_{Zmatch}\eta_{rectifier}\eta_{filter} \tag{2.2}$$

where the rectenna efficiency $\eta_{rectenna}$ is the combined efficiency of the antenna efficiency η_{ant}, the impedance matching network η_{Zmatch}, the rectifier $\eta_{rectifier}$ and

the output filter η_{filter}. The efficiency of the optional power management module is η_{PMM}. This work focuses on optimizing the complete system, therefore all system blocks will be taken into account.

Well-defined figures of merit, such as $\eta_{e\text{-}e}$ and $\eta_{rectenna}$, will be used to evaluate complete RF harvester systems and rectennas to allow a straightforward comparison of the different emerging technologies in this field. From the RF harvesting system shown in Fig. 2.4, the rectenna efficiency just describes part of the system's efficiency and does not take into account the PMM. The PMM functionality is a basic building block that needs to be taken into account for any realistic application.

2.3 Literature Review

2.3.1 Available Ambient RF Energy for Harvesting

Concern about health risks surrounding the use of RF signals to transmit information has been a common topic between researchers and the general public for several decades, and has been increasing since the use of mobile phones started to increase [53]. The International Commission for Non-Ionizing Radiation Protection (ICNIRP), together with other regulating bodies such as the National Radiological Protection Board (NRPB), the Institute of Electrical and Electronic Engineers (IEEE), the World Health Organization (WHO), the International Commission on Illumination (CIE), the Federal Communications Commission (FCC), the International Radiation Protection Agency (IRPA), the National Council for Radiation Protection and Measurements (NCRP), the International Electrotechnical Commission (IEC), and others, have created standards to define the maximum transmitted and exposure levels. It is due to these regulating bodies and the interest in health problems related to RF exposure, that many measurements in different conditions and different frequencies have been made. This section will review measurement techniques and measurements of how much RF energy is available for harvesting.

Depending on the goal of the study or survey, a different measuring instrument can be used. There are mainly three types of devices that are used to measure

transmitted RF signals: survey meters, personal dosage exposimeters and spectrum analysers. Survey meters are broadband and used for field measurements. This instrument cannot sense any type of modulation and will measure near-field and far-field signals. New selective frequency response meters have been designed to comply with standards and will display their measurements in a percentage of the limit of that specific frequency standard. Spectrum analysers are narrow band and are more precise for distinguishing the power strength at different frequencies . Due to its narrow-band capability, it can present the added field strength of certain frequencies and display by percentages the energy supplied by each frequency. Personal dosage exposimeters are not very precise but can be used in many environments. These devices sense with more samples than a measurement performed with a survey meter, where only spot measurements are undertaken.

Other factors such as polarization, multipath propagation, modulation, physical environment, response time, dynamic range, and the capability of sensing near-field and far-field signals will have to be taken into account before selecting the best device, or combination of devices for assessing the available RF ambient energy [58]. It has been shown that using all of these devices in the same study might provide a more reliable dataset [59].

This research is interested in man-made, high frequency sources (470-2500 MHz) because they are ubiquitous in many environments and the possibility of achieving small circuits. If a high frequency source is selected, thanks to its short wavelength, the harvesting device will be smaller than if a lower frequency source is selected. Because of this, this review and research will focus on sources with operating frequencies > 0.4 GHz, $i\,e.$ having a free space wavelength of less than 75 cm. Based on studies on the interaction of human tissue and electromagnetic fields (EMF) [58] at different frequencies, ICNIRP published guidelines for exposure level limits based on a tissue damage limit of 40 W/kg and an additional safety factor of 10 [11]. Figures 2.5 and 2.6 show the electric and magnetic field limits for both the general public and occupational exposure, respectively. As is illustrated in these figures from ICNIRP's guidelines, the occupational exposure is always higher than for the general public,

and the peak values are calculated as 32 times the maximum level for frequencies above 100 kHz.
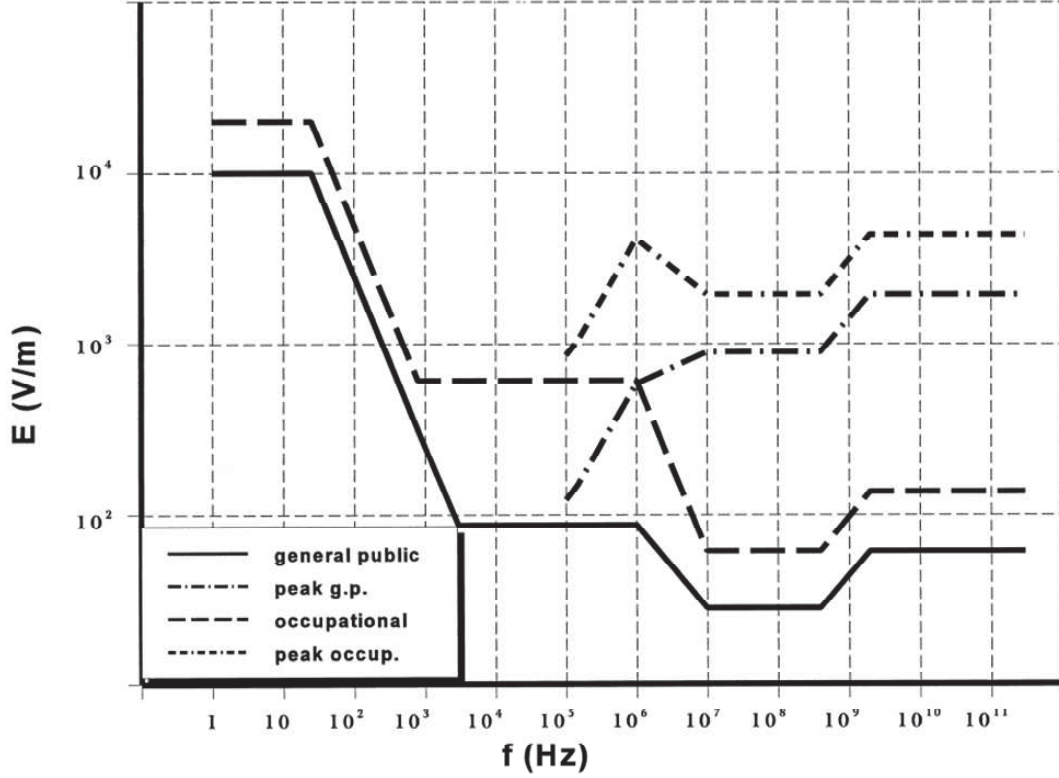
Figure 2.5: Electric field limits for the general public and occupational exposure [11].

For frequencies between 400 MHz and 2 GHz the maximum safe power density in [W/m^2] is calculated by f/200 (f = frequency [MHz]), and for frequencies of 2 to 300 GHz is constant at 10 W/m^2. The WHO published a survey that states the maximum RF power densities should be between 0.002% and 2% of ICNIRP's limits [60], coinciding with [61,62]. These limits are the reference for many measuring devices and telecommunication companies around the world.

Kawahara *et al.* [63] used a Narda Safety Test Solutions SRM-3000 to measure FM, TV, and mobile phone power densities in Tokyo, Japan. This device displays a spectrum of power densities for frequencies between 0.075 to 3 GHz. The measurement of mobile phone signals, between 0.001 μW/cm^2 and 0.17 μW/cm^2, were ubiquitous and with the highest power density of the three sources. Nevertheless, Kawahara *et al.* decided to use FM radio and TV signals because they were more stable, since they do not depend so much on traffic. Mobile phone signals vary depending on
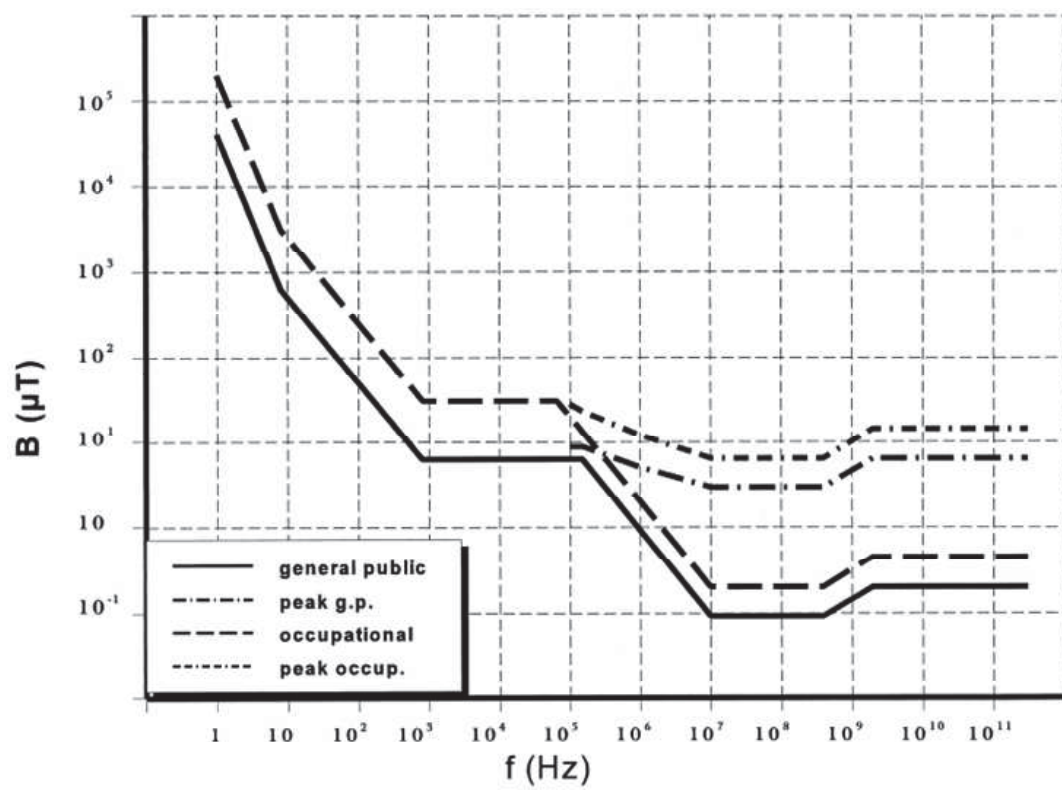
Figure 2.6: Magnetic field limits for the general public and occupational exposure
[11].

the number of users. Power densities of 1 μW/cm^2 were measured at a hundred metres from a radio and TV broadcasting tower. In research in Colorado, USA, RF measurements were taken together with a Global Positioning System (GPS) and a Geographical Information System (GIS), where the NARDA measuring equipment was placed [64]. This allowed the researchers to know exactly the position, altitude, and visibility (if there is line-of-site of the transmitting tower), and correlate these data to the measurements. The RF energy received was from 15 towers with frequencies of 0.083 to 0.6 GHz. Results from 560 measuring stations showed that outside houses the power density was 0.5 μW/cm^2.

As shown by the above surveys, power density levels for signals below 600 MHz tend to be relatively constant, specially if there is line-of-site of the transmitter. For higher frequencies, where mobile phone bands are present, power density levels vary by several orders of magnitude. This was shown in a survey, where spot measurements were undertaken at different distances from GSM base stations. As can be seen in the Fig. 2.7, power densities may vary up to four orders of magnitude at the same distance. This is caused by the different transmitted power levels from mobile phone base stations, spatial conditions, and environmental conditions at the time of the measurement. These variations have to be taken into account when designing and testing the RF harvesting capabilities of rectennas [12]. As seen in this figure, the maximum power densities were measured outdoors and the minimum levels were measured indoors.

Similar measurements were taken at distances of 50 to 200 m and a height of 1.5 m above ground level in five Australian cities, where the maximum measurement of 0.86 μW/cm^2 came from a GSM tower at a distance of 25 m from the transmitter [65].

In another study, a similar variation of measurements at the same distance from the transmitter was recorded using a NARDA SRM-3000 spectrum analyser [66]. Comparison between measurements from GSM and UMTS signals showed that in 85% of measurements, GSM power was higher than UMTS. Median values for GSM power densities were 0.063 and 0.05 μW/cm^2 for UMTS and a power density of 0.016 μW/cm^2 was measured at a distance of 1 km from a UMTS base station [66].
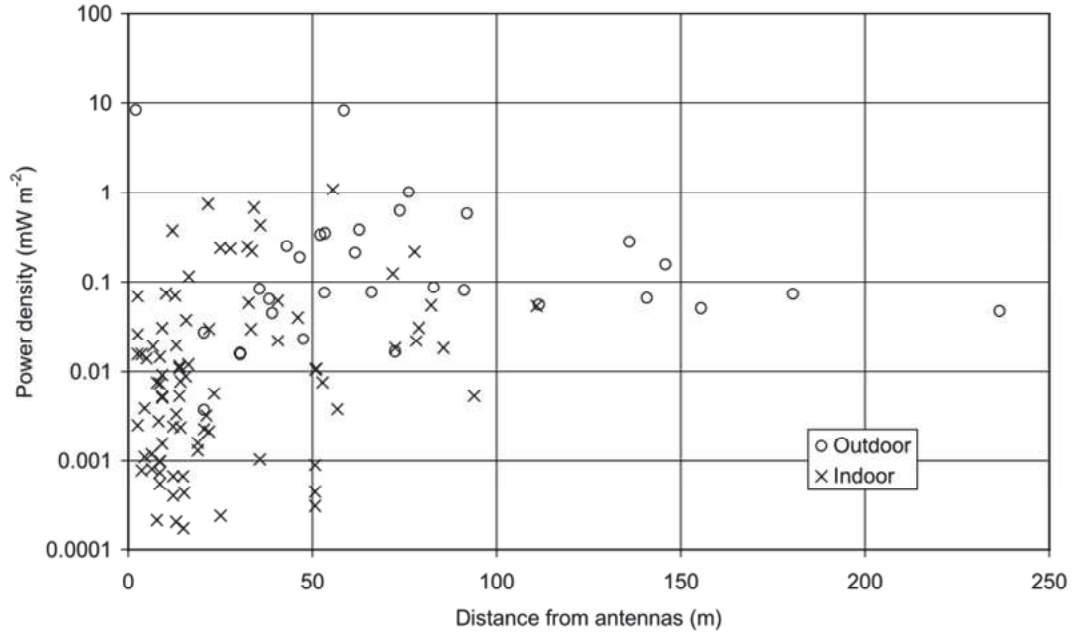
Figure 2.7: Power density measurements vs. distance from transmitter [12].

A study compared measurements undertaken with a spectrum analyser and with a personal exposimeter. Average values from GSM900 and GSM1800 at a distance of 100 to 200 m were 0.025 μW/cm^2 outdoors and 0.013 μW/cm^2 indoors. Since similar variations as discussed in the previous paragraphs were recorded, the use of a personal exposimeter was proposed to record field or power density variations versus time. In the personal exposimeter survey, power received from a GSM downlink while travelling was the highest, with 0.2 μW/cm^2, while office and home environments were 0.04 μW/cm^2 and 0.032 μW/cm^2, respectively [51]. UMTS was the lowest after Digital Cellular System (DCS). The personal exposimeter allowed the study to correlate measurements with the diaries and link the different measurements with locations and daytimes, to give a more clear view of the power densities that can be expected in different situations. A detailed multi-variable regression model for RF exposure prediction was performed in Basel, Switzerland [67]. The model was created using the data collected from 165 participants using a EME Spy 120 personal exposimeter, diary data where daily activities were logged, and a three dimensional model of the area chosen for the experiment. Signals from 0.088 to 2.5 GHz were measured coming from FM radio, TV, mobile phone base stations, Terres-

trial Trunked Radio (TETRA) radio, and Wireless Local Area Network (WLAN). Two models were presented in [67]: a home model, where many details such as having a WLAN router, cordless phone and the type of windows in the house were included; and a total model, where time spent in a train, office, and the street was also included to build a more accurate model. To show the prediction capabilities of the models, the Spearman correlation coefficient was used [67]. The Spearman correlation was useful in this case since it provides higher correlation values to sample variation in the tails of the dataset. Between predicted and measured data for the home and total model the correlation coefficient was 0.65 and 0.75, respectively; showing that the model could be used to predict RF exposure levels for months or years without the need to measure continuously. Power densities of 0.02 to 0.10 μW/cm^2 were measured for both models, but no specific measurements by frequency were given. The values for the power densities were presented as confidence interval percentiles, so for this review the measurements given by this paper are not useful since they do not provide power levels, but it is relevant to show that work on making prediction models for RF exposure is being conducted. In a following research paper by the same group [13], more detailed measurements were performed as a function of frequency using personal exposimeters. As in the previous research, many sources were considered and a weekly average, instead of a daily average as measured by other researches, of 0.013 μW/cm^2 was registered. Of this total average power, Fig. 2.8 shows the percentage provided by each source. Furthermore, this figure illustrates how the power density of the mobile phone downlink frequency band is the source that provides the most amount of power. Also, the highest exposure rates were recorded for people using trains and public transport during daytime.

In [52] power density measurement from mobile phone base stations, specifically GSM900, measurements were recorded in different rural and urban locations both indoors or outdoors. Measurements varied between 0.01 to 0.1 μW/cm^2 at a distance of 25 to 100 m from the transmitting antenna. Contrasting to what was previously cited in [50], energy coming from WiFi signals was one order of magnitude lower than energy from a mobile phone base station. In [68], measurements were performed in-
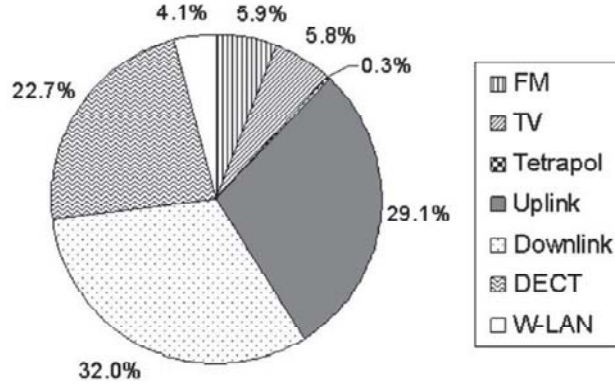
Figure 2.8: Contribution of RF sources to total average RF power during a week [13].

doors and outdoors in rural and urban areas. The range of power densities measured from transmitting GSM, UMTS, and LTE mobile phone base stations was 0.07 to 0.3 μW/cm^2 with an average of 0.05 μW/cm^2, GSM900 being the major contributor with almost half of this energy density. Using the same measuring procedure as in [62], 265 measurements were undertaken in Ankara, Turkey at a distance of 2 to 200 m from a GSM base station [69]. Power densities of 0.0002 to 75 μW/cm^2 were measured from GSM stations operating at 950 MHz, with most measurements under 3.2 μW/cm^2. Power density fluctuations of 0.0001 to 0.1 μW/cm^2 were associated with number of users, white noise, flicker or pink noise, and amplitude drift. Moreover, a comparison between measurements performed with directional antennas and isotropic antennas was undertaken. This comparison showed how power densities with a near-isotropic antenna were bigger than with a directional antenna, because the isotropic antenna received energy from other sources besides GSM base stations. As stated previously, it is important to not only measure the received power, but also the frequency of the received signals in order to know accurately the contribution of each signal to the overall power density at a certain location. Moulder et al. [14] presented measurements that covered 59 antennas and 18 base stations from mobile phone base stations in the UK which were recorded by a previously cited paper by Mann et al. [12]. These measurements are shown in Figure 2.9. The effective radiated power from the base stations was 0.42 to 3.2 kW.

In a 2007 report, published by the Health Protection Agency for the Mobile Telecommunication and Health Research Programme (MTHR), measurements from
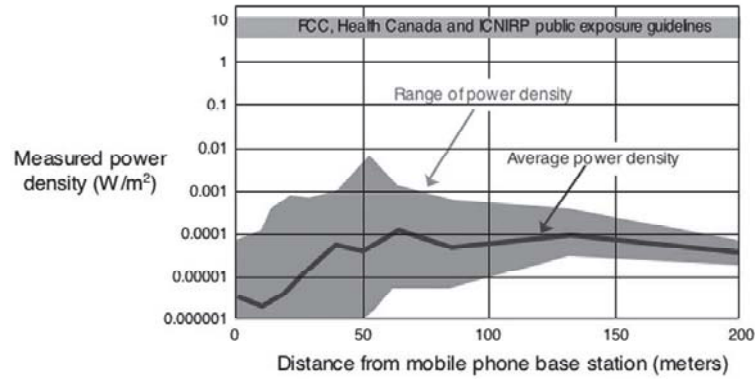
Figure 2.9: Power density vs. distance from mobile phone base stations in the UK compared to the FCC, Health Canada, and ICNIRP limit level of exposure. Data taken from [12]. Graph reported by [14].

microcells and picocells were recorded. Power from microcells at a distance of less than 50 m was higher than power from macrocells, because the wider beam from the microcells would reach ground at a closer distance from the antennas [15]. Power from microcells at more than 50 m from the microcell in public areas was around 0.002 to 2% of ICNIRP's limit value, with a maximum of 8.6% or 43 μW/cm^2 [70]. At larger distances, no significant differences were distinguished between microcells and macrocells because of the effects of other RF signals, and results were similar to Fig. 2.9.
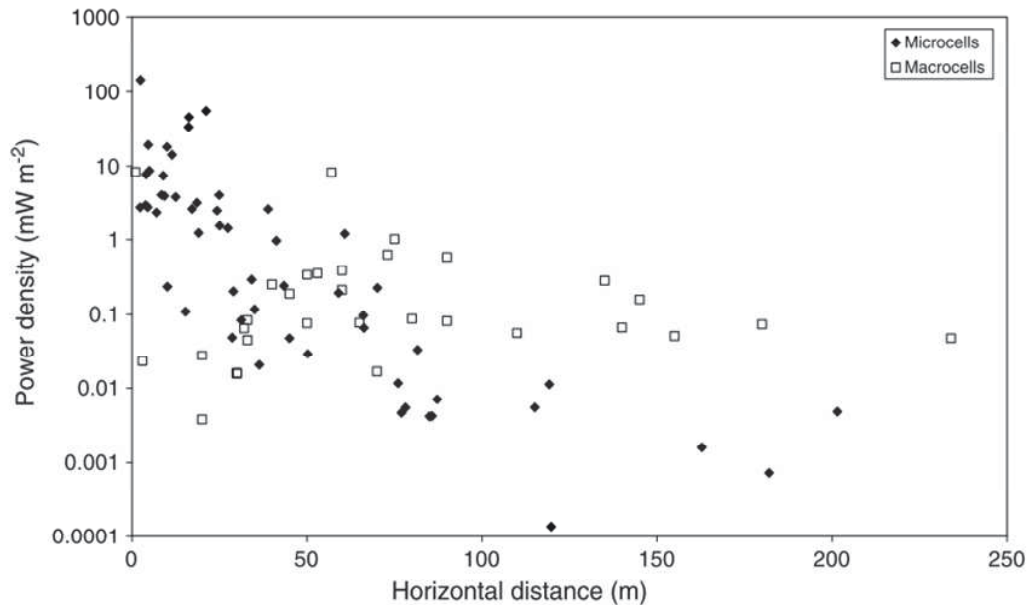
Figure 2.10: Power density vs. distance from GSM microcells and macrocells [15].

Using personal exposimeters, an interesting power density measurement was noticed during RF measurements in France [71]. The data that was collected during the survey showed that even though power densities decreased with an increasing distance from the transmitting antenna, at 280 m from GSM microcells and 1000 m from GSM macrocells there was a peak in power density. This was because at this distance from the transmitting antenna, the beam intersects the ground. As has been corroborated by many studies, the biggest contributor to power densities was GSM with a mean value of 0.003 μW/cm^2. In contrast to other cited studies, no differences between power densities were noticed between indoors and outdoors. Power densities decreased from urban to suburban environments, as well as from suburban to rural.

Wireless local area networks operate in the range of 2.4 to 5.7 GHz and comply with IEEE 802.11 or HIPERLAN2 in Europe. The maximum EIRP (Effective Isotropic Radiated Power) that can be transmitted by a WLAN router is +36 dBm according to the FCC in the US, and from +20 to +30 dBm according to CEPT in Europe. Commercial routers operate around +20 dBm of EIRP [72]. In the Consumer Electronics Show 2010, RCA announced the launch of Airnergy [73]. This device is able, according to RCA, to harvest enough energy from WiFi signals to charge a mobile phone in 90 minutes from 30% of its charge to full charge. Based on the available energy that a standard WiFi source provides, 0.001 to 0.01 μW/cm^2 at a distance of 1.7 m measured with a spectrum analyzer [52], this statement is far from reality and has generated a lot of discussion.

In a very comprehensive research study, measurements from twelve different frequencies with twenty eight different scenarios were undertaken with the DSP120 EME SPY personal exposimeters of Antenessa. After correlating all the date gathered by the personal exposimeters and the diaries filled in by the participants, the following conclusions were made. Among the twenty eight scenarios, the indoor office environment had more energy than the outdoor scenario, thanks to the presence of WLAN and DECT (Digital Enhanced Cordless Telecommunication). In an office, power densities from 0.03 to 0.08 μW/cm^2 were measured from WiFi and 0.02

μW/cm^2 from DECT. In an outdoor environment almost all the energy came from GSM and DCS downlink (communication from tower to mobile phone) with 0.07 μW/cm^2 daytime recording a higher energy than nighttime, because fewer phone calls are performed at night. Although as stated in [74], UMTS can deliver higher values at nighttime. The highest energy was measured in a train or bus, having 0.9 μW/cm^2, with all the energy coming from GSM and DCS uplinks (communication from mobile phone to tower). As expected, an urban environment provided more energy than a rural environment [50].

A similar study with the same personal exposimeter was performed in different French cities with the following results. FM radio sources gave 0.5 μW/cm^2, while WiFi and cordless phone signals where the second highest power source, with 0.38 and 0.36 μW/cm^2, respectively [74]. It is important to note that the personal exposimeter that was used, EME SPY 120, gave a disparity of measurements when the exposimeter was on the body, making the measurements previously cited imprecise. This points to the necessity of performing more work on trying to measure RF power in different microenvironments.

When a WLAN router is experiencing heavy traffic, *i.e.* download or streaming large files (*e.g. videos*, it will transmit more power to cope with the high demand. Measurements were performed with a HP E7402B spectrometer when the access points were transmitting inside an office. The power density ranged from 0.0002 to 1.5 μW/cm^2, with an average of 0.27 μW/cm^2, compared to 0.004 μW/cm^2 in rooms without access points. Similar results were recorded for WiMAX [68]. The measurements from this research, relating to mobile phone signals, will be discussed in the corresponding part of this section.

Finalizing, even though some results differ by one order of magnitude between authors, many of them coincide on the average power available from RF signals. Power density values indoors of around 0.0002 to 1.5 μW/cm^2 are the highest for signals around 0.8 to 2.45 GHz, with an average of 0.27 μW/cm^2 indoors and 0.02 μW/cm^2 outdoors. These values indicate that the mayor constraints of how much energy can be harvested will be dependent on the effective area and the broadband characteris-

tics of the antenna or array of antennas used to collect the available energy, such as those presented in Table 2.1. A more detailed calculation of how much energy this work intends to harvest will be described in Chapter 4.

2.3.2 Dedicated Rectennas

In this section, different rectenna designs that operated with a dedicated transmitter are reviewed. The different designs are organized based on their operating frequency, rather than their achieved efficiency, given the variability of input RF power levels used during simulations and experiments. Besides covering a wide range of frequencies, the review covers a vast range of antennas, rectenna configurations and output power interfaces.

A successful design to decrease the size of a rectenna circuit was implemented by integrating a folded loop antenna rectifying circuit to a total volume of 60 x 80 x.08 mm^3 [75]. The design used an HSMS-285C Schottky diode that has a 0.2 V threshold voltage in a voltage doubler configuration, as shown in Fig. 2.11. In this figure V_{dc} is the output dc voltage, $C_{smoothing}$ is the output capacitor and a resistive load. The circuit operated with an input power of 0 dBm at 925 MHz, at a distance of 0.5 m from the transmitter, with a conversion efficiency of 47%. The input power is the power available at the output of the antenna.
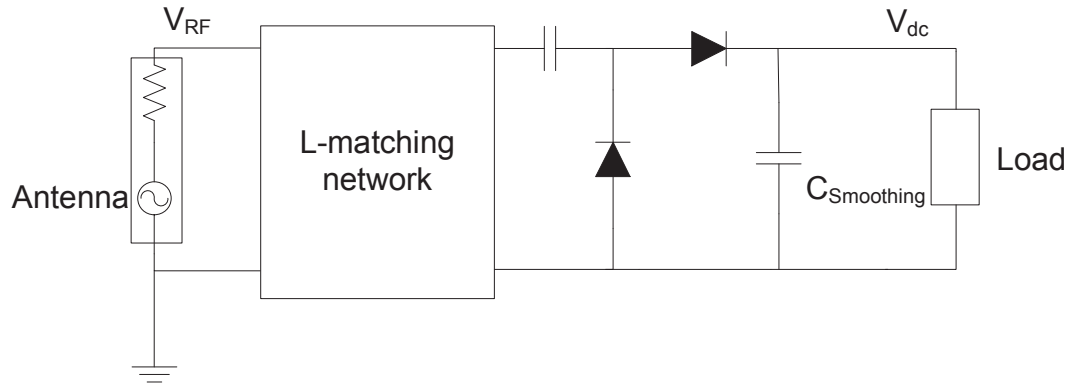
Figure 2.11: Voltage doubler configuration with an L-matching network.

One of the few papers that used RF rectification to power a sensor platform is the one presented in [76]. A 6 x 6 cm^2 dual polarized square patch antenna for the

2.45 GHz ISM band was used to receive incoming RF power from a transmitter that achieved 1 W of transmitted power at a range of 3 to 4 m. By having an integrated design, the boost converter and the sensing platform (thermometer, accelerometer and skin conductivity sensor) were controlled using a MSP430 microcontroller. The microcontroller shut down the boost converter to conserve power after the platform had sensed and transmitted the data. After this, the microcontroller went to sleep to conserve power. The system was able to transmit 2 samples per second with an input power density of 18 μW/cm^2. With this power the rectifying circuit was able to deliver 46.17 μW or -13.4 dBm to a 4 V thin-film lithium battery for full operation of the system.

A complete energy harvesting and data transmission system was designed and tested to work with an input power of -6 dBm (250 μW), at 2.45 GHz, and at a distance of 30 m from the dedicated transmitter [77]. The design uses a 10 x 10 cm^2 patch antenna, series diode configuration and a storage capacitor to store the rectified power, as shown in Fig. 2.12.
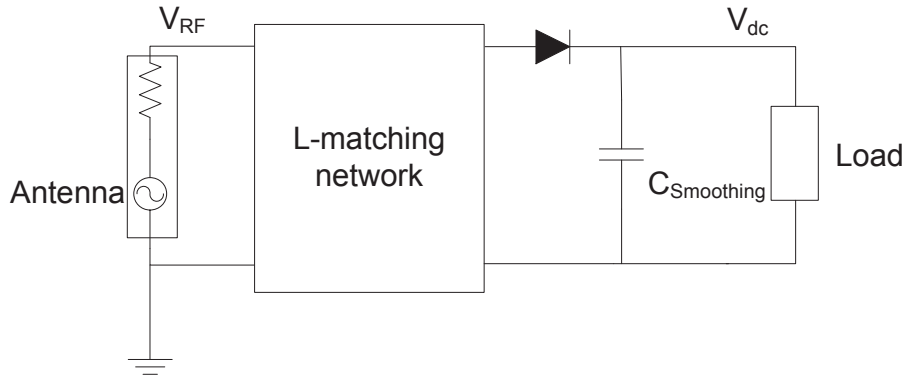
Figure 2.12: Series detector configuration with and L-matching network.

The accomplished distance is quite long, specially if compared to the common RFID devices that work at a maximum of 10 m. A low pass filter between the antenna and the diode helped to impedance match and to block harmonic energy that came from the diodes to the antenna. This simulation proved to be successful and after 50 seconds the 100 pF capacitor was charge to 1.5 V. The data transmission block would only use 10 μW or 4% of the total harvested energy, leaving enough energy to power an image sensor. The rectenna's efficiency was 47% calculated using

the following equation.

$$\eta_{e\text{-}e} = \frac{\textbf{converted dc power}}{\textbf{available RF power}} \tag{2.3}$$

where the available RF power is the power present at the output of the rectenna's antenna and the converted dc power is the power at the load.

In contrast to many rectenna designs, where square patch antennas were used, Itoh *et al.* [7] used a circular sector antenna that rejects second and third order harmonics and a quarter-wavelength transformer to match the shunt diode and antenna impedances. This design is shown in Fig. 2.13. Thanks to this design, the circuit was more efficient than with a square patch antenna because the insertion loss caused by an additional input filter was avoided. The antenna had a resonant frequency of 2.4 GHz and a maximum efficiency of 77.8% with a 150 Ω load and an input power of 10 dBm. The efficiency was defined as the output power divided by the input RF power at the anode of the diode.
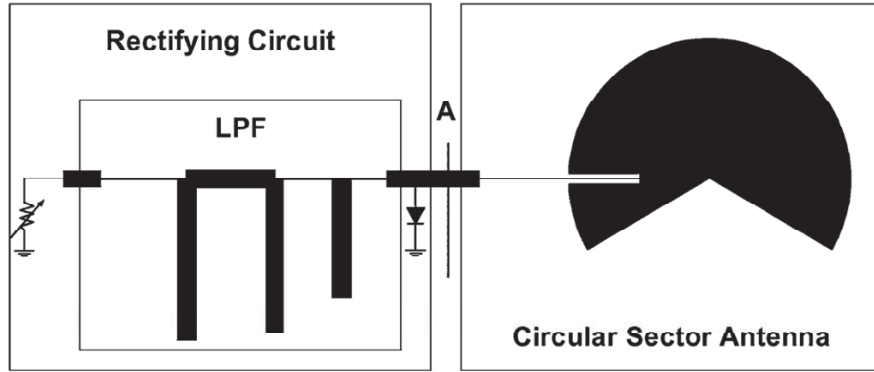
Figure 2.13: Circular patch antenna with harmonic rejection and shunt rectifier [7].

A similar WPT transfer system to the above proved to work at 2.45 GHz, with a transmitted power of 2 W, at a distance of 1.568 m. This was equivalent to a -10 dBm received power from a patch antenna [78]. An ADS diode model was used to simulate accurately low power operation and and impedance matching circuit with a small dc-to-dc converter was placed at the output of the system. The input impedance of the converter was 18 kΩ and a minimum operating voltage of 0.3 V was required for the converter's operation. The converter was able to deliver 7.98

μW or -21 dBm (compared to the simulated value of -22 dBm) to a load of 1 kΩ.

A circular polarized antenna, having two truncated patch antennas, was used to avoid the variation of output voltage due to the rotation of the transmitter or receiver. Moreover, a band pass filter was included to eliminate up to third order harmonics and avoid re-radiation. Also, a series and a shunt diode configuration were compared [4, 79]. The series configuration, with two diodes as shown in Fig. 2.14, had at least twice the output voltage of the shunt configuration. To increase the power at the load, a variable load was used across several input power levels. The maximum conversion efficiency that was achieved was 82%, at a received power of 17 dBm (50 mW) and a frequency of 5.8 GHz. Maximum power transfer was also was also used to achieve a 62% efficiency with an input power of 10 mW at 5.8 GHz and a 533 Ω load. A similar design was used by Fujimori *et al.* [80] and it was noted that 30% of the total input power was lost in the diode.
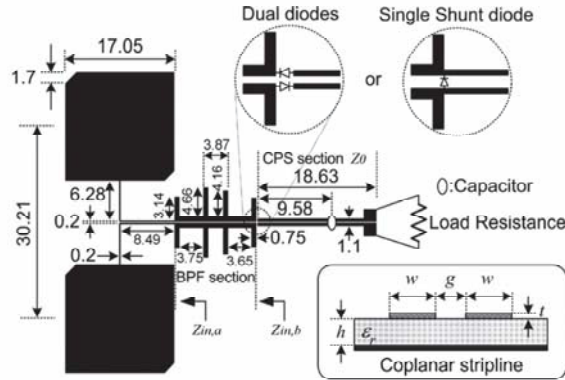
Figure 2.14: Dual-diode, and single shunt rectenna in coplanar stripline [4]

In a highly cited paper, McSpadden *et al.* [81] selected an operating frequency of 5.8 GHz for the smaller component sizes. The rectenna had a low-pass filter and an impedance matching circuit. The system was tested placing the rectenna in front of a waveguide expander (WR-137) and a conversion efficiency of 75% was accomplished with a 326 Ω load and an input power of 55 mW. A dipole antenna proved to be good at receiving power at different angles. But, in a recent rectenna design by the same team, a stepped-impedance dipole was used to reduce the size of the antenna by 23%, achieving a similar conversion efficiency in the complete 5.8 GHz ISM band [82].

In another high power rectenna design, a MESFET was used as a rectifying element, instead of a Schottky diode, due to its high power handling capabilities (>20 dBm) [16, 83]. A self-biased configuration allowed the source gate channel to work as a detector, without the use of an external voltage. Low pass filters before and after the transistor concentrated all the energy of the system in the transistor, to increase rectification efficiency to 62% at 5.8 GHz with an input power of 29.4 dBm. The design shown in Fig. 2.15, as well as the three previously cited designs, were used for high output voltage rectennas for space power transmission or with dedicated transmitters. Therefore, they do not apply to low power density applications. However, they provide a good source for references and ideas that can be applied to low power rectification.
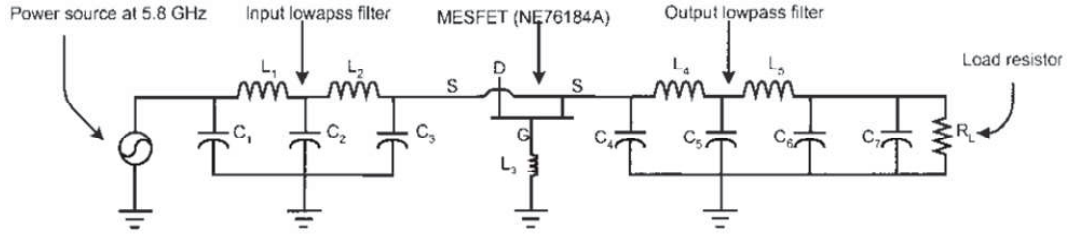
Figure 2.15: Self-biasing MESFET rectifying circuit [16]

2.3.3 Ambient Rectennas

As previously stated, rectennas powered by ambient energy need to apply very efficient impedance matching circuits and techniques to achieve maximum power point tracking. In contrast to a rectenna working with a dedicated transmitter, maximum power point tracking needs to be implemented since distance to transmitter and input power is unknown and highly variable. It is key in ambient RF harvesters to achieve the latter with low loss and low power system blocks that can perform under input power levels as low as tens of microwatts.

For example, one of the most successful attempts of harvesting ambient RF energy utilized a modified omnidirectional patch antenna that had an efficiency of 18% with a single-tone input RF power at -20 dBm [3]. This dedicated signal source was meant to emulate the input RF power levels measured from a nearby DTV transmitter in

Tokyo, but did not take into account the more realistic effect of harvesting from a modulated broadband signal. Another attempt at harvesting ambient RF energy from a mobile phone base station at 845 MHz was reported in [84]. This prototype managed to power an LCD thermometer for 4 minutes, but only after harvesting for 65 hours. In that work, when the authors used a dedicated signal source with a single-tone input RF power at -15 dBm, an efficiency of 3% was recorded. A battery-less location sensor has also been demonstrated [85], powered by a rectenna with a printed antenna on a flexible substrate and a solar cell, although no details for the RF-dc efficiency were reported. Finally, successful prototypes capable of harvesting energy using TV antennas were presented, but again no details of their efficiency were given [86, 87].

One of the first attempts to charge a mobile phone battery with RF energy was made by Harrist [88, 89] in his Master's thesis and patents from the University of Pittsburgh and Powercast, respectively. The design used a quarter wave monopole antenna and a rectifying circuit with a 7 stage voltage doubler connected to a mobile phone charge base. The system was not actually harvesting ambient energy, as in many cases where alleged energy harvesting is implied. In fact, RF signals at 915 MHz were transmitted exactly to the monopole of the system at a distance of a few centimetres. Even though the experiment was successful in charging a mobile phone battery in 4 hours, information of how much energy was transmitted to the system was missing. Therefore, it was impossible to calculate the rectifying efficiency. Using Powercast's wireless power calculator for the P2110 rectenna operating at 915 MHz and at a distance of 4 m, the efficiency of the system is 46.9% for an input power of -2.95 dBm or 507 μW [90].

Far-field RF harvesting was achieved by increasing the input voltage supplied to the rectifying circuit in [2, 91, 92]. This was achieved by a high-Q resonator formed by the antenna and rectifying circuit. With a loaded Q above 20, the input voltage to the rectifier is increased because the passive voltage gain of the resonator is proportional to the loaded Q-factor of the system. The trade-off of achieving a high Q resonator is that the bandwidth is decreased; therefore, this application is not

ideal for ambient RF harvesting, where relatively large channels want to be covered. With a loaded $Q = 35$, the rectenna was able to operate between 902-928 MHz.
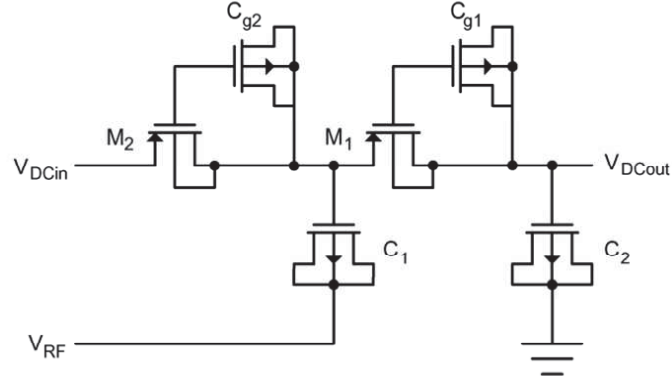
Figure 2.16: PMOS floating gate rectifier voltage doubler [2]

A schematic of the rectifier configuration is shown in Fig. 2.16, where V_{DCin} is the voltage coming from the previous stage, C_g and C_x are MOS capacitors. The floating gate transistors used in the voltage doubler configuration reduced (passively) the threshold voltage of the rectifiers by achieving a gate-source bias, making them better for sensing low power signals. The biasing was achieved by having a high impedance node between the gate of the capacitor and the transistor, therefore trapping charges and creating a fixed bias voltage and reducing the voltage threshold of the transistor. While achieving this, a very good analysis was made of the trade-offs of decreasing the size of the transistors used as rectifiers and the number of stages of the voltage doublers. This research came to a conclusion that a 36 stage design was best. This was achieved taking into account parasitic capacitance and its effect in lowering the Q of the system, thus decreasing the voltage supplied to the rectifying circuit and the conversion efficiency of the system. The latter research team also selected a 906 MHz operating frequency, where RF signals experience less propagation losses than at higher frequencies. They achieved a 15 m distance of operation from the source, being able to harvest signals as low as 5.5 μW or -22.6 dBm to generate 1 V and 0.1 μW. After an hour of operation, enough power was harvested to supply an external circuit with 100 mW for 10 ms. In free space, the same energy was harvested at 42 m from a 4 W EIRP source. This is one of the few attempts where actual outdoor readings have been made.

Another rectenna that worked at low incoming power levels with diode connected PMOS transistors, working at 2.22 GHz, was proposed by Salter, *et al.* [93] from the Laboratory for Physical Sciences at the University of Maryland. Their circuit introduced a low power charge pump (switched capacitor dc-dc converter) between the RF power harvesting stage and the load. The power consumption of the charge pump, 0.5 nW, was a couple of orders of magnitude lower than the harvested energy by the Villard voltage doubler (series capacitor and shunt diode) used in the harvesting block. An improvement of 10 dB of RF energy harvested was recorded, compared to the same system without the charge pump. In this system, the output voltage was dependent on the duty cycle of the charge pump's clock, which made the voltage increase in moments where the current was low. 162 nW of dc power at 1 V through a 5 MΩ load were harvested from just -26 dBm or 2.5 μW. Even though the incoming power was transmitted through a coaxial cable and not through air, via an antenna, the research reported in this letter achieved the highest sensitivity at the lowest incoming power recorded in the open literature. This paper proved that a dc-dc converter might be used in RF energy harvesting, with the trade off of losing small amounts of energy while doing so. It also proved how energy from low power levels, in the range of what can be harvested from mobile phone base stations, could be harvested with a limited collecting area.

Following the above design, a recent paper suggested the use of two Villard doubler cells (Greinacher or Cockroft-Walton) to charge a wireless device, such as a mobile phone if placed near a wireless router or another mobile phone [94]. They stated that the available power for a mobile phone from a base station is around 0.25 to 2 W and that 10 μW with a 50 Ω antenna meant a 32 mV amplitude. Two commercially available quad band antennas were used to harvest energy from 0.400 and 2.4 GHz. Both antennas were matched empirically by varying the value of the matching capacitor. First attempts were undertaken with HSMS-2850 Schottky diodes, at a distance of 2 cm. The second design used a rectifier design with PMOS transistors [93] to simplify the CMOS process. An efficiency of 4% was achieved on simulations at an input power of -5 dBm [94].

In a recent paper, an RF harvesting circuit used to trickle charge a battery for a sensor node was described [95]. A sleeve antenna, having a centre frequency of 2 GHz, a PIN diode voltage doubler , and a capacitor were used to charge the battery from 2.7 to 3.2 V. The input power was 2.79 μW or -25.7 dBm emulating the power that the receiver could detect from a mobile phone base station. The operating range was around 110 m and it took 10 days to get to 3.2 V, to be able to transmit 312 packets of 5 bits in 10 seconds, before starting charging again. They assumed that the reflected power from the rectifier and antenna was zero and this decreased the efficiency to 24.7%, so a low pass filter was needed to suppress this loss. It is important to note this is one of the few teams that tested their system outdoors with similar power densities that would be transmitted by a mobile phone base station.

According to Visser *et al.* [52], an average of 1 μW/cm^2 can be harvested from ambient energy, so very large area arrays need to be designed or a dedicated source must be installed to supply power. In their paper, a 6 x 10 cm^2 folded dipole antenna connected in series was used to harvest energy from a 2.45 GHz transmitter. A boost converter was used to elevate the rectified voltage, to charge a 4.2 V lithium battery. In another work, the research team proposed to place ITO dipole antenna arrays onto windows of buildings [96]. Recently, the same team published a rectenna using a broadband Yagi-Uda antenna that covered all DTV frequencies (475 - 810 MHz) [5]. The rectifier was implemented with a voltage doubler topology and Schottky diodes. Although no indication of the efficiency was presented, the ambient harvester is expected to generate an output voltage of 0.725 V at an input power of -15 dBm.

A 4 x 4 cm^2 antenna array was used to harvest energy at around 2.45 GHz [6]. The antenna design that was used was a folded patch antenna that could work at different frequencies, but had less gain than a narrowband antenna. Using this antenna design, shown in Fig. 2.17, the system was able to harvest more energy from different frequencies. The folded patch antenna had a size of $\lambda/16$ and several designs were simulated using a diode in series and shunt configurations. The shunt configuration proved to be more efficient, although no reasons for this were explained, and the system was simplified by conjugately matching the antenna impedance to the

diode. The operation frequencies were from 2.41 to 2.47 GHz, simulating common sources that would be found in an office environment, such as WiFi and Bluetooth.
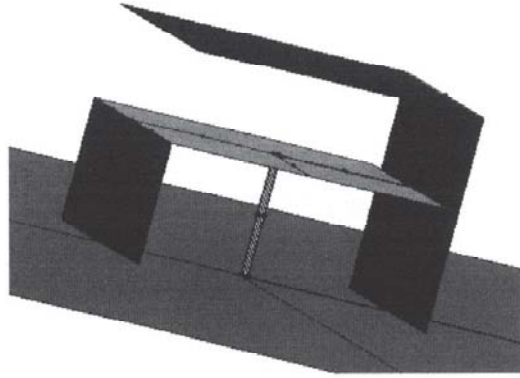
Figure 2.17: 3D folded patch design ($\lambda/16$) [6]

One of the few rectenna designs capable of harvesting energy at different bands was presented by the University of Bologna [97]. A multi-resonator rectenna was simulated to collect energy from mobile phone base stations and WiFi routers. A multiband circular polarized aperture-coupled antenna was selected to resonate at GSM900, GSM1800 and WiFi frequencies. A circular patch with two outer rings that used near-field coupling worked as a three band receiver, using a combination of the three structures for each frequency. A multilayer design allowed the team to include the antenna structures and the rectenna circuitry in the same area. To simulate the incident field on the antenna, which was estimated by combining the antenna characteristics with the reciprocity theorem, they computed a Norton current source equivalent. To optimize the system they ran simulations on each specific frequency with harmonic balance to do a good impedance match. The input power was varied between -16 dBm to 8 dBm and the source was placed at 1 m distance, having a maximum electric field of 20 V/m. The optimal load was 6.3 kΩ and an efficiency of 60% was achieved in the centre of each band, with a voltage doubler using SMS7630 Schottky diodes. The team recently presented the same idea but in a wearable design, with a boost converter and a maximum power point tracking system [98,99]. The system achieve a 45% end-to-end efficiency at 900 MHz and with an input power of 133 μW and 35% at 1750 MHz with an input power of 23 μW.

A broadband and a narrowband rectenna were designed after field measurements

from GSM, WiFi and WiMAX were performed. During these measurements, at frequencies between 0.680 to 3.5 GHz, power densities were between 0.001 to 35.5 μW/cm^2, and the highest constant value was between 1.8 to 1.9 GHz with a power of 0.063 μW/cm^2. A frequency independent spiral antenna with a 100 Ω impedance and an area of 9 x 8 cm^2, was able to harvest a maximum input power of -42 dBm from 1 to 3 GHz. The output dc power was -80 dBm (10 pW). According to the previous measurements, it is important to emphasise that the available harvested power from the environment with this antenna is around -79 dBm. These power levels are very low because of the broadband mismatch of the antenna with the rectifier, so a narrowband antenna with an impedance matching circuit was designed. Both antennas used the same voltage doubler configuration with an HSMS-2850 Schottky diode. The maximum dc power was -64 dBm, with a -42 dBm input power and an RF-to-dc efficiency of 0.6%. It was not specified if the measurements were performed with real ambient sources. According to Bouchouicha *et al.* [8] this power is not enough to continuously energize a WSN node, so a super capacitor was suggested for storing energy.

Georgiadis *et al.* [100] presented a rectenna where a 2.45 GHz dual linear polarized aperture coupled antenna was used to convert RF signals of -20 dBm with an efficiency of 15.7%. The design of the antenna was performed with Momentum and the rest of the system was simulated with the Harmonic Balance tool from Agilent's ADS [101]. To integrate the antenna in the rectenna design, a Thévenin equivalent was calculated by doing transmission simulations of the antenna. The source voltages were calculated using the reciprocity theorem [102]. A maximum input power density of 0.135 μW/cm^2 was equivalent to an input of -20.4 dBm thanks to a directivity of 7.5 dB at 2.45 GHz that corresponded to an efficient area of 67.1 cm^2. The output voltage was between 50 to 90 mV and the physical area of the antenna was 3.4 x 3.4 cm^2.

2.4 Conclusion

This chapter presented how the early applications of radiative RF energy transfer, mainly for defence and security applications, helped develop the theory, initial approaches and challenges of transferring power at a distance. Based on the technology developed on these applications, the main building blocks of an RF energy transfer and, more importantly, ambient RF energy harvester were analysed. This analysis highlighted the importance of designing a system that is capable of achieving high overall efficiencies across a broad spectrum of frequencies and variable input power levels.

As summarized in the literature review, the main design approaches for RF energy transfer and harvesting systems have concentrated on either transferring energy with dedicated sources or collecting ambient RF energy from already deployed sources. Based on the above'mentioned RF surveys, the rectenna and complete harvester systems were analysed to understand the different approaches that have been undertaken around the world to make each of the system blocks, from the antenna to load, more efficient.

Table 2.1 summarizes and compares past and state-of-the-art designs of rectennas and harvester systems. The rows in bold indicate the rectennas and harvesters that were designed to operate under ambient power density levels, although as mentioned before, only a few were tested from already deployed sources. It can be clearly seen that rectennas operating under high input power levels can achieve efficiencies close to 90%, similar to the first RF power transfer attempts. The difficulty arrises when the source is variable in both frequency and power and the rectenna needs to be able to not only work under these conditions, but achieve this while mainting high efficiency with low power system blocks.

The table helps to highlight the main differences between designing rectennas working from dedicated transmitters and ambient sources. Rectennas operating from ambient sources tend to use a rectifier voltage doubler configurations to achieve higher output voltages at the load. This does not mean that this is the best topology for ambient energy harvesting, since only a few comparisons of rectenna topologies

Table 2.1: RF Transfer and Harvesting Systems Comparison

Frequency [MHz]	P_{RF} [dBm]	η_{e-e}	Rectifying Topology	Rectifying element	Antenna	Reference
550	**-20**	**19**	**Series**	**BAT43W**	**UWB Modified patch**	[3]
845	**-15**	**3**	**Voltage doubler**	**HSB276AS**	N/A	[84]
900	**-8.7**	**45**	**Voltage doubler**	**SMS7630**	**Multiband rings**	[99]
906	**-22.6**	**2**	**Floating gate voltage doubler**	**PMOS transistor**	**Folded dipole**	[2]
915	**-2.95**	**46**	**Voltage doubler**	**Schottky**	**Patch**	[90]
925	0	47	Voltage doubler	HSMS-285C	Folded dipole	[75]
1850	**-42**	**0.6**	**Voltage doubler**	**HSMS-2850**	**Spiral antenna**	[8]
2000	**-25.7**	**25**	**Voltage doubler**	**PIN diode**	**Sleeve**	[95]
2200	**-26**	**6.5**	**Voltage doubler**	**PMOS transistor**	N/A	[93]
2400	10	78	Shunt	HSMS-2820	Circular sector patch	[7]
2400	**-5**	**16**	**Voltage doubler**	**NMOS transistor**	N/A	[94]
2450	-21	8	Series	HSMS-2860	Square patch	[78]
2450	N/A	N/A	Series	HSMS-8101	Dual-polarized square patch	[76]
2450	-6	47	Series	N/A	Square patch	[77]
2450	**-40**	**N/A**	**Shunt**	**HSMS-2850**	**Folded patch**	[6]
2450	**-15**	**N/A**	**Voltage doubler**	**HSMS-2850**	**Plannar Yagi Uda**	[5]
5800	16.9	82	Series	MA4E1317	Truncated square patch	[4]
5800	17.4	75	Shunt	Schottky	Dipole	[81]
5800	29.4	62	Shunt	MESFET	N/A	[16]

at ambient power densities have been performed.

Also, Schottky diodes tend to be ideal for harvesting low power density levels but a few rectennas using self-biasing MOSFETS have been designed and have achieved relatively good efficiencies under very low input power levels. Only a few papers explain in detail the selection of their rectifying devices, raising the need for a more in-depth analysis of COTS devices to select the optimal rectifier for a specific set of frequencies and power levels. In addition, patch antennas are used mostly due to their planar design and simplicity, but their directivity constraints their use for ambient harvesting applications. Loop antennas seem to provide several advantages not only for their more omnidirectional radiation pattern but also for their highly tunable impedance. The latter is a very useful characteristic that can decrease losses in the impedance matching network, by conjugately matching the impedance of the rectifier under a specific input power level and frequency.

Based on the findings of this section, a complete dataset of power density levels is required to define which type of antenna, rectifier topology, rectifier element and power management module should be used for harvesting energy from ambient sources. The next sections show how the findings from the literature review prompted the need of a city wide RF survey and the design of an efficient harvesting system. Then, based on these results, rectennas were fabricated and their efficiencies, under ambient RF energy harvesting operation, were calculated using *in situ* field strength measurements. Furthermore, an investigation of multiband rectenna arrays is also presented, demonstrating the trade-offs between series (voltage summing) and parallel (current summing) topologies with the aim of reducing the minimum input power required for harvester operation. Finally, a comparison between measured ambient RF energy harvesting and alternative forms of energy harvesting technologies is presented, highlighting the practical feasibility of exploiting existing, freely available sources of RF energy.

3 London RF Survey

3.1 Introduction

As mentioned previously, to assess the feasibility of deploying an RF harvester in a specific location, the available power density levels need to be measured, since these will define the characteristics and specifications of the harvester. In addition, these levels will constrain the functional characteristics of the harvester, more specifically, they will define the application and the duty cycle at which the latter will operate. It is the goal of this chapter to identify the power density levels present in London to serve as a starting point for the design of an efficient RF harvester.

In order to quantify the input RF power density levels present in a typical urban and semi-urban environment, a city-wide RF spectral survey within the ultra-high frequency (0.3 to 2.5 GHz) part of the frequency spectrum was conducted within Greater London. A number of city-wide RF spectral surveys, as presented in the previous chapter, have previously been conducted, but in general only a few samples were taken, giving little insight into (semi-)urban environments [62, 63, 84]. Other surveys [15, 52] compare their measurements relative to the distance from the nearest transmitter. This type of survey is useful if a direct line of sight can be achieved between the transmitter and the receiver, or if the harvester is going to be placed in an open space. Contrastingly, in a (semi-)urban environment this may not provide enough information about the RF spectrum, since there are likely to be local geographical variations in base station density and propagation characteristics (e.g. multipath effects, reflection, diffraction and attenuation from buildings).

This chapter presents the methodology and instrumentation used to conduct the survey at each station of the London Underground network. Covering all the Un-

derground stations provides a robust dataset for representing Greater London in terms of geographical distribution and population density by having a combination of urban (in the centre) and semi-urban (in surrounding areas) characteristics. Measurements were taken at each of the 270 stations (from a randomly chosen exit, at street level). To provide traceability and for use as a historical reference, time stamps and GPS locations were recorded. In addition, measurements taken inside a building at Imperial College London (ICL) are presented as an example of the density levels available in a typical office block within an urban environment. Finally, this chapter concludes with the statistical analysis of the city-wide RF spectral survey, indicating suitable locations and associated RF bands with sufficient input RF power density levels for harvesting.

3.2 Methodology and Instrumentation

Mobile phone usage varies during daytime and hence ambient RF energy in the mobile phone allocated frequency bands is expected to be time dependant, with more energy available during daytime than at night time. Therefore, in order to be able to make fair comparisons between locations, measurements were taken consistently between 10:00 am and 3:00 pm on weekdays over a period of one month (between the 5th March and 4th April 2012). The measurements were performed at street level at the exit of each of the 270 London Underground Stations, as illustrated in Fig. 3.1.

Figure 3.1: Transport for London Underground map [17].

To record the location and time of each measurement point, a web-based smart-phone application was specifically designed for this survey. The application also ensured that the data that was stored in the database had a location error of less than ±8 m. This database was then correlated with the FieldFox measurements to create the londonrfsurvey.org website, which is presented in the following section.

The electric field strength was measured between 0.3 and 2.5 GHz, using an Agilent N9912A FieldFox RF Analyser [18] with a calibrated Aaronia BicoLOG 20300 quasi-omnidirectional antenna [19], as shown in Figures 3.2 and 3.3. It is important to note that the spectral measurements were undertaken during the analogue-to-digital switchover period in the UK and so the measurements for DTV may represent an underestimate of present RF power levels measured now that the switch over is complete [103]. Also, it should be noted that this survey was conducted prior to the 4G network being switched on within the UK.

Figure 3.2: Agilent FieldFox RF Analyser [18].

Figure 3.3: BicoLOG 20300 omnidirectional antenna [19].

To achieve a calibrated measurement, the 296 calibration points of the BicoLOG antenna were loaded into the FieldFox. Fig. 3.4 shows the antenna factors (AFs) across the antenna's operating frequency range (0.02 - 3 GHz). The antenna factor describes the voltage in the terminals of an antenna in the presence of an electric field. The FieldFox automatically applies the correction factors at each of the frequency points, with a step size between 5 and 10 MHz, and interpolates between steps depending on the resolution of the measurement.
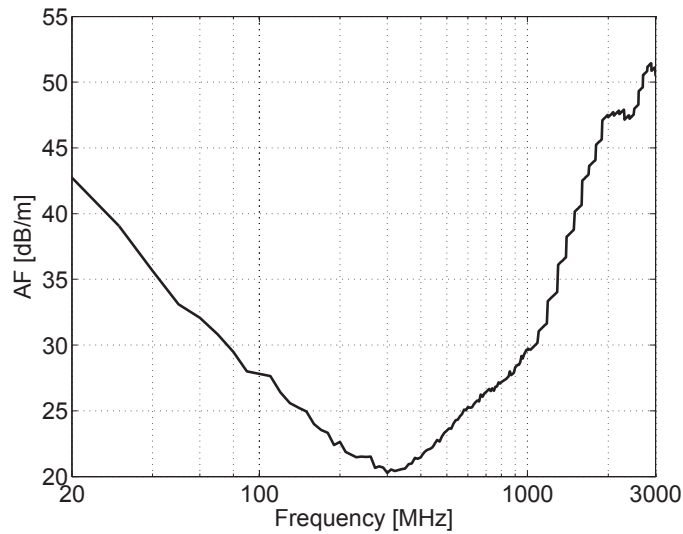
Figure 3.4: BicoLOG antenna factors [19].

A 'panning method', which complies with international regulations for measuring exposure limits, was used [104] [61] [105]. Here, the calibrated antenna is rotated to three orthogonal axes while the spectrum analyser is set to 'max-hold', ensuring that the maximum reading is recorded. It is important to emphasize that since this survey is intended to provide just a reference on the electric field strength levels available in London at a certain point in time, the averaging function was not used. The average measurement of a short and random period of time would not provide a representative value. To have a representative mean value, measurements would need to be taken for several days throughout several months. The latter exceeds the time span and goals of this survey, thus the maximum field strength values were used as a snapshot of the expected spectral conditions that can be present at a certain time and location in London.

More than one minute was allocated for each measurement, to allow for more than three sweeps across the selected frequency range. Allowing for several sweeps provides enough information of the ever-changing signals in each of the frequency channels, as explained in the ICNIRP guidelines. Additionally, to maintain a comparable signal-to-noise (S/N) ratio, attenuation was introduced (with a minimum set at 5 dB) to avoid compression when high input RF power levels were detected. For all measurements the resolution bandwidth was fixed at 100 kHz, the internal amplifier was turned on and the highest resolution of 1001 points was selected. These settings provide the ability to obtain a snapshot of the power density that can be expected in an urban or semi-urban environment from continuously variable sources.

3.3 Survey Results

Based on the survey data points, the available RF power density can be calculated based on the electric field as follows: $S = E^2/Z_o$, where E is the electric field strength (V/m) and Z_o is the free space impedance. Fig. 3.5 shows the input RF power density measured outside the Oval London Underground station, where the spectral bands for DTV, GSM900, GSM1800, 3G and WiFi can been clearly identified.
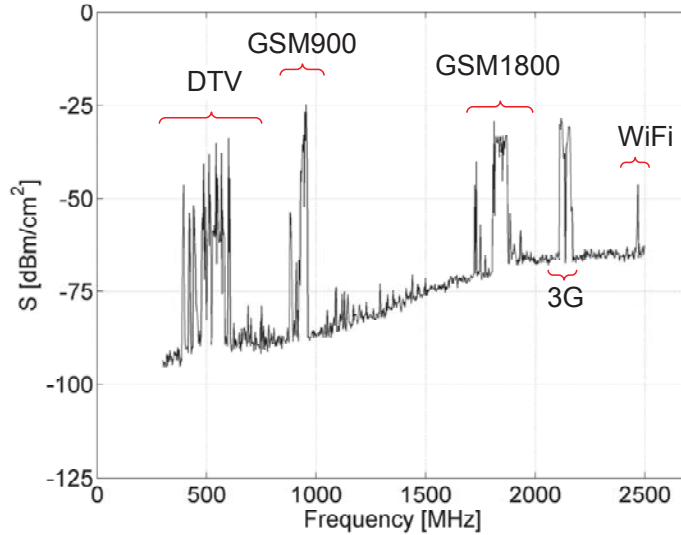
Figure 3.5: Input RF power density measurements outside the Oval London Underground station.

A well designed rectenna should ideally be capable of harvesting energy across

an entire band and thus it is important to calculate the total band power. The banded input RF power density S_{BA} (nW/cm2) is calculated by summing all the spectral peaks across the band (i.e. in a similar way the spectrum analyser calculates channel power). These levels provide a snapshot of source availability at the time and location of the measurement. Moreover, they are used as the harvester design starting point, since the power density at each band will define the impedance of the diode. With the impedance of the diode known, the rectenna can then be designed, as will be shown in the following chapter.

After correlating the timestamp and GPS location with the measured field strengths, the dataset was placed in the London RF Survey website [106]. Fig. 3.6 shows all locations where measurements were taken, together with their GPS coordinates and time stamps. As can be seen, once a point is selected from the map, its field strength or banded RF power density can be selected and displayed.
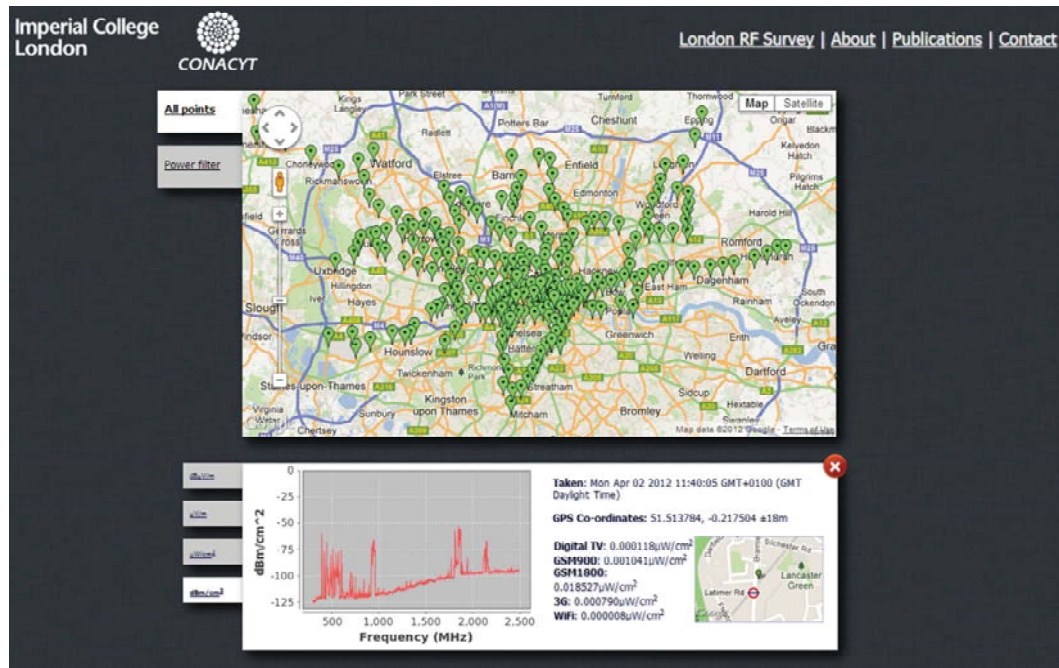
Figure 3.6: LondonRFSurvey.org snapshot with the Latimer Road underground station selected.

71

3.3.1 Frequency Band Selection

The exact frequencies for each band are set by the UK's official frequency band allocation [107]; the GSM900, GSM1800 and 3G base transmit (BTx) bands were separated from the associated mobile transmit (MTx) bands. Table 3.1 shows average RF power levels across all London Underground stations for the banded input RF power density measurements. It can be seen that all base station transmit levels are between one and three orders of magnitude greater than the associated mobile transmit levels. For this reason, and the fact that the population of transmitting mobile phones in close proximity of the harvester is highly variable, only base station transmitters will be considered further.

Table 3.1: Summary of London RF Survey Measurements

Band	Frequencies [MHz]	Average S_{BA} [nW/cm^2]	Maximum S_{BA} [nW/cm^2]
DTV*	470-610	0.89	460
GSM900 (MTx)	880-915	0.45	39
GSM900 (BTx)	925-960	36	1930
GSM1800 (MTx)	1710-1785	0.5	20
GSM1800 (BTx)	1805-1880	84	6390
3G (MTx)	1920-1980	0.46	66
3G (BTx)	2110-2170	12	240
WiFi	2400-2500	0.18	6

During switch over

From our London RF survey, DTV, GSM900, GSM1800, 3G and WiFi were identified as potentially useful ambient RF energy harvesting sources, although DTV appears to be heavily dependent on atmospheric conditions and WiFi is very dependent on user traffic. It should be noted that the mobile phone base station transmitters employ vertically polarized antennas, placing a constraint on harvester orientation in deployment. With DTV, within the UK, the main transmitters have horizontally polarised antennas, while repeater transmitters have vertically polarized antennas.

Using the complete dataset from the London RF survey, Fig. 3.7 shows the average and median of the banded input RF power density measurements for the four largest

ambient RF sources in Greater London. From this figures, it can be seen that more than half of the locations have below average power levels. This is due to the fact that several stations had maximum levels that were considerably higher than the average, because of their close proximity to TV transmitters (e.g. Crystal Palace), extremes in base station density and propagation characteristics.
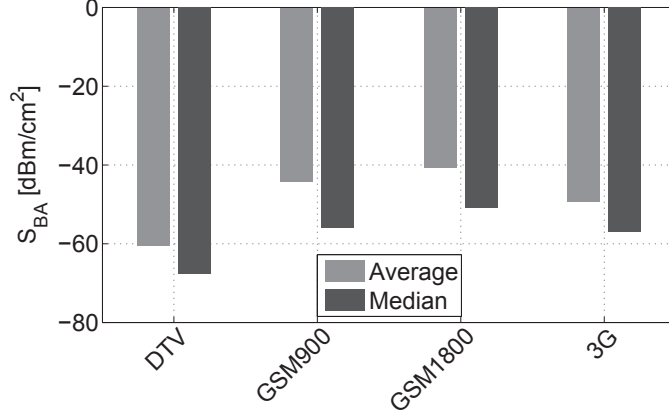
Figure 3.7: Banded input RF power density measurements for the four largest ambient sources in Greater London [20].

3.3.2 Urban and Semi-urban Analysis

It is convenient to define the boundary between urban and semi-urban environments by the line that separates zones 3 and 4 on the London Underground map [17]. As one would expect, the central zones 1-3 host the highest density of base stations. With the use of an interactive filter on the London RF Survey website, the station exits with the highest field strengths can be easily selected and will appear on the map, as shown in Fig. 3.8.

Using the filter, a banded input RF power density threshold is selected to filter the ten London Underground stations with the highest measurements for each band, as shown in Table 3.2. With DTV, the highest recorded measurements were all found within the urban environment. This is because Greater London's main DTV transmitter (at Crystal Palace) is located on the south-eastern boarder of zones 3 and 4 and there are no London Underground stations further south. With mobile phones, more than 50% of the stations were inside the urban environment and those
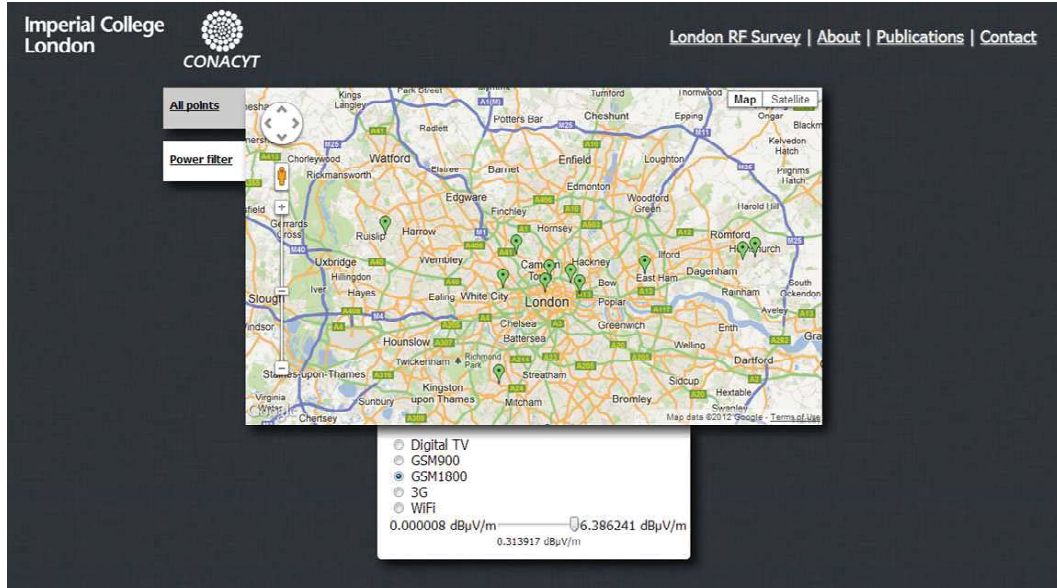
Figure 3.8: Top ten highest GSM1800 field strength locations.

in a semi-urban environment were all located in close proximity to a cluster of base station transmitters.

Table 3.2: Banded Input RF Power Density Threshold: London Underground Stations within Central Zones 1-3 (Urban) and Outer Zones 4-9 (Semi-urban)

Band	S_{BA} Threshold [nW/cm^2]	Number of Stations	
		Urban	Semi-urban
DTV*	40	10	0
GSM900	230	8	2
GSM1800	450	7	3
3G	62	6	4

During switch over

3.3.3 ICL Measurements

In addition to the London RF survey, measurements within the Department of Electrical and Electronic Engineering building, at Imperial College London (ICL), were taken on the 11th floor of the south stairwell. These are shown in Table 3.3. As can be seen, DTV and GSM900 have a higher than average power level (see Table 3.1, due to a near line of sight from the TV transmitter and a close proximity to the 2G GSM900/1800 base stations.

Table 3.3: Measured Banded Input RF Power Densities at ICL

	DTV*	GSM900	GSM1800	3G
S_{BA} [nW/cm^2]	18	48	50	3

During switch over

3.4 Conclusion

In this Chapter the methodology, instrumentation and some of the results of a city-wide spectral RF survey were presented. The collected data showed that the mobile transmit power is several orders of magnitude lower than the one measured from the base station transmitters. This prompted the selection of BTx over MTx for the mobile phone bands. It is important to emphasize, that this situation can be drastically different for applications where a mobile phone is used to power an RF harvester, meaning that the phone and harvester would be required to be less than 5 m apart.

Based on the average measured power levels, DTV, GSM900, GSM1800 and 3G were selected as the the four highest contributors in an urban and a semi-urban environment. For all these bands, the maximum power levels were more than twenty times higher than the average power level, showing a high variability between locations. This is due to the multipath and reflection characteristics of each location. This conclusion strengthens the initial thesis that in an urban and semi-urban environment, distance to the transmitter might not provide all the necessary information required to estimate the available power density levels.

To analyse the difference between an urban and a semi-urban environment, in terms of available RF power, a threshold was selected to filter the stations with the highest power levels. This analysis demonstrated that more than 50% of the highest power density levels were measured in an urban environment. Furthermore, by looking into the location of transmitters near the filtered semi-urban locations [108], it was seen that all of these stations were placed near a cluster of transmitters.

The dataset from the London RF survey, with all relevant information (e.g. locations, timestamps and banded input RF power density measurements), can be

found at the interactive website: www.londonrfsurvey.org [106]. The londonrfsurvey.org website is open source and the collected data can be used as a reference not only for the design of RF harvesters in London, but as a reference for urban and semi-urban ambient RF harvester designs in other cities around the world. Additionally, this website provides critical information for health-related electromagnetic exposure research and the general public.

These measurements, together with the ones taken at Imperial College London are an essential starting point for the design of efficient harvesters, as is presented in the following Chapter. The dataset collected during the survey can also be used to identify other locations in Greater London, where a tested harvester might work by comparing the test's spectral conditions with other survey points. The harvester design procedures and prototype test measurements are presented in the following Chapter.

4 Single-band and Multi-band Harvesters

4.1 Introduction

In order to implement efficient ambient RF energy harvesters the operation conditions, such as the environment (indoor, outdoor, urban, semi-urban or rural), polarization, elevation and most importantly, available RF power density levels, are required. In addition, since the goal of this work is to design harvesters capable of operating in an outdoor urban and semi-urban environment from non-dedicated RF transmitters, the previous chapter showed the results of a city-wide survey performed in London. Furthermore, measurements at Imperial College London were also recorded and a comparison between the performance at ICL and the expected performance across London is presented in this chapter.

Based on the survey measurements, a confident estimate of the total input RF power per band can be performed in hand with the harvester antenna characteristics. Since the location of the transmitter is unknown and reflections and multipath are common, as the survey analysis showed, an omnidirectional antenna is desired. This chapter presents the antenna selection and design framework for an easy to fabricate and scalable antenna. The benefits and characteristics, as well as the drawbacks, of using the selected antenna topology are highlighted and a thorough comparison between full-wave 3D electromagnetic simulations and measurements is also presented.

With the antenna designed and characterized, the total input power can be calculated for each of the selected operation bands. Since the frequency and power

will define the impedance of the diode, the impedance matching between the antenna and the rectifier can be simplified. This is another reason why it is crucial to know the available power density levels when harvesting ambient RF signals. In this chapter the diode selection is presented based on the component characteristics and performance across a wide range of frequencies and for the expected power levels per band. In addition, several detector topologies are analysed and conclusions of the topology selection are presented.

To prove the correctness of the selected diode and detector topology, several impedance matching networks are presented for a single band detector. Simulations and experimental measurements of all the single banded detectors are shown, demonstrating the operation of an ambient RF harvester with a high end-to-end efficiency, including the power management block. This power management block is capable of performing maximum power point tracking, as well as battery management, and was used throughout simulations and measurements to showcase the end-to-end efficiency of a complete RF harvesting system.

To finish this chapter, analysis and measurements of multi-band harvesting architectures, capable of operating at lower power levels than the single-band prototypes, are presented. This section presents the findings of experimental work performed in series and parallel connected harvester architectures and highlights the benefit of each circuit as well as their limitations. Finally, a power density comparison between different harvesting technologies is presented, demonstrating that ambient RF harvesting is an alternative solution for certain applications, where vibrations, thermal gradients or light are not readily available.

4.2 Antenna Design and Measurements

Since the harvesters are intended to operate within a general (semi-)urban environment, where the exact location of the TX source is unknown, the rectennas' or harvesters' antennas need to be as close to omnidirectional as possible, avoiding the need for beam-pointing during deployment. This is at the obvious expense of limited antenna gain and, therefore, the corresponding levels of input power P_{RF} that

the rectifier can receive. Conversely, if the location of the TX is known, it may be tempting to use a high gain antenna, but this would require an appropriate level of beam-pointing and polarization matching that can be established and maintained. Another requirement is that the antennas need to be easily scalable across all frequency bands, since one important objective for this work is to compare and contrast differently banded harvesters. Finally, the antennas need to be easily fabricated. For all these reasons, a rectangular loop was selected, although a monopole would also be suitable [109].

To simplify impedance matching from a standard 280 Ω half-wavelength folded dipole [110] and the rectifier (which, for experimental simplicity and the fact that the harvester is going to be modular, was set to 50 Ω), a modified rectangular loop was used to obtain the required 50 Ω reference input impedance. As presented in [111], a balun does not need to be employed to transition from a balanced to and unbalanced circuit, as there is no significant degradation in performance for this particular application, even with the use of an unbalanced microstrip rectifying circuit. It is important to note that this only applies if the antenna is conjugately matched to the rectifier circuit. Furthermore, the antenna was not integrated onto a substrate, to give the additional freedom to embed the harvester on windows or within walls, furnishings, fixtures or fittings. To achieve this, two different antennas were fabricated for each band; one made using 560 μm diameter copper wire and the other with 75 μm thick, 25 mm wide copper tape. The fabricated antennas are shown in Fig. 4.1. Since the copper tape was not rigid enough to retain its shape, it was placed on a Perspex substrate, to represent a flat panel.

To design the antennas, full-wave 3D electromagnetic simulations were performed using CST Microwave Studio. As discussed previously, the antennas were designed to be as omnidirectional as possible, while covering as much of the ambient RF source bandwidth as possible. Figures 4.2 and 4.3 show the H-plane cut of the modified folded dipoles for the GSM900 band. As can be seen, although the radiation pattern is symmetrical, the antennas cannot achieve a full omnidirectional pattern. The nulls can be seen clearly for $\theta = 0°$ and $180°$. Although not ideal, this antenna
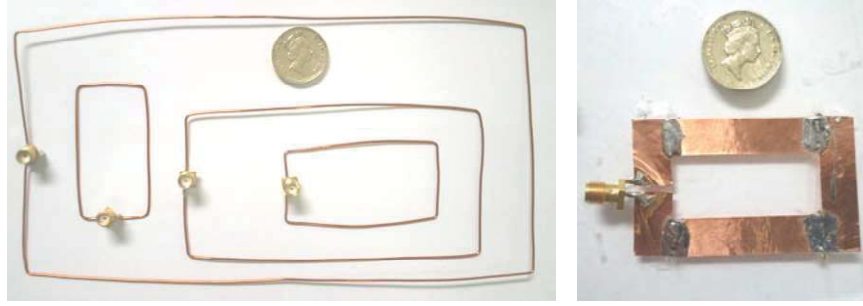
Figure 4.1: 50 Ω rectangular loop antennas shown next to a British one pound coin: (left) DTV, GSM900 (BTx), GSM 1800 (BTx) and 3G (BTx) copper wire antennas; and (right) 3G (BTx) copper tape antenna on Perspex

provides a more suitable radiation characteristic than a directional antenna, such as a square patch. As expected from Maxwell's equations, the same radiation patters are present for all frequency bands.
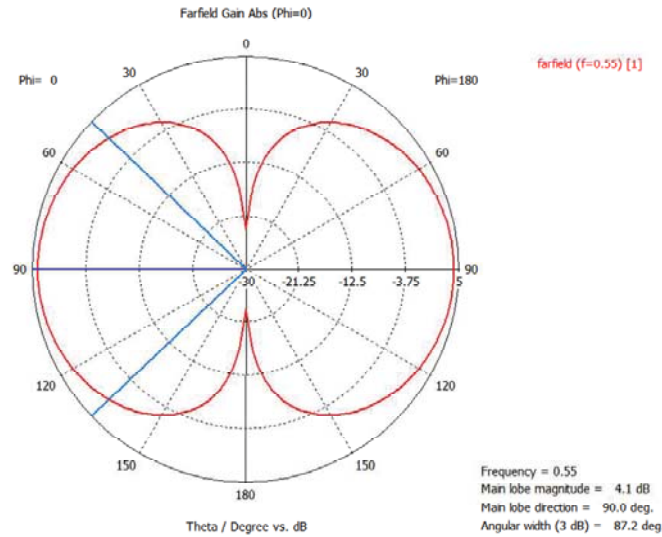
Figure 4.2: Simulated H-plane radiation pattern for the DTV wire antenna.

Figures 4.4 and 4.5 show the typical simulated gain profile for the DTV wire and tape antenna. In these figures the front-to-back ratio of unity is clearly shown, ensuring that the same amount of power will be received from both sides of the antenna.

Table 4.1 shows the simulated gain and the 10 dB return loss fractional bandwidth (BW) for the optimized copper wire and tape antennas across the selected bands. The gain for all of them is almost constant across all the bands and a clear increase in the fractional bandwidth can be appreciated for the highest frequencies. As with
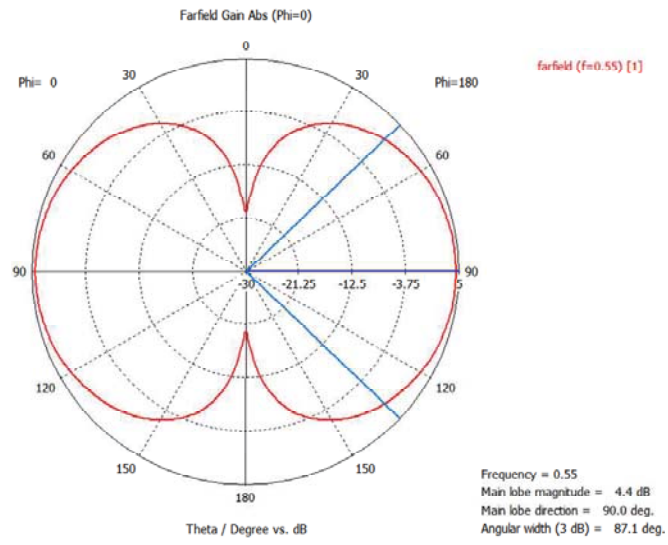
Figure 4.3: Simulated H-plane radiation pattern for the DTV flat antenna.
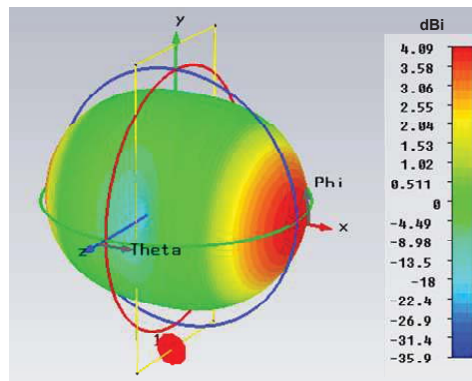
Figure 4.4: Simulated beam profile for the DTV wire antenna.
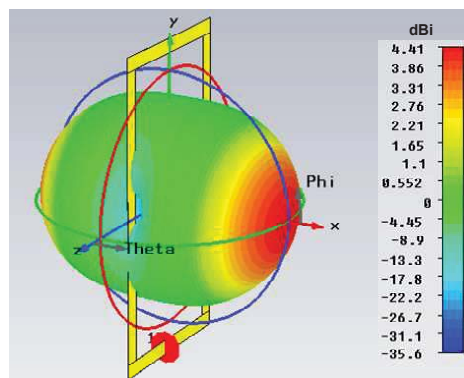
Figure 4.5: Simulated beam profile for the DTV tape antenna.

any antenna type, this is due to the increase in antenna volume from the wire to the flat antenna.

Table 4.1: Simulated Gain and 10 dB Return Loss Fractional Bandwidth for Modified Folded-dipole Single-band Antennas

Band		Wire		Tape	
	BW [%]	Gain [dBi]	BW [%]	Gain [dBi]	BW [%]
DTV*	26	4.35	4	4.48	6
GSM900	3.7	4.42	4.3	4.73	4.3
GSM1800	4.1	4.32	5.3	4.73	10.7
3G	2.8	4.39	5.4	4.76	12

During switch over

Figures 4.6 and 4.7 show the predicted and measured return loss results, within a 10 dB return loss bandwidth, for the eight fabricated single-band antennas. It was found that better return loss measurements are achieved with our single-band antennas when compared to other reported single-band omnidirectional [84] and multi-band [99] designs. The latter may be important, as it may be tempting to implement a more compact multi-band rectenna, which may ultimately decrease the performance of the ambient RF energy harvesting due to low return loss.
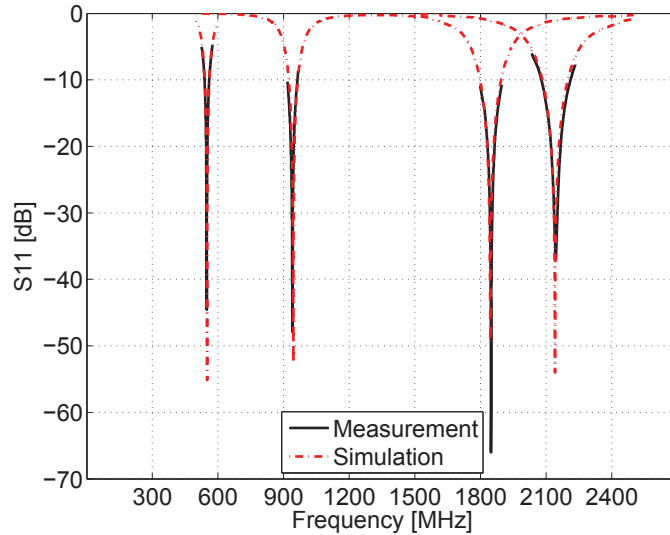
Figure 4.6: Input return loss predictions and measurements for all wire single-band loop antennas [20].

Obtaining a minimum acceptable return loss over an antenna fractional bandwidth
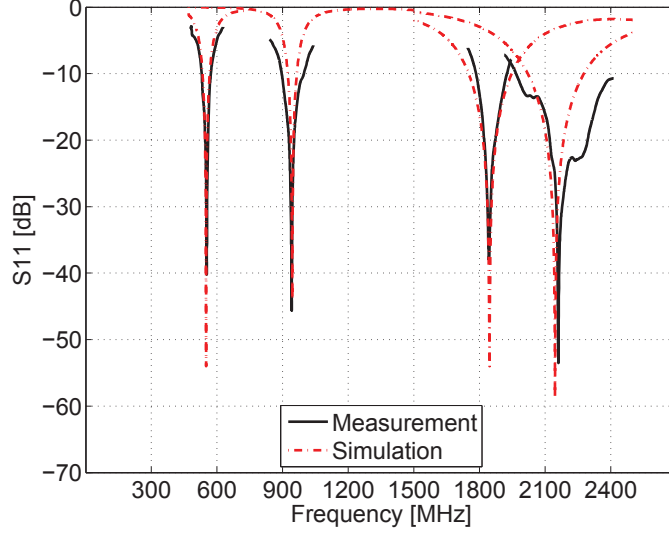
Figure 4.7: Input return loss predictions and measurements for all tape single-band loop antennas [20].

as large as that of the source is key to harvest as much input RF energy as possible. As can be seen in Table 4.1, where the fractional bandwidth is defined for a 10 dB return loss, these antennas have a fractional bandwidth greater than those of the sources; with the exception of DTV, which only covers approximately 35% of the target frequency range. In other work [57], 5 dB return loss fractional bandwidth is adopted for RF energy harvesting applications.

The fractional bandwidth of the antennas having a minimum return loss of 5 dB is too great to assume a constant antenna gain over the whole band. Therefore, an additional advantage of using 10 dB return loss fractional bandwidths is that (4.1) can be used to calculate the input RF power with the assumption that the mid-band antenna gain is constant with frequency [110]. Therefore, the time-averaged input RF power P_{RF} is given by:

$$P_{RF} = S_{BA}A_{real} \text{ and } A_{real} \approx G(fo)\frac{\lambda_o^2}{4\pi} \tag{4.1}$$

where A_{real} is the effective aperture (or capture area) of the antenna, λ_o is the free-space wavelength at the mid-band frequency fo and $G(fo)$ is the rectenna's antenna gain at fo. Substituting the measured input RF power densities recorded in Table 3.3 and the predicted mid-band antenna gains in Table 4.1 into (4.1), realistic values for

P_{RF} can be calculated for all four bands, with the results shown in Fig. 4.8. It is seen that as all antenna gains are in the region of 4.5 dBi, the GSM900/1800 harvesters can generate the highest input RF power levels, due to the high banded input RF power density levels measured *in situ*. At the other extreme, the 3G harvesters will be the worst performers. As only a small fraction of the required frequency range is covered by the DTV antennas, the predicted values for P_{RF} represent an overestimation.
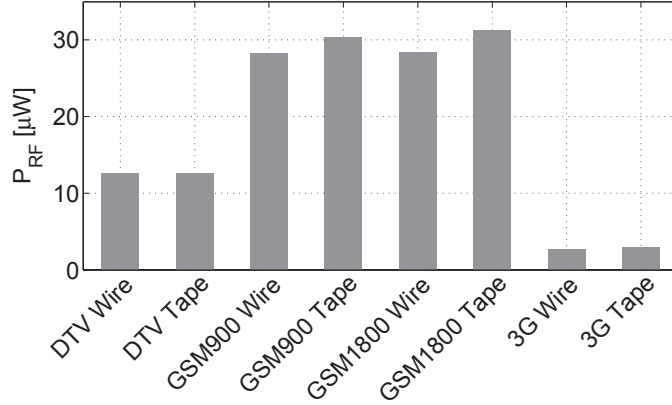
Figure 4.8: Predicted input RF power levels for the four largest ambient sources at the ICL testing location [20].

To emphasize the need of the survey measurements to predict the input RF power that the harvester could receive, the Friis' transmission equation was used, based on the distance between Imperial College London and the Crystal Palace Transmitter. It is important to note that in this case the impedance matching is assumed perfect as well as a perfect line of sight to the transmitter with no reflections or multipath. In a similar fashion to [5], the received power P_{RX} was calculated with (4.2) at 548 MHz, with a TX to RX distance $R_{RX} = 11.1$ km, ERP (effective radiated power) of 20 kW and receiver antenna gain of $G_{RX} = 4.5$ dBi.

$$P_{RX} = P_{TX} + G_{TX} + G_{RX} + 20log_{10}\left(\frac{\lambda_o}{4\pi R_{RX}}\right) \qquad (4.2)$$

where the transmitter antenna gain and power G_{TX} and P_{TX}, respectively, are equal to the EIRP=ERP+2.15 dB, which is 44 dBW for the Crystal Palace Transmitter. Substituting the EIRP in (4.2) gives $P_{RX} = -29.71dBm = 1\mu W$, which is three

orders of magnitude higher than the maximum input power measured during the survey for the same conditions. This shows how using Friis' transmission equation in an urban to semi-urban environment, even with a clear line of sight between the TX and RX, provides an overestimate of the available power, thus resulting in an inaccurate harvester design that will be inefficient at the low ambient RF power levels.

4.3 Rectifier Design and Measurements

With the antenna selected, designed and characterised, the total expected banded input RF power can be used to select the optimal rectifying component and topology. In this section, a comparison of rectifying COTS components is presented, as well as their performance in a series rectenna configuration. In addition, the advantages of this configuration over a shunt and voltage doubler topologies for the selected frequency bands and available input power levels are presented.

4.3.1 Diode and Rectifier Topology Selection

As presented in Chapter 2, much effort has been made by the international community to select the optimal rectifier technology for harvesting RF power, either from dedicated or readily available sources. It has been highlighted throughout this chapter that defining the latter is crucial in selecting the rectifier and rectenna topology, since ultimately this will set the available power levels at which the harvester will work. Therefore, a specific rectifier and rectenna topology, which is optimized for working at high input power levels from a dedicated source, will not be as efficient in low ambient power levels; the opposite condition applies as well [112].

To start the rectifier design, Schottky diodes were selected, based commercially available devices. Schottky diodes were selected for rectification purposes because of their shorter transit time (required for the selected frequencies) when compared to p-n diodes and transistors and for their low turn-on voltage. This low turn-on voltage is required because the diode will not operate with bias and consequently will not operate in its most efficient region. Therefore, Schottky diodes that are able

to operate with zero bias are needed for low power, high frequency rectification.

From the open literature, the Avago HSMS-2850 and Skyworks SMS7630 were selected for their zero bias characteristics and their already proven performance from 0.8 to 5 GHz [113]. The MZBD-9161 GaAs beam lead detector was selected because of its comparable performance to the previously described diodes and its potential for working at higher frequencies from 1 to 110 GHz. A few characteristics of these diodes are presented in Table 4.2, where C_j is the junction capacitance, R_s is the series resistance, R_v is the video or junction resistance, L_p is the parasitic packaging inductance, C_p is the parasitic packaging capacitance and V_j is the junction voltage. The small-signal model of the diode is presented in Figure 4.9. These diodes were selected because of their low junction voltage, junction capacitance and series resistance when compared to other COTS detectors.

Table 4.2: Small-signal Parameters for Selected Zero-bias Schottky Diodes

Device	C_j [pF]	R_s [Ω]	R_v [kΩ]	L_p [nH]	C_p [pF]	V_j [V]
SMS7630	0.14	20	5000	0.7	0.11	0.34
HSMS-2850	0.18	25	8000	2	0.08	0.35
MZBD-9161	0.035	20	3000	0.3	0.11	0.26
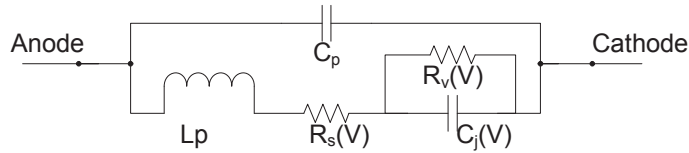
Figure 4.9: Small-signal diode model.

Based on previous analyses presented in [114, 115] and summarized in Chapter 2, low power energy harvesting rectifier configurations were simulated, in order to compare previously published configurations and to select a semiconductor device that would achieve a higher conversion efficiency. The analysis from these results gives a clear explanation as to why series rectification is more efficient than a shunt configuration for frequency scalable rectennas.

Rectification is inherently a large signal operation and, therefore, assuming a constant value of R_s (*i.e.* a linear model) is invalid. In addition, junction capacitance

is very important at high frequencies. For these reasons, the large signal harmonic balance (HB) simulation tool from Agilent ADS was chosen to simulate rectenna designs at different frequencies and input powers levels.

HB is a large signal frequency domain technique, which evaluates the non-linear elements in the time domain using an inverse Fourier transformation and with the linear elements analysed in the frequency domain. After the non-linear devices are analysed in the time domain, they are converted to the frequency domain at each iteration, to obtain their spectral behaviour. The currents of the linear and non-linear elements have to be balanced for every harmonic to finalize the analysis [101]. Since HB assumes that all inputs are a series of steady-state sinusoids, the solution will also be in steady-state, helping to do fast and accurate RF simulations without having to wait until the transient solution finishes [102].

In HB simulations, the antenna was simulated using its equivalent Thevenin circuit, with a single tone power source and source resistance, as shown in Figures 4.10 and 4.11 for the series and shunt rectifier configurations, respectively [21]. The source resistance represents the antenna's impedance of 50 Ω, which has to match the impedance of the rectifying circuit to ensure maximum power transfer.
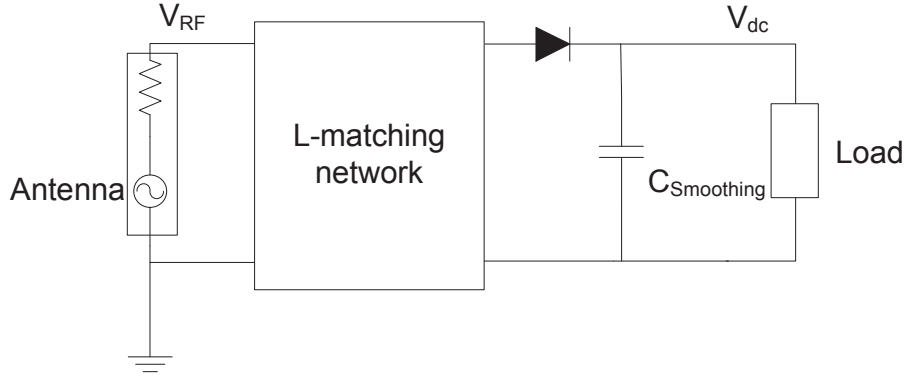
Figure 4.10: Series detector configuration with and L-matching network

As seen throughout the literature review, many research teams have defined several figures of merit for comparing rectennas. This work uses conversion efficiency η, as described below.
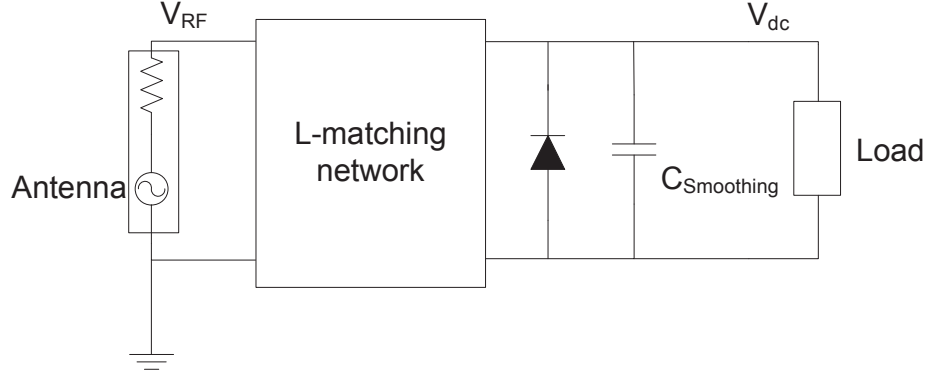
Figure 4.11: Shunt detector configuration with an L-matching network

$$\eta = \frac{P_{dc}}{P_{RF}} \qquad (4.3)$$

where P_{dc} is the time-averaged output (*i.e.* equivalent dc) power into the storage element (*e.g.* battery or supercapacitor) and load.

To ensure that all the different simulations were compared on the same basis, an optimized lumped element L-matching network and an optimal load were used for each power and frequency band. The L-matching network was designed with the aid of the ADS Smith chart utility, which automatically matches to different impedances at a specific frequency, ensuring that a perfect match is always achieved. Finally, output dc power and efficiency were calculated. Fig. 4.12 shows the simulations results for a series rectifier configuration, with a measured DTV input power level of -19.2 dBm = 12 μW. The HSMS-2850 presented the highest conversion efficiency for 0.1 GHz to 1 GHz, the SMS7630 for 1 to 10 GHz, and the MZBD-9161 presented the highest efficiency between 10 to 100 GHz, highlighting its capabilities for high frequency applications.

Due to the selected frequency bands being below 3 GHz, the analysis will focus on the differences between the HSMS-2850 and the SMS7630. Figures 4.13 and 4.14 show the performance of the latter diodes in an impedance matched series configuration across different frequencies and input power levels. As Fig. 4.12 suggests, the HSMS-2850 can achieve higher efficiencies than the SMS7630 for frequencies below 400 MHz. The 3D plots illustrate how the HSMS-2850 can ideally achieve efficiencies
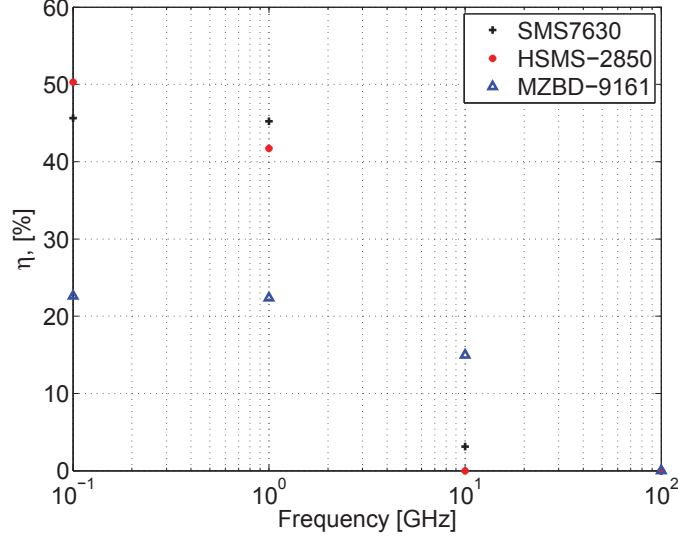
Figure 4.12: Conversion efficiency of an impedance matched series configuration rectenna [21].

close to 50% between 100 and 300 MHz, but it quickly drops for power levels below -20 dBm at higher frequencies. In contrast, the SMS7630 can achieve efficiencies higher than 22% for power levels as low as -30 dBm accross all frequencies of interest. The highest conversion efficiency at 2.45 GHz was 34% for an input power of -20 dBm with the impedance matched SMS7630 in a series configuration and a 3250 Ω load. These results are similar to the ones found in [115] using the SMS7630, thus proving the SMS7630 to be one of the best COTS zero bias detectors for frequencies near 2.45 GHz and low power levels.

These results also demonstrate that the lower R_j, R_s and C_j are the better the performance of a zero bias Schottky diode at higher frequencies. As the barrier height of a Schottky diode decreases, the saturation current I_s goes up and R_j decreases. Also, low silicon doping lowers the R_s but increases C_j, making this trade-off very important to make the cut-off frequency of the device higher [116]. In contrast, the ideality factor n_d increases as the barrier height decreases. Therefore, there is a compromise in how small the barrier height can be to have an efficient zero bias detector that works at high frequencies. Equation (4.4) shows the relationship between the R_v and I_s [116], where V_t is the thermal voltage.
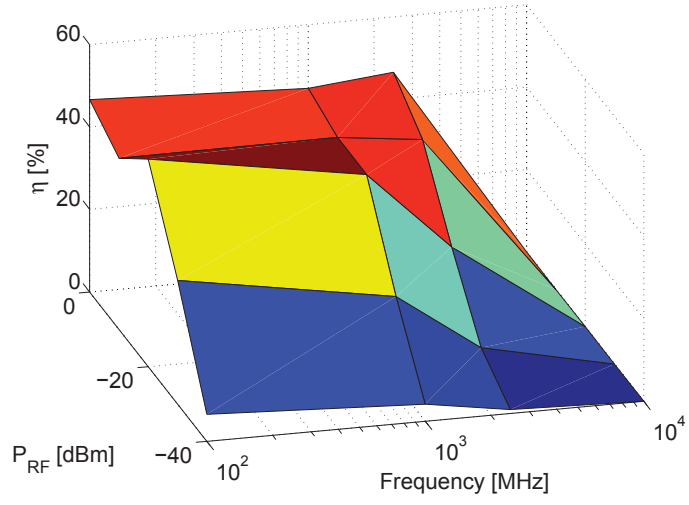
Figure 4.13: Conversion efficiency of an impedance matched series configuration using a HSMS-2850 diode through different power RF levels and frequencies.
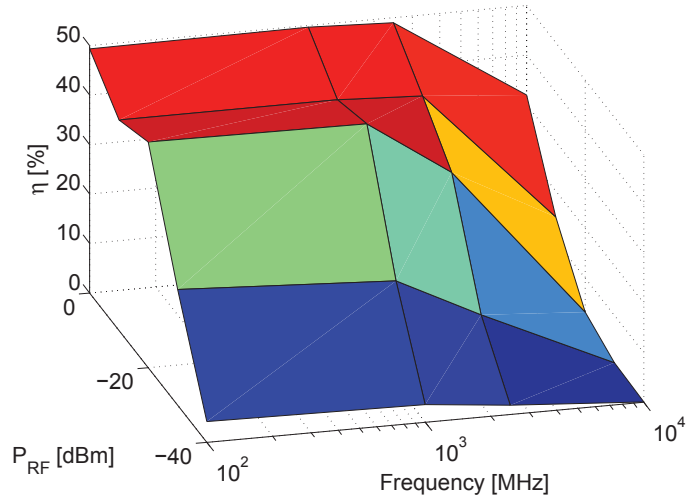
Figure 4.14: Conversion efficiency of an impedance matched series configuration using a SMS7630 diode through different power RF levels and frequencies.

$$R_v = \frac{n_d V_t}{I_s} \tag{4.4}$$

Based on the simulation results, previously reported analysis in [21, 114] and the predicted input RF power levels presented in Fig. 4.8, the zero bias SMS7630 diode was selected as the optimal solution for ambient RF energy harvesters a series configuration. The selected diodes in a shunt configuration achieved efficiencies of less than 1% at input power levels lower than -15 dBm, thus confirming that a shunt configuration is not efficient for low power applications.

To understand why the shunt configuration is not suitable for ambient RF harvesting, Figures 4.15 and 4.16 show the series and shunt rectifying configurations with the diode's small-signal model [114].
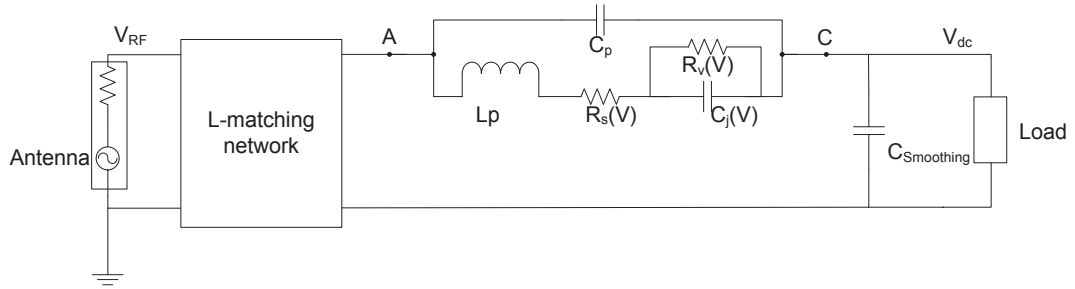
Figure 4.15: Series configuration rectenna with small-signal diode model.

In a series configuration, the junction capacitance $C_j(V)$ of the diode dominates the detector's impedance, as long as the output filter or smoothing capacitor $C_{Smoothing} > C_j(V)$, and thus $C_{Smoothing}$ has little or no effect on the matching circuit. This allows $C_{Smoothing}$ to be large enough to provide a ripple free output voltage. In contrast, $C_{Smoothing}$ must be less than 1 pF to achieve a good impedance match with a shunt configuration, as $C_{Smoothing}$ appears in parallel with $C_j(V)$ and the packaging parasitic capacitance. However, $C_{Smoothing}$ is too small to provide a ripple free dc voltage to the load. This can be overcome with a matching network that will allow a good impedance match with a large output capacitor, but at the expense of a introducing losses. Furthermore, as shown in [117], this issues start to become negligible with a shunt configuration as the shunt diode becomes more self-biased as the input power increases.
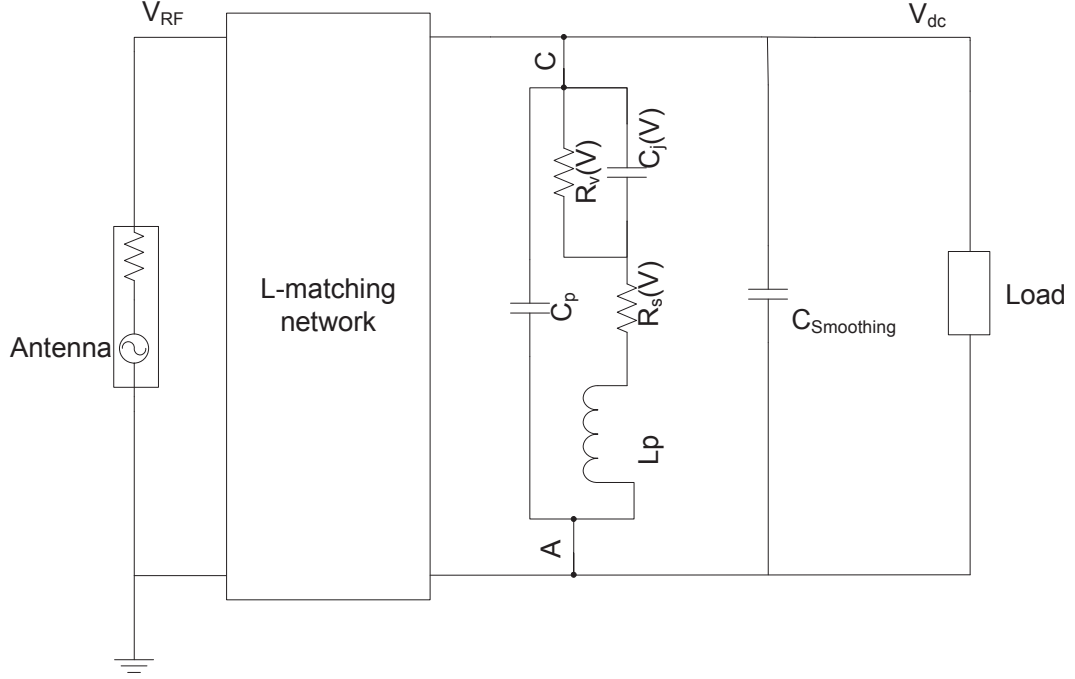
Figure 4.16: Shunt configuration rectenna with small-signal diode model.

Other rectenna topologies, such as a voltage doubler or a double-series, were not considered, since it has been proven that these configurations cannot achieve high efficiencies at power levels below -15 dBm [5,48,117–119]. In contrast, they are ideal for high power levels, such as the case of a dedicated radiating WPT, where these topologies achieve high efficiencies and high output voltages. These topologies can achieve high efficiencies even with an increased voltage drop, intrinsic to multi-diode topologies.

4.3.2 Single-band Rectennas

Simulations were performed using Agilent's ADS co-simulation capability. Its Momentum package not only takes into account the losses from the low-cost FR4 substrate, used in this work, but also calculates fringing fields effects, which are passed to the harmonic balance package for simulating the non-linear behaviour of the rectifier.

In the first rectenna prototype, a good impedance match to 50 Ω was achieved by employing a simple matching network, as shown in Figures 4.17 and 4.18. In this

circuit, a series lumped-element inductor was used to absorb part of the capacitive
reactance from the series diode and an additional quarter-wavelength short-circuit
shunt stub was employed to achieve the desired 50 Ω impedance [120]. Since the
impedance of the diode varies with frequency and input RF power, impedance match-
ing between the antenna and rectifier was first undertaken by finding the optimal
output load resistance for the measured input RF power levels with a single-tone
source at the mid-band frequency. After the optimal load was found, further broad-
band optimization was performed to the impedance matching network and the load
to ensure good impedance matching throughout the target frequency range and the
measured P_{RF} for each band. The modulated sources available in ADS were not
suitable to simulate readily available sources due to the random behaviour of the
data rate generated by different transmitters.
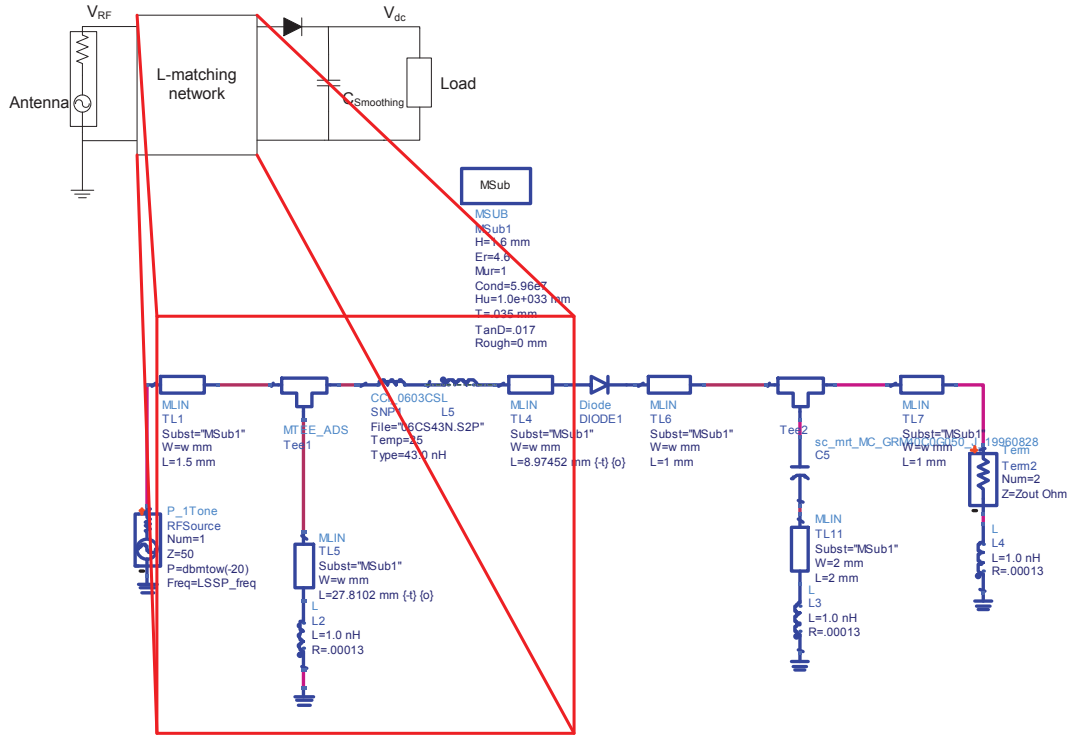
Figure 4.17: Impedance matching network of the first series rectenna prototype in
ADS.

As with the antenna analysis, and unlike conventional RF circuits that adopt the
more traditional half-power bandwidth definition, the rectifier should adopt the 10
dB input return loss bandwidth. The reason for this is that, for ambient RF energy

Figure 4.18: Half-wave 3G version 1 rectifier prototype on FR4 substrate [20].

harvesting applications, input RF power is at a premium and so what little energy is available should not be wasted by being reflected back from avoidable impedance mismatches at either the antenna or rectifier.

Fig. 4.19 shows the predicted and measured input return loss results, within the -10 dB bandwidth, for the DTV and GSM900 rectifiers, having fractional bandwidths of 5.7% (below target) and 4.8%, respectively. With these lower frequency designs, the fundamental and higher order harmonics were naturally suppressed by at least 55 dBm, ensuring a clean dc voltage at the load, without the need for any output filtering. Reasonable agreement was found with the GSM1800 and 3G rectifiers, having fractional bandwidths of 1.6% (below target) and 7.4%, respectively. This is due to the bandwidth of an L-matching network which could be increased if the order is increased. It was found that with these two higher frequency designs the higher-order harmonics were only suppressed by 40 dBm at the output. This reduced performance is due to the higher series inductive reactance leads of the output shunt storage capacitor.

For this reason, a second prototype version (v2) was designed for the 3G rectifier, using distributed-element components for the input impedance matching stage and an additional output filter stage, displayed in Fig. 4.20. With this version, it was found that in order to achieve and simplify the impedance matching to 50 Ω, all the microstrip transmission lines had to have a characteristic impedance of 92 Ω. A shunt quarter-wavelength open-circuit stub, designed for operation at the fundamental frequency, was employed to achieve a good dc isolation. The fabricated v2 3G
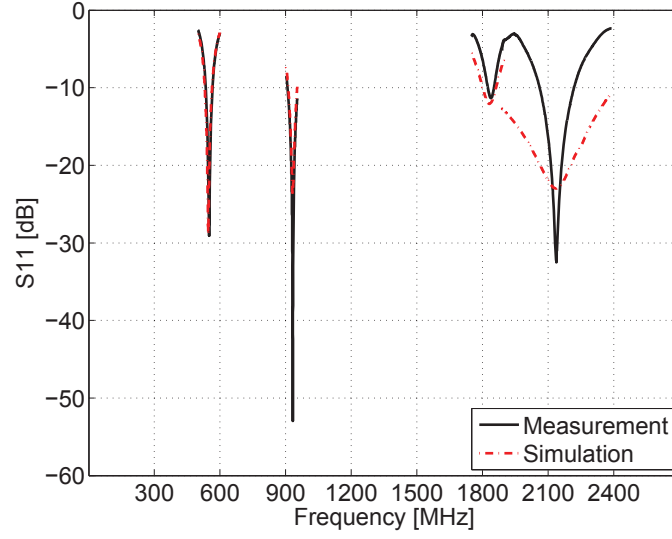
Figure 4.19: Input return loss predictions and measurements for all first prototype single-band rectifiers, with optimal load resistances at the output [20].

prototype, presented in Fig. 4.21, was able to suppress the higher order harmonics by at least 50 dBm, isolating efficiently the dc output.
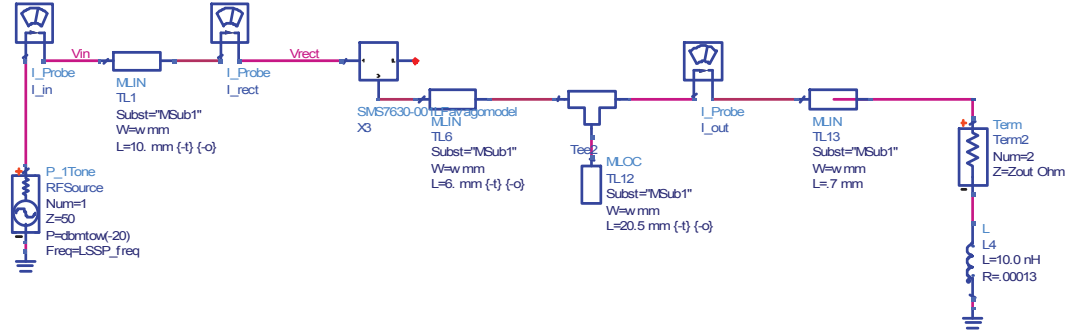
Figure 4.20: Impedance matching network of the second version of the series rectenna prototype.

As can be appreciated on the v2 fabricated prototype, a 1.2 mm extension was added to the stub, to account for a mismatch between simulations and measurements, which is due to the tolerance of the dielectric constant provided by the FR4 manufacturer, which varies between 4.3 and 4.8. There is also a discrepancy of the loss tangent provided by the manufacturer and the one present in the real boards. This can be avoided by the use of a substrate intended for RF applicatios, such as the Rogers RT5870. Figure 4.22 shows the simulation and measurement results of the 3G v2 prototype. After the stub tuning was performed, a significant agreement

95
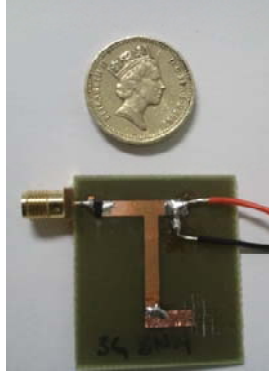
Figure 4.21: Half-wave 3G version 2 rectifier prototype on FR4 substrate [20].

between results was achieved and power was effectively delivered to the load thanks to the isolation provided by the stub.
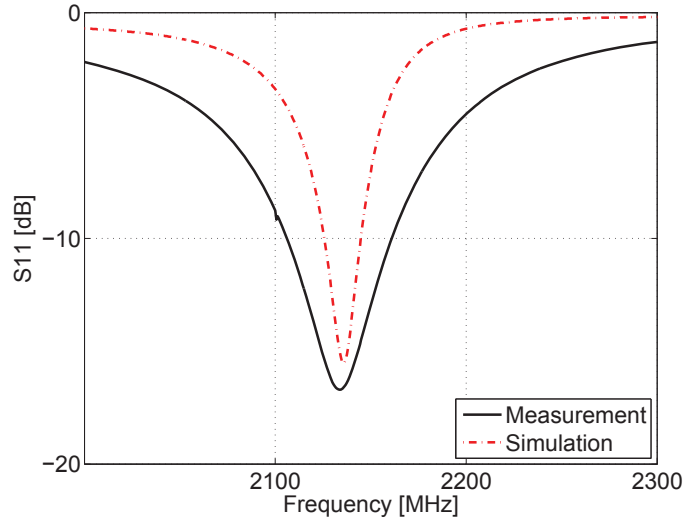
Figure 4.22: Input return loss predictions and measurements 3G v2 single-band rectifier with optimal load [20].

4.3.3 Power Management Module

Since the input RF power from ambient sources can be represented as a multi-tone source, with power levels fluctuating across the target frequency range, the output impedance of the rectifier is time varying. A power management module capable of performing maximum power point tracking is required. For this work, a low power integrated circuit PMM from Texas Instruments (BQ25504) was selected, due to its low quiescent current (< 330 nA) and low input voltage operation (80 mV hot-start

and 330 mV cold-start) [22]. It is worth noting that its start-up voltage is lower than PMMs previously reported and realized using hybrid circuits for RF energy harvesting [3]. The BQ25504 PMM includes a boost converter that steps-up its input voltage (having a 350 mV average value during ambient operation) to useful levels between 2.4 and 5.3 V. The BQ25504 also has a built-in battery management module, which is used to control the duty cycle of the output power to the load. The efficiency of the PMM for an input voltage and current of 400 mV and 10 μA, respectively, is above 65% [22]. This shows a considerable improvement over other non-comercial boost-converters for RF harvesting, capable of achieving 52% at the same voltage and power levels [121].

MPPT operation on the BQ25504 is achieved by periodically sampling the open circuit voltage (OCV) at the input of the converter, which then draws a current causing the converter input voltage to fall and be held at a preprogrammed fraction of the OCV (set by a potential divider connected to VIN_DC, illustrated in Fig. 4.23). In a simple dc circuit, with a resistive source impedance, the optimal ratio is 0.5. For the rectenna-based system, a ratio of 0.48 to 0.53 was found by using a potentiometer to maximise the power output of the system.
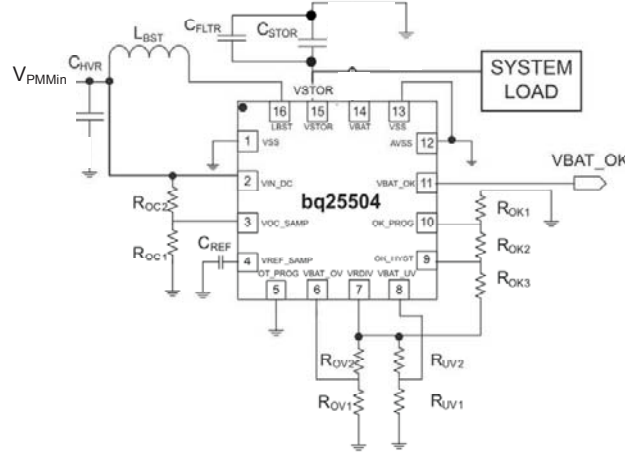
Figure 4.23: Simplified circuit diagram of the PMM with a BQ25540 [22].

The BQ25504 is designed to charge a storage element and in this case a 100 μF capacitor $C_{storage}$ was used. The PMM continuously charges the storage capacitor, and the load (a low power LED) was connected to the storage capacitor when the

capacitor voltage reaches an upper limit $V_{high} = 2.84$ V and disconnected when it reaches a lower limit $V_{low} = 2.40$ V, in the VBAT_OK pin. The duty cycle of the LED (Optolight series336 with and average power consumption of 5.4 mW [122]) can then be used to calculate the efficiency of the system, as will now be described. A diagram of the full harvester system is represented in Fig. 4.24.
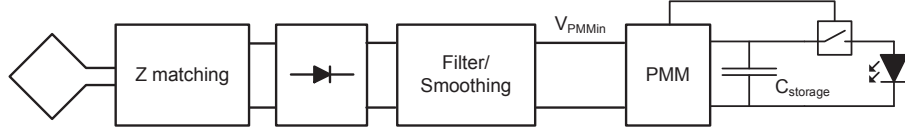
Figure 4.24: System block diagram.

4.4 End-to-end Efficiency Analysis

Measurements for this type of system are usually performed in a controlled environment (*e.g.* an anechoic chamber or TEM cell), using a dedicated constant or variable amplitude single-tone RF signal source [111], [123]. However, this is not suitable for evaluating ambient RF energy harvesting operation, which has a much broader spectrum of non-constant input frequencies and where the instantaneous input RF power is time variant. The use of a constant single-tone dedicated source provides a convenient stable reference power to the harvester; while available ambient sources have fluctuating power levels across a non-zero bandwidth and multipath and reflection effects are very difficult to simulate in a controlled environment.

Therefore, to determine the overall end-to-end efficiency η_{e-e} for a complete ambient RF energy harvester, the input RF energy U_{RF} is calculated based on the harvester's antenna characteristics and the actual banded input RF power density measurements taken at the time of harvester operation, using the Agilent FieldFox and the calibrated antenna. It is important to note that since the mismatch between the antenna and the detector is not taken into account, U_{RF} is higher than expected, providing an underestimate of end-to-end efficiency. The output dc energy U_{dc} was then calculated by measuring the charge-discharge cycle time, t_{cycle} of the storage capacitor between V_{high} and V_{low}, as the LED is repeatedly connected and discon-

nected. The output dc energy equation is already taking into account the efficiency of the PMM given the fact that the measurements are taken at its output. The end-to-end efficiency of one charge-discharge cycle of $C_{storage}$ is:

$$\eta_{e-e} = \frac{U_{dc}}{U_{RF}} \tag{4.5}$$

where the input RF energy is given by integrating the time-averaged input RF power over a cycle time, as:

$$U_{RF} = \int_0^{t_{cycle}} P_{RF}\,dt \tag{4.6}$$

and the output dc energy is given by the energy supplied to the load, as follows:

$$U_{dc} = \frac{C_{storage}\left(V_{high}^2 - V_{low}^2\right)}{2} \tag{4.7}$$

4.4.1 ICL Field Trials

Four single-band ambient RF energy harvesters were assembled by connecting the rectifiers to the wire/tape antennas and PMMs programmed for the optimal load. A 100 μF shunt capacitor was employed as the storage element, providing $U_{dc} = 115\ \mu$J. The system is capable of cold-starting the boost converter and MPPT block, since the rectenna is capable of providing the minimum starting voltage of 330 mV. When the minimum voltage is reached, the boost converter and MPPT start to operate and the charge-discharge cycle at the load begins, causing the LED to flash. During field trials, t_{cycle} took up to 170 seconds for the harvester with lowest banded input RF power density, corresponding to 3G with the wire antenna. Table 4.3 summarises the results where t_c and t_d are the charge and discharge times, respectively. The end-to-end efficiency was calculated using (4.5), with data from Fig. 4.8 and measuring the charge and discharge cycle time during harvesting operation. As can be appreciated, the discharge time tends to be longer for those bands where the input power is higher. This is due to the harvester being able to continue to provide enough power to maintain the LED ON. The smallest power per cycle can be correlated to the harvested with the longest charge to discharge cycle. It is important to note that

since ambient power conditions continuously change during operation, a correlation between the charge and the discharge time can not always be seen. This can be caused due to an increase of power during the discharge cycle, which would be expressed in a longer discharge time, even though the charge time was short.

Fig. 4.25 shows the overall end-to-end efficiencies for all the harvester demonstrators deployed and tested at ICL. As predicted by simulations, the improved 3G v2 demonstrator with tape antenna out-performed its original design by 11%; achieving an end-to-end efficiency of 40% with an input RF power of only -25.4 dBm.

A much greater efficiency can be achieved for the DTV harvester if the fractional bandwidths for the first prototype circuits (*i.e.* 4.4/4.5% for the antennas and 5.8% for the rectifier) are increased to match the much greater target value of 26%. Likewise, the reduced efficiency of the GSM1800 harvesters can be attributed to the detrimental effects of the narrow-band input impedance matching of the rectifier (*i.e.* having a fractional bandwidth of only 1.6%, when compared to its target value of 4.1%). Finally, with all the harvesters, the end-to-end efficiencies can be enhanced through better antenna design and optimal polarization matching.
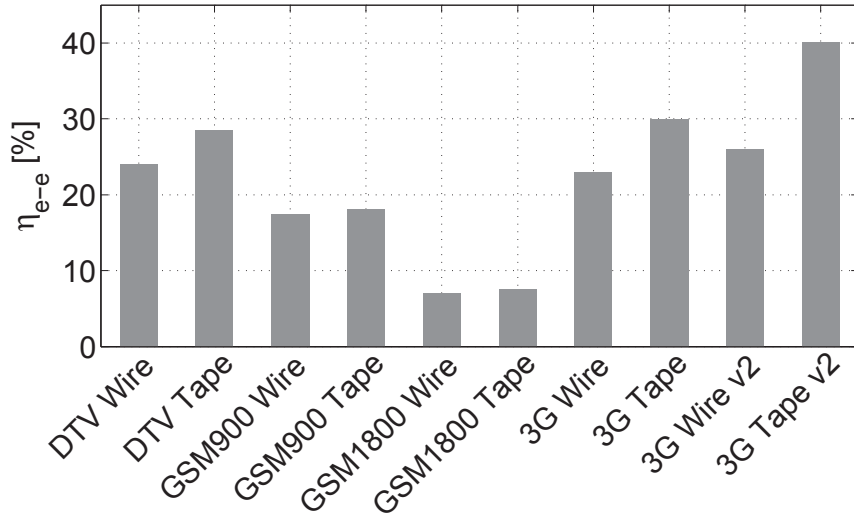
Figure 4.25: End-to-end efficiencies for single band ambient RF energy harvesting at ICL [20].

Table 4.4 summarises the number of locations from the London RF survey that would be able to support our harvesters.

Table 4.3: Harvester charge and discharge times (t_c and t_d, respectively) for a specified load.

Band	Wire					Tape				
	t_c[s] load independent	t_d[s] load dependent	t_{cycle}[s] load dependent	$P_{dc}(t_d)$ [μW]	$P_{dc}(t_{cycle})$ [μW]	t_c[s] load independent	t_d[s] load dependent	t_{cycle}[s] load dependent	$P_{dc}(t_d)$ [μW]	$P_{dc}(t_{cycle})$ [μW]
DTV	26	12	38	9.6	3	14	18	32	8.2	3.6
GSM900	14	10	24	11.5	4.8	8	13	21	14.4	5.5
GSM1800	43	15	58	7.7	2	22	27	49	5.2	2.4
3G v2	167	3	170	38.4	0.7	96	5	101	1.2	1.1

Table 4.4: Number of locations from the London RF Survey capable of supporting identical harvesters at the same efficiency levels

	DTV	GSM900 (BTx)	GSM1800 (BTx)	3G (BTx)
Stations with higher S_{BA}	2	28	68	122

Unlike the single-band 3G harvester, which can operate at 45% of the locations, our DTV harvester can only be used at two locations (one in zone 2 and the other in zone 3). Therefore, for the general deployment of an ambient RF energy harvester within an (semi-)urban environment, at street level, the single band DTV harvester may not be practical.

4.5 Array Architechtures

Since ambient input RF power levels can be low (*i.e.* below -25 dBm) and dependent on both time and spatial considerations, harvesters could be designed to extract energy with spatial-diversity within the same frequency band or using different frequency bands. For example, with the former, at a particular location there may be only one band that has significant levels of RF energy worth harvesting. In this case, spatial-diversity array architectures may provide more usable output power. Alternatively, with the latter, multi-band array architectures may provide more robust operation. With both forms of parallel array architecture (*i.e.* spatial-diversity and multi-band), a further classification can be seen through the use of either diversity/band switching or a summing node. With the former, physical switches automatically select whichever signal path delivers the highest input RF power level; with the latter, power from all signals is combined. Fig. 4.26 illustrates generic forms of parallel array architectures, showing that switching/summing can be performed electromagnetically at a single antenna or at the output from multiple antennas, rectifiers or power management modules.

Multiband array architectures, similar to those in Fig. 4.26(c) and Fig. 4.26(d), capable of RF harvesting from the four previously identified bands, were selected
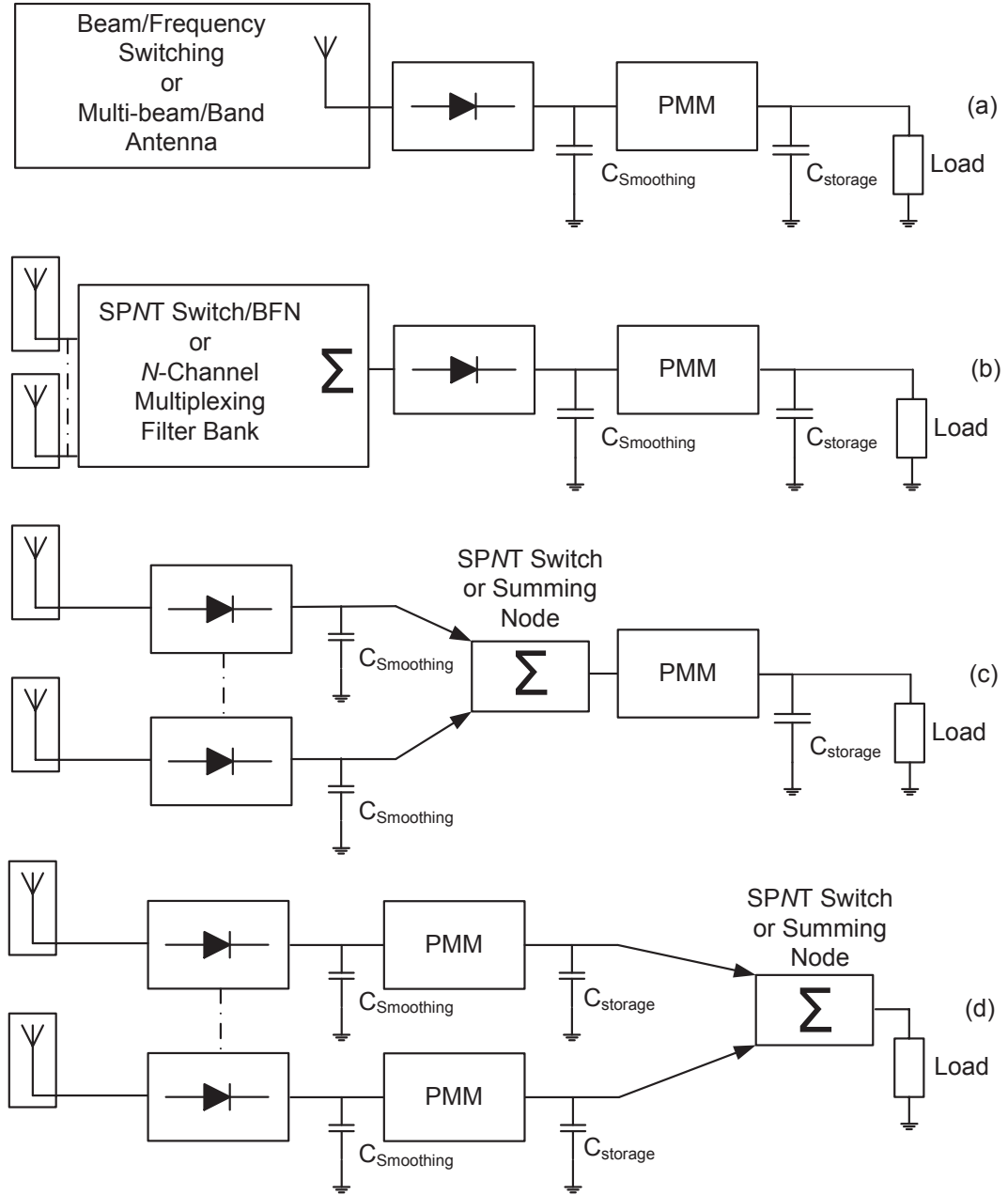
Figure 4.26: Parallel array architectures with switching/summing at the: (a) antenna; (b) output of multiple antennas; (c) output of multiple rectifiers; and (d) output of multiple PMMs [20].

given no size/cost constraints. The objectives were to reach the minimum cold-start voltage at the lowest possible input RF power levels and increase the harvesters' operational capabilities within (semi-)urban environments. To this end, two different multiple rectenna architectures were investigated. The first having a single shared PMM and the second having multiple PMMs, as illustrated in Fig. 4.27.
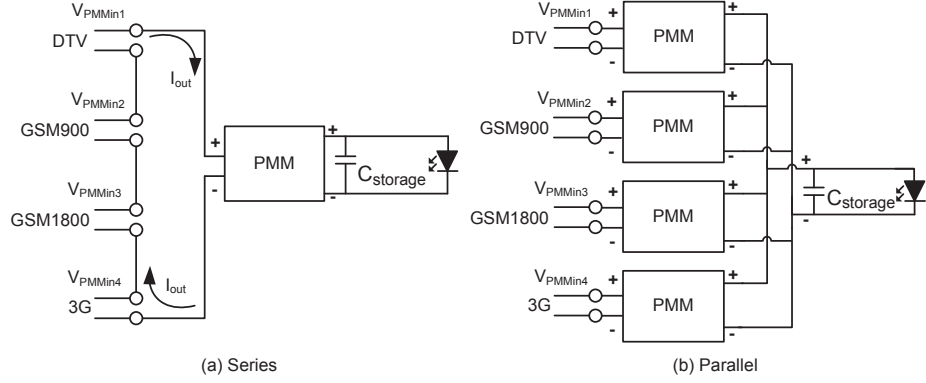
Figure 4.27: Multiband array architectures (with N = 4 bands): (a) voltage summing at the outputs of the single-band rectennas; and (b) current summing at the outputs of the single-band harvesters [20].

To simplify the assembly, the wire antennas were selected since they did not require a substrate. Unwanted coupling between the single-band antennas was minimised by placing them a minimum distance of $\lambda_L/5$ apart; where λ_L is the wavelength of the lowest frequency band antenna [124]. For example, the DTV and the 3G antennas were kept at least 11 cm apart, as shown in Fig. 4.28. This allowed S11 measurements to be the same as in Fig. 4.6, once all antennas were assembled into the array.

4.5.1 Multiple Rectennas with a Shared PMM

In order to improve the cold-start performance of the system, the outputs of multiple rectennas can be connected in series, as shown in Fig. 4.27(a). This increases the probability of the voltage on the input of the PMM reaching the cold-start level (330 mV for the BQ25504) under any given scenario. Whilst cold-starting the PMM, each rectenna harvests (albeit not optimally). Once the PMM circuit starts, with the MPPT operating, the harvested power level increases. The behaviour of the
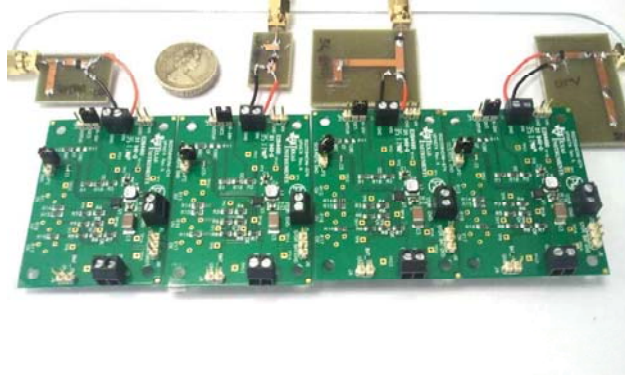
Figure 4.28: Rectenna array architecture with individual PMMs for the four largest contributors with wire antennas [20].

series rectenna topology with a shared PMM requires some discussion. As the output impedance and the OCV for each rectenna is different, since they operate at different frequencies and input RF power levels, the rectennas are forced to share the same output current in a series configuration, which does not allow them all to operate at their individual maximum power points. This causes the voltage on each rectenna output, except the one having the highest input RF power, to collapse. This operation is analogous to the partial shading problem with a series string of solar panels [125] sharing a common boost converter. With this photovoltaic system, bypass diodes placed around individual cells stop the poorly lit cells contributing a negative voltage (and power) to the string. In our case, the series circuit formed by the loop antennas and rectifying diodes performs the same task. This means that whilst all rectennas contribute to system start-up only the rectenna with the highest input RF power contributes significant power for continuous operation once the PMM starts.

Fig. 4.29 shows the end-to-end efficiency for the voltage summing multi-band harvester array when tested at ICL. An efficiency of only 15% was achieved, with a combined input RF power of -12 dBm. The lower efficiency, when compared to a single-band harvester, is due to the imbalance of rectifier outputs, as discussed above. Here, the charge time was 43 seconds, compared to 167 seconds with the lowest contributing single-band 3G harvester with wire antenna.

4.5.2 Multiple Rectennas with a Individual PMM

In order to overcome the balancing issues when multiple rectennas share a common PMM, as discussed previously, each rectenna can have its own PMM, whose outputs can be connected to a common storage element (in this case a 400 μF shunt capacitor, providing $U_{dc} = 461$ μJ), as illustrated in Fig. 4.27(b) and shown in Fig. 4.28.

Table 4.5 compares the multi-band harvester times with the single-band prototypes. ΣV and ΣI are the multi-band series or voltage summing and parallel or current summing array architectures, respectively. As one can appreciate, the parallel architectures achieve similar times to those from the single-band prototypes but for a storage element that is 4 times the size of the single band. Although not achieving cold-start as quickly as the series topology, the parallel topology has the advantage of being able to run each rectenna at its maximum power point. In addition, once a single rectenna is able to harvest enough energy for a cold-start operation, all PMMs will start because they share a common storage element. This allows the rectennas with low input RF power levels to harvest at lower power levels, which they could not do so independently.

This parallel topology was tested and found to be capable of operating in many locations where the series array was unable to operate; for example, if only one of the bands had $P_{in} <$ -25 dBm. As expected, the largest contributor hot-started (input dc voltage as low as 80 mW) the other PMMs, allowing them to harvest at an input RF power level down to -29 dBm. However, as with the previous results for voltage summing, having a combined input RF power of -12 dBm, the efficiency using multiple PMMs is slightly lower, at 13%, as shown in Fig. 4.29. This is because useful dc output power from the cold-starting harvester is being supplied to the other harvesters for hot-starting, even though some of them may not actually be contributing any of their own harvested power.

Table 4.5: Harvester charge and discharge times (t_c and t_d, respectively) for a specified load [20].

Band	Wire					Tape				
	t_c[s] load independent	t_d[s] load dependent	t_{cycle}[s] load dependent	$P_{dc}(t_d)$ [μW]	$P_{dc}(t_{cycle})$ [μW]	t_c[s] load independent	t_d[s] load dependent	t_{cycle}[s] load dependent	$P_{dc}(t_d)$ [μW]	$P_{dc}(t_{cycle})$ [μW]
DTV	26	12	38	9.6	3	14	18	32	8.2	3.6
GSM900	14	10	24	11.5	4.8	8	13	21	14.4	5.5
GSM1800	43	15	58	7.7	2	22	27	49	5.2	2.4
3G v2	167	3	170	38.4	0.7	96	5	101	1.2	1.1
Multiband ΣV	43	7	50	66	2.3	-	-	-	-	-
Multiband ΣI	55	5	60	92.2	2	-	-	-	-	-

Figure 4.29: End-to-end efficiencies for all ambient RF energy harvesting prototypes at ICL.

4.6 Output DC Power Density Comparison

The volumetric output dc power density S_{harv} [μW/cm^3] represents an important figure of merit for comparing alternative energy harvesting technologies. For ambient RF energy harvesting, the output dc power is calculated by multiplying the effective input RF power by the overall end-to-end-efficiency. The total volume (including that of the antenna, rectifier and PMM; not including energy storage, as this does not directly affect the dc power output) must be determined. It is important to note that the volume for the antenna could effectively disappear if it is assembled onto a window or within a wall, furnishing, fixture or fitting. Moreover, the required PMM PCB size used throughout these calculations was assumed to be ten times the size of the BQ25504 chip, to account for any necessary additional components. Fig. 4.30 shows the output dc power density for all the harvesters demonstrated here. It can be seen that the 2G GSM900/1800 harvesters with tape antennas both have the highest value of $S_{harv} = 7.4$ μW/cm3, when tested at ICL, due to the high banded input RF power density. The value for the most efficient harvester (*i.e.* 3G v2 with tape antenna) was not the highest in terms of output RF power, because S_{BA} in this band was more than an order of magnitude lower than with GSM900.

S_{harv} allows a direct and meaningful comparison to be made with other alternative
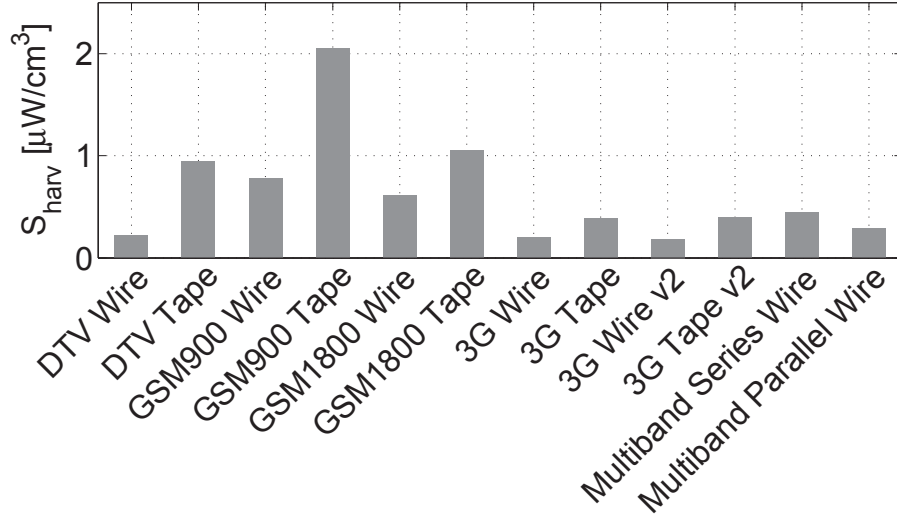
Figure 4.30: Output dc power density for all harvesters at ICL [20].

energy harvesting technologies. The best performing ambient RF energy harvester (*i.e.* GSM900 with tape antenna) was compared against alternative energy harvesting technologies, assuming they used the same PMM board size [23–25]. It can be seen from Fig. 4.31 that ambient RF energy harvesting has a low output dc power density when compared to alternative energy harvesting technologies, but only when the total volume of the first prototype demonstrator is considered. However, when the antenna is absorbed onto or into a background feature and when the PMM is fully integrated into the rectifier, it can out-perform (as indicated by the dotted column) the alternative energy harvesting technologies, while providing a complimentary means of extracting energy from the environment. The RF harvesters, however, have the additional advantage in that they do not require a thermal gradient and, unlike vibration-driven devices, they have no moving parts. The comparison is made against human sources of energy and not industrial sources, since the latter is several orders of magnitude higher. This would be the same case as power available from dedicated RF transmitters and ambient RF sources.
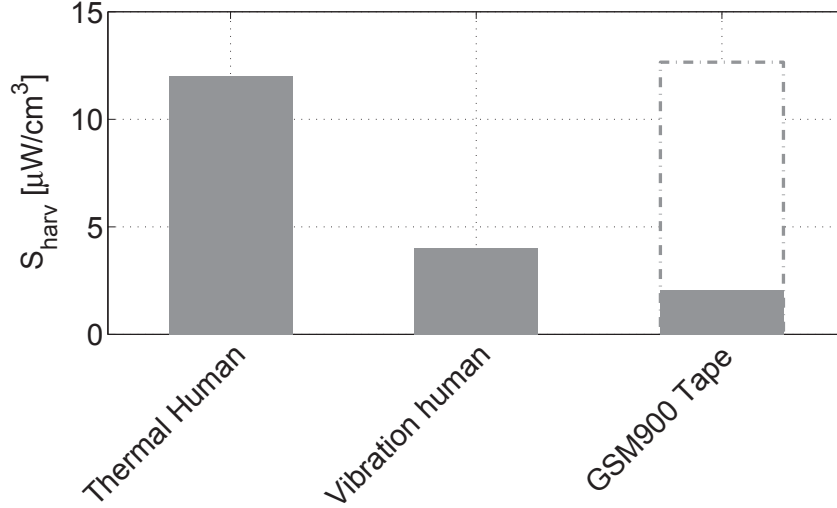
Figure 4.31: Output dc power density comparison for alternative ambient harvesting technologies [23–25] against the best current generation of RF harvesters at ICL [20]. Dotted line represents embedded antenna into background feature and integrated PMM and rectifier.

4.7 Conclusion

The objectives of this work were to analyse how much ambient RF power is available in a city and prove that suitable ambient RF harvesters could work efficiently in this scenario. In addition, this work should prove that useful power levels could be harvested from undedicated power sources. Once this was proven, the additional goals were to design and test harvesters capable of operating at the lowest possible ambient input RF power levels and extend the harvesters' operational capabilities within (semi-)urban environments.

To reach these goals, a comprehensive city-wide RF spectral survey was undertaken, and results presented in Chapter 3 helped to identify the four largest contributors (DTV, GSM900, GSM1800 and 3G). Measurements indicated that banded power density levels as high as 6.4 μW/cm^2 were available at street level. Furthermore, all the measurements were used to select the optimal antenna, rectifier and rectenna topology for the predicted ambient RF power levels.

A rectangular loop was selected as an ideal antenna for ambient RF harvesting since, as shown through simulations and measurements, it can provide a front-to-back ratio of one and a quasi-omnidirectional pattern; ideal for receiving signals from an

unknown source location. Wire and a copper tape frequency scalable antennas were fabricated for the four selected frequency bands and measurements shown that the fractional bandwidth of almost all the antennas exceeded the fractional bandwidth of the selected band, with the exception of the DTV prototype. The copper tape antennas proved to have twice the fractional bandwidth of their wire counterparts for GSM1800 and 3G, due to their higher overall volume.

With the antenna characteristics and *in situ* spectral measurements, the input RF power was calculated, showing that the highest power levels were around 30 μW for GSM900 and GSM1800 bands and as low as 2.5 μW for 3G. These power levels were used as the starting point for the rectenna topology selection and design. In addition, it was proven how a conventional power link budget calculation provides an overestimate of the available power, when compared to spectral measurements, due to the reflections and multipath phenomena intrinsic to an urban scenario.

Simulations and measurements showed that the SMS7630 zero bias Schottky diode was the most efficient COTS device for the selected bands and predicted input power levels. Furthermore, Harmonic Balance simulations and an analysis of the role of the diode's junction capacitance showed how a series half-wave rectenna topology is the most efficient rectenna topology for input power levels below -15 dBm, when compared to shunt, double series and voltage doubler configurations.

With the optimal component and rectenna topology selected, two single-band versions were designed and fabricated for each band. The first prototype that included a lumped element impedance matching network proved to achieve a match between simulations and measurements, covering almost all the selected bands and achieving a good dc-isolation at the output of the DTV and GSM900 prototypes. For the higher frequency prototypes, a new design with only distributed elements and no vias achieved the specified -10 dB return loss with an effective harmonic rejection at the output.

To ensure that the harvesters were operating optimally, regardless of input power variation, due to the variability of the ambient sources, the TI BQ2554 power management module was selected. This module is able to harvest power and boost the

detector's input voltage to 2.84 V, which was then used to power a 5.4 mW LED. It was demonstrated that single-band harvesters can operate with efficiencies of up to 40% in a (semi-)urban environment with duty cycles as high as 32% and can start to operate from power levels as low as -25 dBm.

To increase the freedom of operation, multi-band array architectures were investigated. With the current summing harvester arrays, RF harvesting was achieved at an input RF power level as low as -29 dBm, without any external dc power supply to hot-start the power management module. Limitations on the multi-band array architectures were discussed, highlighting the need for further work in balancing rectennas with voltage summing rectenna arrays when operating at lower input RF power levels. With the combination of the survey results and the harvester's performance, it is expected that more than 50% of the 270 London Underground stations are suitable locations for the deployment of the ambient RF energy harvesters presented in this work.

In this chapter, a full system design framework and optimization for ambient harvesters was presented and all project goals were achieved. Finally, an output dc power density comparison against alternative energy harvesting technologies has shown that RF harvesting can represent a competitive solution within (semi-)urban environments, especially when the antenna can be absorbed into background features.

Part III

Inductive Power Transfer

5 Introduction

5.1 History of Inductive Power Transfer

Inductive power transfer without a magnetic core was first proposed by Nikola Tesla around 100 years ago [126] to supply wireless mains power over long distances. Since then, low-power, closely-coupled wireless charging methods have been used to power medical implants [41], while the wireless powering of portable devices through charging mats is now available via commercial products [127]. Nonetheless, there has been a resurgence in research interest in wireless power transfer for medium range (*i.e.* 10s of cm) applications, such as electric vehicle charging through resonant inductive coupling [28, 128–130].

Highly cited reviews [27, 48] tend to present the history of wireless power transmission, in specific inductive power transfer, as a field that almost had a hundred years of darkness since Tesla's prototypes. According to these reviews, no developments were achieved in the latter field until 2007, when Marin Soljacic *et al.* published a journal paper where a resonant inductive power transfer system was capable of powering a 60 W light bulb at a distance of 2 m [131].

These historical accounts of the field of inductive power transfer are missing the major theoretical and practical developments that were achieved in the 1960's by John C. Schuder and his team at the University of Missouri Columbia (UMC). Schuder's contribution to the field of IPT was motivated by finding ways of powering artificial hearts transcutaneously, as shown in Figure 5.1. It was then that the field of Transcutaneous Energy Transfer (TET) started [26].

The intrinsic low coupling factor between the transmitter and the receiver coil in TET applications (k < 0.3) spurred the creation of the theory and first prototypes
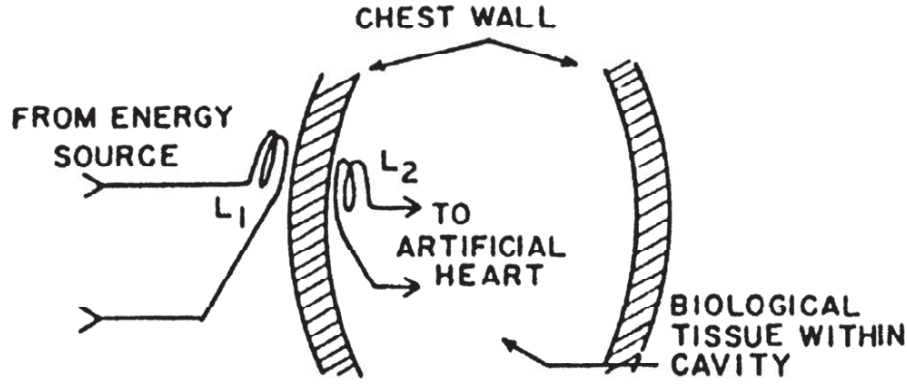
Figure 5.1: Inductive power transfer system with receiver inside a thoracic wall [26].

that were able to achieve high transfer or link efficiencies [132]. It is due to these developments that further research was able to achieve link efficiencies $> 95\%$ for low coupling factor systems. The coupling factor is a key variable in inductive power transfer since it defines the percentage of mangetic flux, generated by the transmistter, that reaches the receiver.

All recent attempts to achieve long distance IPT, such as the work from Soljacic's (from MIT) and Smith's *et al.* (from Intel Labs) [35], based their resonant inductive systems on the theory developed on TET more than forty years ago. Fig. 5.2 shows MIT's and Intel's demonstrators of IPT systems. As can be appreciated in this picture, Intel's system (top) uses single turn driver loops and planar coils, whilst MIT's system (bottom) uses helical coils [27] for the transmitter and the receiver. The details of these two systems will be explained in the following sections but it is important to note that, as with most IPT designs, these systems were designed to increase the link efficiency and not the total end-to-end efficiency. In medical applications, where tens to hundreds of mW are required, the system does not need to operate in efficiencies higher than 10%, as long as the load receives enough power to operate. In contrast, in medium to high power applications, such as the one mentioned in the motivation section of this work where 100 W are to be transmitted wirelessly, it is of the utmost importance that efficiencies above 60% or higher are achieved, in order to make IPT an attractive solution. This is based on commercial efficiency figures for wired laptop chargers

The next sections explain in detail the main building blocks of an IPT system,
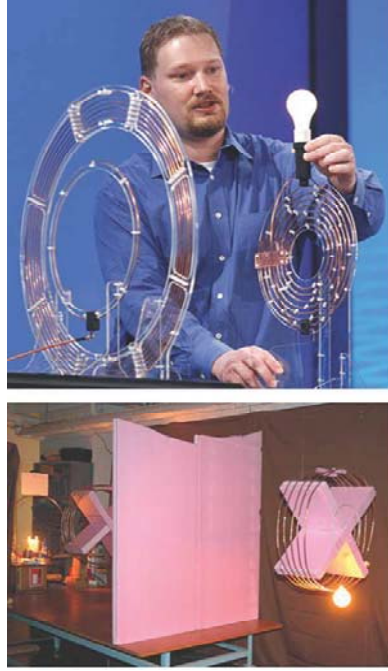
Figure 5.2: Intel's and MIT's IPT systems top and bottom, respectively [27].

in order to analyse all the parts and not only the link, that need to be optimized to achieve high end-to-end efficiencies. Furthermore, the state of the art and the different attempts to increase both link and end-to-end efficiencies are presented. These help to demonstrate the importance of the initial design focus, in developing an IPT system that could be capable of achieving similar or even higher efficiencies than many conventional wired power supplies.

5.2 System Analysis

A basic IPT systems architecture consists of several modules, as illustrated in Fig. 5.3. The architecture includes dc power supply units (PSUs), coil driver (*i.e.* clock genera-tor and power amplifier (PA) having an impedance matching network), transmitting (TX) coil with separation distance D from a receiving (RX) coil (measured from the centre-to-centre of the coils), an optional rectifier/regulator and a load. To fully characterize the complete system, the end-to-end efficiency η_{ee} of all the building blocks, from the ac source to the load, can be considered as follows; where the efficiency terms are shown on Fig. 5.3:
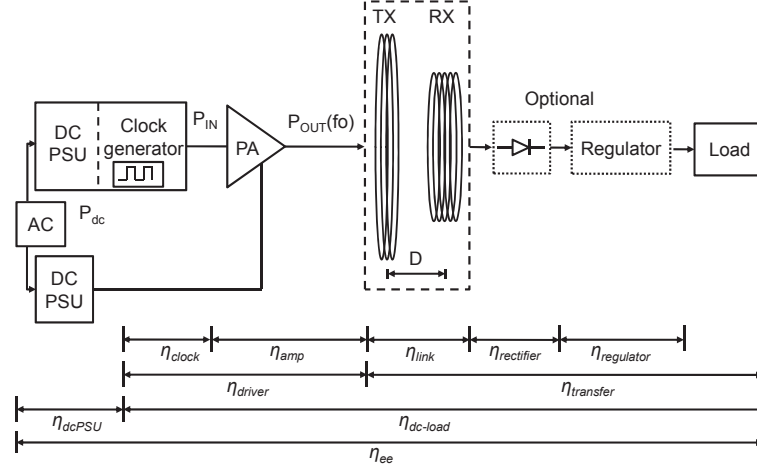
Figure 5.3: Inductive power transfer systems architecture.

$$\eta_{ee} = \eta_{dc\text{-}PSU}\eta_{dc\text{-}load} \tag{5.1}$$

$$\text{where } \eta_{dc\text{-}load} = \eta_{driver}\eta_{transfer} \tag{5.2}$$

$$\eta_{transfer} = \eta_{link}\eta_{rectifier}\eta_{regulator} \tag{5.3}$$

$$\text{and } \eta_{driver} = \eta_{clock}\eta_{amp} \tag{5.4}$$

where $\eta_{dc\text{-}PSU}$ is the combined efficiency of the dc power supplies, $\eta_{dc\text{-}load}$ is the dc-to-load efficiency, η_{driver} is the efficiency of the driver, η_{link} is the link efficiency, $\eta_{transfer}$ is the transfer efficiency, η_{clock} is the efficiency of the driver clock, η_{amp} is the efficiency of the power amplifier, $\eta_{rectifier}$ is the rectifier efficiency and $\eta_{regulator}$ is the efficiency of the regulator. This work focuses on optimizing $\eta_{dc\text{-}load}$ for an IPT system without a rectifier or regulator, *i.e.* maximising:

$$\eta_{dc\text{-}load} = \frac{P_{load}}{P_{dc}} \tag{5.5}$$

where P_{dc} is the total dc input power to the system (*i.e.* into the clock and power amplifier) and P_{load} is the real power dissipated in the load.

Well-defined figures of merit, such as $\eta_{dc\text{-}load}$ and η_{ee}, are used to evaluate IPT systems, to allow a straightforward comparison of the different emerging technologies in this field. From the IPT systems architecture in Fig. 5.3, the transfer efficiency just describes part of the system's efficiency and does not take into account the driver.

5.3 Literature Review

For many industrial and commercial applications, IPT systems must be capable of achieving a high η_{ee}, while transferring hundreds of watts at sub-metre distances, otherwise they will not be adopted. Several approaches for achieving good link efficiencies have been developed by various research groups. The first is to work at relatively low frequencies (tens of kHz), where efficient driver circuits can be easily realised and by increasing the coupling factor k of the system, using field-shaping techniques; for example, by employing metamaterials [30] and ferrite cores [28]. Field-shaping techniques normally occupy useful volume, require heavy materials, employ expensive fabrication techniques and need a precise coil alignment. These solutions make the field-shaping approach unsuitable for many applications, where the size, weight and cost of the system are limiting factors.

The second approach relies on transferring energy at the optimum frequency for maximum power transfer given a particular coil size, where the unloaded Q is maximised and compensates for the low coupling factor. In the past, this approach was not considered efficient, since low driver efficiency (due to semiconductor losses) dramatically reduced the end-to-end efficiency of the IPT system.

This section presents past and state-of-the-art designs, from academia and industry, and categorizes them according to the two approaches mentioned above. This analysis of the various attempts to increase the link efficiency, and in many cases the dc-to-load or end-to-end efficiency, helps define the starting point for designing an efficient IPT system capable of transferring tens of watts under low coupling conditions. Due to the aim of this work, close proximity, high coupling IPT systems, such as those being recently commercialized [133, 134] will not be analysed in detail.

5.3.1 Field Shaping

In [28], 2 kW of power was transferred at a distance of 20 cm using planar Litz wire coils at 20 kHz, with a link efficiency of 85%. The operating frequency was defined by the power handling capabilities of the coil H-bridge driver, limiting the coil's maximum unloaded Q-factor to 250. To compensate for the relatively low quality factors, ferrite bars were embedded in the coil pads, to shape the magnetic flux between the coils. Ferrite bars are lighter and more robust than ferrite discs and E cores [135–137]. Fig. 5.4 shows the coil pad assembly with the ferrite bars and an aluminium ring and back plane to help shield the surrounding area of stray magnetic fields. Both the tranmsitter and receiver had the same construction.
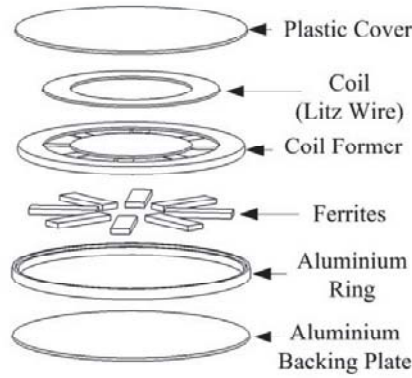
Figure 5.4: Exploded diagram of a Litz wire coil with ferrite bars and Al shielding [28].

The same research shows that increasing the number of ferrite bars improves the coupling coefficient, but careful consideration of the bar allocation inside the pad is crucial to avoid magnetic field nulls between the TX and RX coils. Furthermore, the saturation limit of the ferrite bars defines the width, and therefore, the weight of the bars; limiting the amount of power that the pads can handle. In addition, using ferrite bars has the disadvantage of increasing the vertical and horizontal offset sensitivity. If the separation distance between the coils is less than 10 cm, the system is unable to achieve more than 50% link efficiency and the transmitter power drops by more than half if the vertical offset exceeds 14 cm for a 60 cm diameter pad size. To increase the horizontal offset to a maximum of 16 cm, the pad needs to be as large as possible, but due to cost and weight limitations, a 60 cm diameter size pad

was selected.

The pads were designed to comply with magnetic field limitations. Magnetic field limitations by ICNIRP state that, between 20 to 150 kHz, the maximum flux level is 13.3 μT [104]. The Australian Radiation Protection and Nuclear Safety Agency (ARPANSA), has guidelines that define body average, temporal and body spot limits, which may be higher than 5 times the those specified by ICNIRP. According to ARPANSA, for systems working below 100 MHz, no part of the body should be exposed to more than 27 μT and an average of 6 μT [138]. The combination of field shaping and the aluminium shielding helped to minimize the stray magnetic fields away from the pads and meet the international and local exposure limits. At a distance of 17 cm from the edge of the pad, the maximum flux density was 7.2 μT, at a vertical offset of 35 cm, but at less than 50 cm from the pad, the field limits were exceeded [28].

In another system, designed to provide 2 kW of continuous power to a passenger bus, at a distance of 15 cm, ferrite components were used to increase the link efficiency up to 95%. The system required field shaping materials to compensate for coils with $Q < 50$, due to a 20 kHz insulated-gate bipolar transistor (IGBT) H-bridge coil drive [139]. The system was able achieve a link efficiency of up to 80%, for an offset of 26 cm, equivalent to 60% of the coil size.

A comparison of series and parallel resonant tanks is given, to analyse the most efficient tank topology combination [140]. The tank topology that achieved the highest efficiency and horizontal tolerance was using a parallel resonant transmitter tank with a series inductor and a series resonant receiver tank. The additional series inductor helps prevent current peaks during voltage transitions, due to the square wave from the H-bridge. This solution, albeit valuable to increase the link efficiency, is cumbersome due to core saturation limitations of the extra inductor and increasing transmitter losses, which decrease the end-to-end efficiency of the system.

Using the approaches described above, several companies have been established and have started commercializing IPT systems for static charging electric vehicles. These are Plugless Power, Qualcomm (formerly HaloIPT) and WiTricity [29, 141–

144]. The three companies have a very similar approach and system performance for transferring power wirelessly. All of them are capable of transmitting 2 to 3 kW of power across an air-gap of 10 to 18 cm. Their systems operate between 20 and 145 kHz and their end-to-end efficiency is above 85%. They use standard H-bridge inverters, as transmitter drivers, and full-bridge rectifiers on the receiver side. Although all companies use coupling factor enhancing techniques, mainly by the use of ferrite cores, the arrangement of the ferrite materials, selection of magnetic and dielectric materials, transmitter coil construction and automatic power transfer optimization is what differentiates them. For example, Witricity uses a combination of Titania, Barium tetratitanate, or Lithium tantalite for the coil fabrication, due to their low loss and high dielectric constant [145]. In addition Witricity also claims the use of metamaterials and photonic crystal structures for shaping magnetic fields [146].

HaloIPT and Witricity systems also require the use of dynamic impedance matching circuits, to couple to their $50\,\Omega$ coils and allow for impedance variations when the coupling changes, as shown in [147,148]. The use of field shaping techniques requires complex systems to account for misalignment or, as in the case of some commercial systems, the user is required to use an parking guidance system to precisely align the receiving coil on the car with the transmitter [29], see Figure 5.5.

Figure 5.5: Plugless Power wireless power transfer system for EV with parking guidance indicator [29].

Instead of using ferromagnetic materials, a team of researchers from the Mitsubishi Electric Research Laboratories used a metamaterial placed between the transmitter

and receiving coils to shape the magnetic fields and increase the coupling factor [30]. The use of metamaterials can help refocus the propagating wave and amplify evanecent waves, as explained in [149]. The IPT system has two 50 Ω driving and receiving loops that couple to two 40 cm diameter resonators, as illustrated in Fig. 5.6. The metamaterial was constructed from double layer square spirals single cells and has a first self resonant frequency of 24 MHz, which as Professor John Pendry from Imperial College London explained, will have a negative permeability [150]. The link efficiency of the system is 17% without the metamaterial. When the metamaterial was placed between the transmitter and the receiving coil, the system was able to transmit 40 W across an air gap of 50 cm with a link efficiency of 45% at 27 MHz.
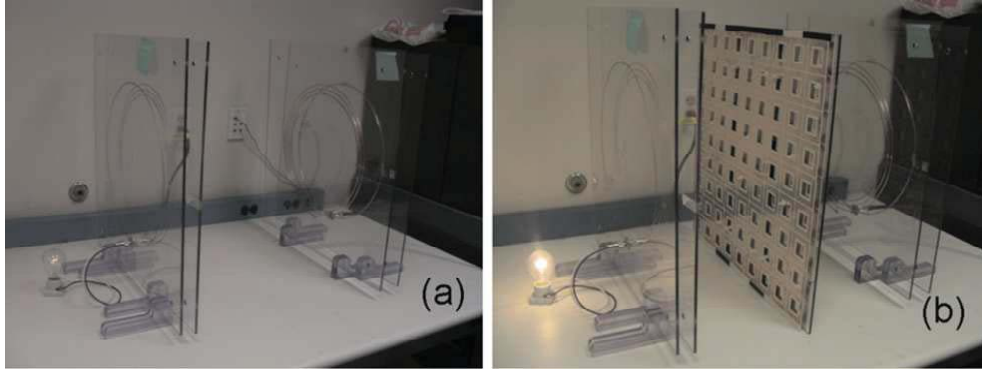
Figure 5.6: IPT system (a) without metamaterial (b) with negative μ and positive η metamaterial and a TX to RX distance of 50 cm [30].

A different approach to the conventional transmitter and receiver coil arrangement was proposed by the Korea Advanced Institute of Science and Technology (KAIST), to dynamically charge a passenger bus. In their on-line electric vehicle design (OLEV), two power lines embedded below the pavement carry up to 200 A of current, flowing in opposite directions at a frequency of 20 kHz. This current generates a magnetic field which adds constructively at the centre between the two power lines and is picked up by a receiving coil with ferrite material to power a passenger bus [31]. Due to the high power required by the passenger bus, the magnetic flux outside the bus exceeds ICNIRP limits by several orders of magnitude. To solve this problem, two different techniques are used. The passive technique involves placing

metallic brushes around the bus, which are in contact with metallic plates embedded in the road. The active technique involves placing two extra power lines parallel to the driving power lines, which generate the same magnetic field but in opposite phase. With this latter approach, the magnetic field from the driving power lines at the limit of the chassis are parallel to the ground, and as Fig. 5.7 shows, cancelling power lines decrease effectively the magnetic fields. Both active and passive solutions helped the OLEV system to comply with ICNIRP levels, achieving less than 6.5 μT at the edge of the bus.
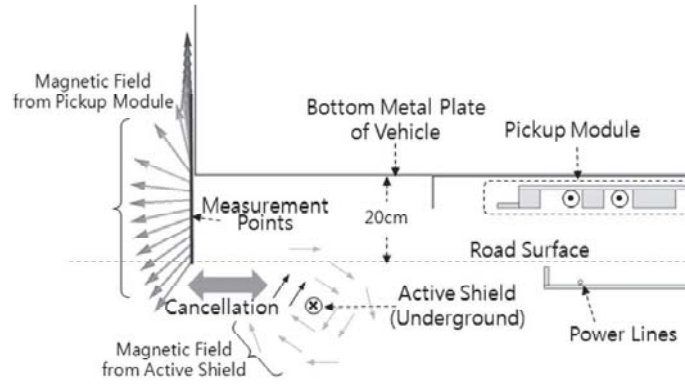
Figure 5.7: OLEV system with active and power lines and active field shielding [31].

A link efficiency of 80% was achieved at a distance of 20 cm, but no details of the end-to-end efficiency are given. Furthermore, no details of misalignement tolerances are given, but due to the power line magnetic field generation and the ferrite material of the receiver coil, it is expected that the passenger bus needs to drive precisely between the two power lines, as shown in [151, 152]. To increase the horizontal tolerance of the OLEV system, and avoid the use of the active and passive shielding techniques described above, a system with I-beam power rails was used to transfer 27 kW, with an end-to-end efficiency of 74%, at a distance of 20 cm [32]. The system has a H-bridge driver working at 20 kHz and a full-bridge rectifier on the receiver. Both the power rail and the receiver have ferrite material, as shown in Fig.5.8.

The direction of the current through the cables and the ferrite I-beams generates magnetic poles that have a maximum H-field strength in the centre of the I-beam and allow for 50% end-to-end efficiency with a horizontal misalignment of 24 cm.
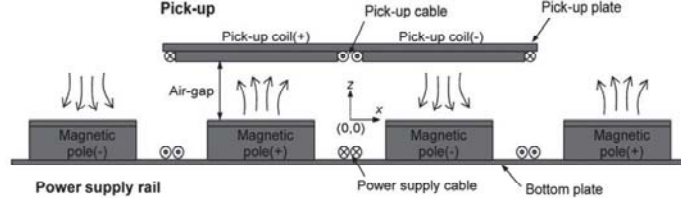
Figure 5.8: I-beam magnetic pole power rail with ferrite receiver coil. [32].

The different polarity of neighbouring I-beam poles helps to cancel the field at a distance of 1 m, where the magnetic flux was below the 6.25 μT ICNIRP maximum level at 20 kHz.

5.3.2 Optimal Frequency

In order to avoid the use of heavy and expensive field shaping techniques, the system can be driven at an optimal frequency where the unloaded quality factor of the TX and RX coils is large enough to compensate for the low coupling coefficient. An example of this was described by Kurs *et al.* [131], where two coreless copper helical coils of 60 cm diameter were driven at 9.9 MHz, by a Colpitts oscillator. This system achieved an end-to-end efficiency of 15%, with a link efficiency of 50%, for 60 W of received power. The link efficiency was high at a separation distance of 2 m, due to coil unloaded Q-factors being above 950, even with coupling factors of less than 0.02. The low end-to-end efficiency was due to a high impedance mismatch and the use of a COTS driver, which was not designed for high efficiency operation at high frequencies and high power levels.

Other alternatives to the Colpitts oscillator are half or full-bridge converter circuits, but a frequency control or variable resonant tank is required to achieve driver efficiencies above 40% for a wide range of loads [153, 154] and extend the efficiency of the link. An alternative to this is a Class-E amplifier that is capable of achieving a zero-voltage and zero-current operation at the time of switching [155].

A Class-E driver is very sensitive to load changes and, therefore, it is difficult to achieve good operation under a variable load [156]. This is the case when powering a device that is used for charging a battery. If the load impedance varies while it is charging or the coupling of the IPT system changes due to misalignments, the

system should be capable of achieving a high efficiency, ideally without complex control systems.

To achieve this, Class-E component selection was optimized across a wide range of loads to operate at high end-to-end efficiency $\eta_{ee} > 50\%$ [33]. A capacitor was placed in parallel with both coils, to change both the resistive and reactive parts of the impedance. If a series capacitor was used instead, only the reactive part would be changed. The parallel tank provides more control on the receiver and the transmitter impedance and allows, in the case of low coupling, to have an effective resistance that is larger than the series coil resistance of the transmitter and allows power to be transferred efficiently to the reflected RX resistance .

In [157] a Class-E amplifier was used because it can operate more efficiently at higher power levels than a Class-D and at a lower input voltage . In addition, in [33] a double-sided Class-E with independent gate drive was used to increase the efficiency for low and high-power requirements, as illustrated in Fig. 5.9.
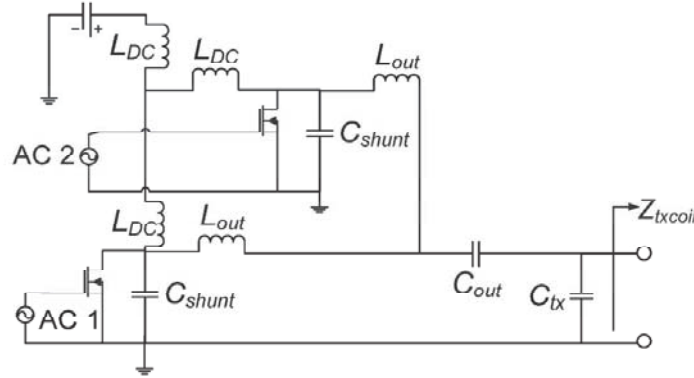
Figure 5.9: Double-side Class-E amplifier with independent gate drives. [33].

Under low-power operation, one of the gate drivers is turned off and the equivalent inductance towards the TX coil is halved, while the shunt capacitance is doubled. Although it is easy to scale the number of channels, the device mismatches might generate an unstable operation. Such is the case of using more than four channels, where the efficiency starts to drop due to MOSFET, inductor and capacitor tolerances. It is important to note that the extra inductors reduce the efficiency of the system.

The TX and RX resonant tank capacitors, as well as the Class-E capacitors, were

selected by sweeping the expected input impedance of a regulator, while charging USB input consumer electronics with an expected impedance between 25 and 100 Ω [158]. The TX coil was 21 x 21 cm^2 and the RX was 13 x 13 cm^2, while the separation distance was 0 cm and the coupling was larger than 0.4. The coils' unloaded Q was maximized by selecting the optimal frequency of operation, although it was constrained to the operating frequency of the MOSFET used in the driver. The coils were characterized with an impedance analyser at the operating frequency and Q-factors of 84 and 52 were measured at 134 kHz for the TX and RX coils, respectively.

A full-wave rectifier was used on the receiver side and the losses, due to voltage drops and reverse recovery, were said to be negligible when compared to the 300 W of power delivered to the load. The system was able to achieve a 77% end-to-end efficiency for a load that varied between 60 and 110 Ω. It is important to note that, for 95 W of delivered power, the Class-E MOSFET and inductor required forced-air cooling to operate under component specifications, and the power from the fan was not taken into account in the end-to-end efficiency measurements [33].

Four-coil systems, as shown in Section 5.3.1, require complex and lossy impedance matching networks. In addition to efficiency loss, the impedance matching networks need to be tuned every time the misalignment changes, thus restricting the misalignment tolerance of the system to the bandwidth of the matching network. To increase the link efficiency of the system when the separation distance between the multiturn resonator coils increases, without coupling enhancement techniques, the coupling between the driver and its resonator and the receiving loop and its corresponding resonator can be modified to achieve a good impedance match. This can be achieved without requiring a lossy impedance matching network, as long as all coil resonant frequencies are identical [159]. This solution works very well for scenarios where the distance between the load and the transmitter is static. To further increase the link efficiency, Q-factors above 300 were achieve with an operating frequency of 6.7 MHz. The system was able to achieve a link efficiency of 92.5% at a distance of 15 cm and 30% at a distance of 60 cm [159].

Following the same approach of increasing the Q-factor by increasing the frequency of operation, and designing a driver that can tolerate misalignment conditions, a Class-D driver was used to increase the separation distance and achieve a medium range (100 cm) wireless power transmission, see Figure 5.10 [34].
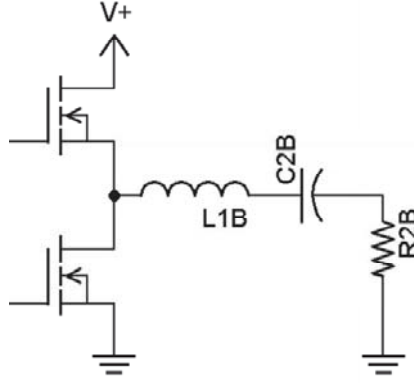
Figure 5.10: Class-D amplifier topology [34].

Although a Class-E amplifier can achieve a higher efficiency than a Class-D driver, the Class-D was selected because the component voltage ratings required in a Class-E are considerably higher, and thus more difficult to obtain. A Class-D amplifier has a similar topology to that of a buck converter, but the main difference is that the Class-D supplies changing voltage and current to a load, while the buck converter provides a constant dc voltage. In addition, the Class-D switches with zero voltage, although a current is present while switching. A major setback of the Class-D topology is that the there is no parallel capacitance to the drain and source of the MOSFET, as shown in Fig. 5.10. Due to this, the output capacitance of the MOSFET limits its power handling capabilities. When a parralel capacitor can be added to the drain and source, the total capacitance can be designed to achieve higher power levels.

In [34] a Class-D was operated at 508.5 kHz to drive two square meter Litz wire coils and achieve a link efficiency of 76%, at a distance of 1 m and with a transmitter angle variation of up to 35°. The coupling factor value was 0.023, according to HFSS simulations, up to this rotation angle. Furthermore, the transmitted power was limited to 35 W, due to the tolerance of the Litz wire isolating compound.

A team from the University of Washington, working in collaboration with Intel Labs, exploited a key fundamental phenomenon in IPT resonant systems, namely

frequency splitting [35]. The conventional analogy to a resonant system is comparing the resonant coils to two pendulums that are linked together by a spring having a specific stiffness (equivalent to the coupling factor of an IPT system). The spring's stiffeness is linked to the frequency of ocillation of the two pendulums. As the stiffeness increases so will the separation of the oscillating frequencies of the pendulums, causing what is known as a frequency split. As the spring stiffness decreases the two pendulums start to oscillate like a single pendulum, this situation is defined as critical coupling. Past this point, as the coupling decreases the rate of energy transfer will decrease as well. Fig. 5.11 shows the transmission coefficient (S_{21}) measurement of a 4 coil IPT system.
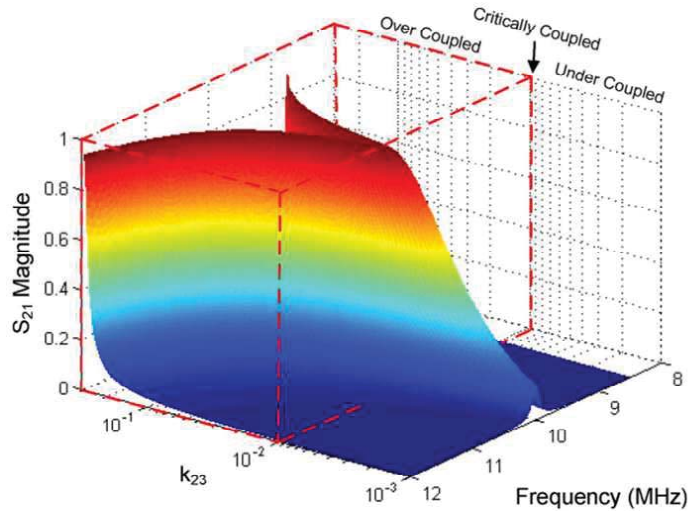
Figure 5.11: S_{21} measurements showing (red box) the over-coupled and critically-couple region of an IPT system vs frequency and separation distance. [35].

As can be clearly seen, two modes are generated in what is called the over-coupled region. In this region, operating at any of the two frequencies will give the same link efficiency, as is the case for the critically-coupled point. The region outside this red box is called the under-coupled region. The critical coupling can also be appreciated in Figure 5.12, where the critical coupling is found around 0.7 m.

To achieve the maximum link efficiency possible, coils with Q-factors around 350 were used, together with frequency tuning and impedance matching at 7.65 MHz. The coil dimensions were 28 cm in diameter for the driving and receiving loops and 59
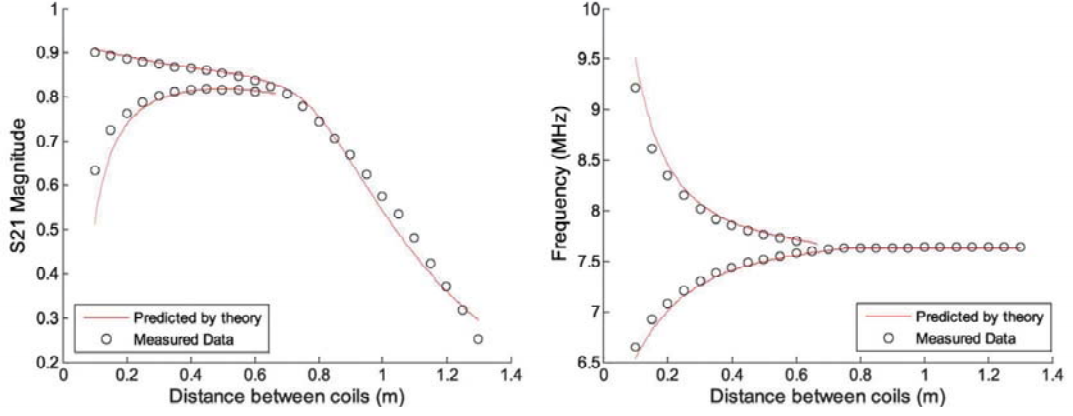
Figure 5.12: S_{21} simulations and measurements (left) and frequency (right) vs. distance. Frequency splitting can be appreciated on distances lower than 0.7 m [35].

cm for the resonant coils. To measure the unloaded Q-factors, a transmission type measurement with a vector network analyser (VNA) was used. This method will be discussed in the following chapter. To account for separation distance or angular misalignment, the operating frequency needs to match either the over-coupled modes or the critically-coupled point. This was achieved by placing a directional coupler between the driver and the impedance matched 50 Ω loop, as shown in Fig. 5.13. The coupler allows a power meter to measure the transmitted and reflected power, while a frequency sweep is performed, and the frequency is selected where the maximum transmitted power is detected.

Another way of tuning the system, for different misalignment conditions, is with variable impedance matching networks. Both solutions achieved link efficiencies higher than 75% at a distance of 70 cm and at receiver angles as high as 60° [35].

A research team from Samsung reached Q-factors of 1450 for large 30 x 40 cm^2 copper wire coils, driven by 50 Ω loops at 13.56 MHz [36]. To maximize the end-to-end efficiency of the system, a frequency tracking algorithm was implemented to operate in both the over-coupled ($D < 25$ cm) and under-coupled regions. By varying the frequency, reasonably good impedance matching was accomplished without having a variable matching network. The power levels at both the TX (output of Class-E amplifier) and RX (at the load) were measured with directional couplers and a power meter. The power measured at the RX was relayed to a phase-locked
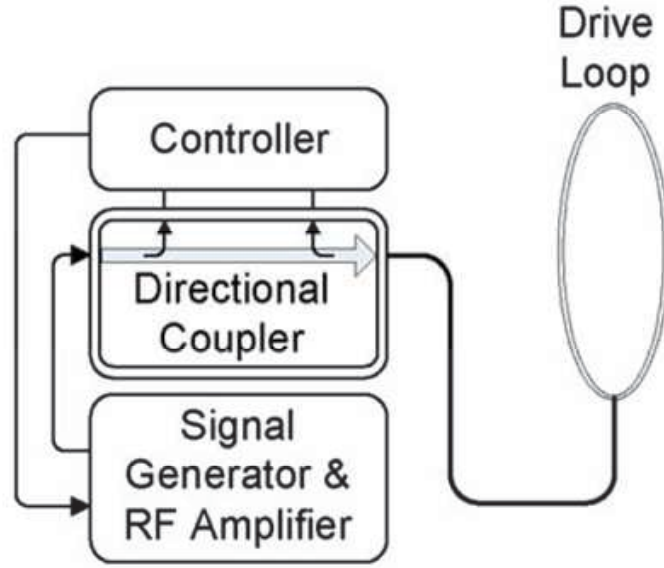
Figure 5.13: Frequency tuning system schematic for driving a 50 Ω driving loop [35].

loop to control the driver's frequency via a 2.45 GHz ZigBee wireless link and dipole antennas, as shown in Fig. 5.14. The system was able to achieve link efficiencies above 85%, for a variable separation distance between 30 to 50 cm.
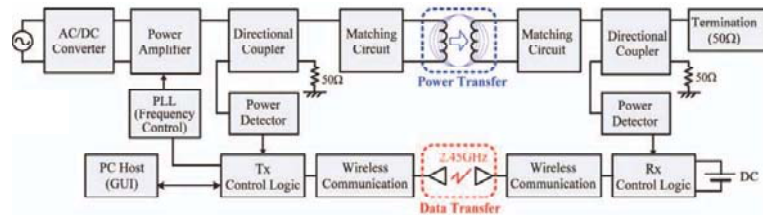
Figure 5.14: Automatic frequency control block diagram with 2.45 GHz ZigBee wireless link [36].

In another IPT system design, different resonant tank topologies were analysed to extend the efficiency of the system for situations where the separation distance between coils needs to be increased without tuning techniques. If the separation distance is past the critical coupling point, the system will not be able to achieve the maximum link efficiency. Fig. 5.15 shows the different resonant tank topologies that are normally used for IPT systems. In [37], a new topology is presented to extend the over-coupled and critically coupled region. Insertion loss measurements showed that a mixed series-shunt tank topology proved to have a critical coupling factor, which was ten times smaller than the series topology, albeit with a lower
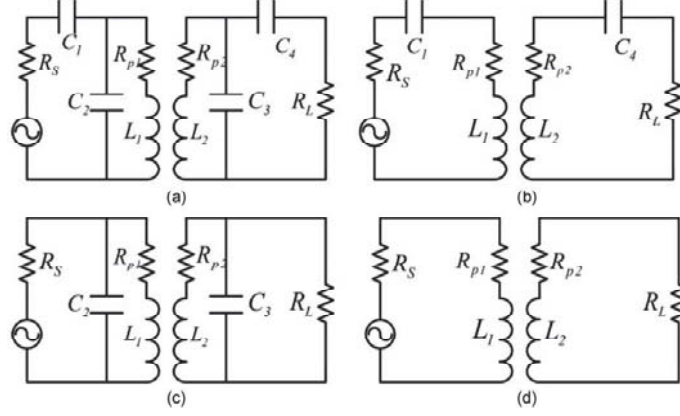
Figure 5.15: Resonant tank topologies for IPT systems (a) mixed series-shunt, (b) series, (c) shunt and (d) self resonant [37].

link efficiency than the shunt topology - due to the extra added component losses. Using a conventional 50 Ω output impedance Class-E amplifier and an impedance matching network, the resonant coils were driven at a frequency of 4 MHz for an unloaded $Q = 300$. The mixed-resonant system was able to achieve a dc-to-load efficiency of 50 % at a distance of 20 cm and with 4 W of transmitted power.

As shown in the above-mentioned coil designs, normally fabricated with Litz wire or copper wire, unloaded Q-factors above 500 are difficult to achieve, even at operating frequencies between 1 and 10 MHz. Achieving a high Q-factor is essential to decrease the losses and maximize the end-to-end efficiency of the system. This is of particular importance for medium to high power systems (> 50 W), where high losses may overheat the system or make IPT technology an unattractive power alternative to tethered technology.

As stated in the previous section, skin and proximity effect losses dominate the coil losses at high frequencies. Although a large cross sectional area of the conductive material and spacing between turns helps to alleviate these problems, for many applications a large helical coil might not meet the size constraints.

To optimize the coil design, in [38] several finite element analysis (FEA) simulations were performed for different cross sectional areas. The solid copper wire had the highest effective series resistance, because there is concentrated and opposing current inside the wire; as opposed to the hollowed conductors, illustrated in

131

Fig. 5.16.
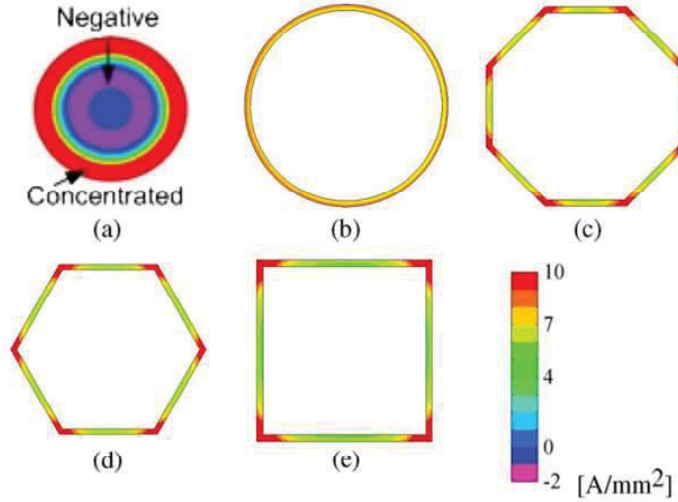
Figure 5.16: Current density distribution of cross-sectional areas on simulated conductors (a) solid circular , (b) hollow circular, (c) hollow octagonal (d) hollow hexagonal and (e) hollow square [38].

In addition, the polygonal conductors have a higher effective resistance, since the current is not distributed evenly through the conductor and is concentrated in the corners. Proximity effect on multi-turn coils creates a concentration of current in the external outermost part of the conductors. This phenomenon contributes more than skin effect to an increased coil series resistance.
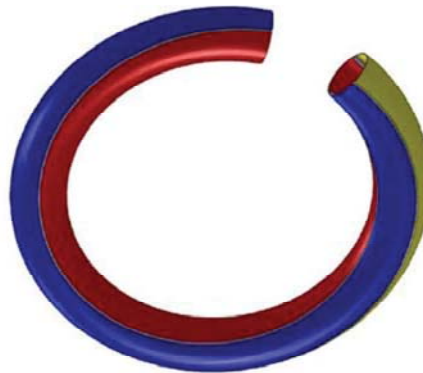
Figure 5.17: Three turn surface spiral with circular cross-sectional area [38].

A surface spiral was designed to decrease the proximity effect, as illustrated in Fig. 5.17 [38]. The surface spiral has an even distribution of current, thus resulting in an even magnetic field around the coil. The spiral can be fabricated by copper plating a circular glass tube. Simulations of a three turn surface spiral show that

132

the self inductance is the same as that of a three turn copper wire or Litz wire coil, but the series resistance is less than 50 %; therefore, the unloaded Q-factor can be increased, as will be shown in the next chapter. These results make the surface spiral an ideal candidate for high power IPT applications.

5.4 Conclusion

This chapter presented the early applications of inductive power transfer systems, *i.e.* mainly implantable medical devices, which helped develop the theory, initial approaches and challenges of transferring power wirelessly. Based on the technology developed for these applications, the main building blocks of an IPT system were presented. This analysis highlighted the importance of designing a system that is capable of achieving high overall efficiencies and not only high link efficiencies.

As summarized in the literature review, the main design approaches for loosely coupled IPT systems have concentrated on either coupling enhancement techniques or Q-factor maximizing by operating at the optimal frequency. Both of these approaches increase the link efficiency and only a couple of designs take into account the full system's efficiency.

Table 5.1 summarizes and compares the IPT designs presented in this Chapter. In this table, η_{link}, $\eta_{dc-load}$ and η_{ee} have been separated out, where possible, to highlight that dc-to-load efficiency can be substantially lower than the transfer efficiency. It is interesting to note that the highest η_{ee} values have been demonstrated by all the commercial IPT systems currently available on the market. As said before, high efficiencies of $\eta_{ee} = 90\%$ have been achieved at distances of less than 30 cm but with relatively heavy systems (30-40 kg) that use field shaping ferromagnetic materials.

The main disadvantages of using coupling enhancement techniques is that the system is more sensitive to offset, distance or other misalignment scenarios, due to the static field shaping provided by using ferromagnetic materials. In addition, coupling enhancement techniques are expensive, heavy and mostly cumbersome to implement. This is the case of using metamaterial structures between two coils to increase the separation distance.

Table 5.1: IPT Systems Comparison

D [cm]	fo [kHz]	Driver Technology	Coil Technology	Magnetic Material	P_{load} [W]	η_{link} [%]	$\eta_{dc-load}$ [%]	η_{ee} [%]	Ref.
0	134	Class-E	Litz wire	No	295	-	-	75.7	[33]
0	240	Class-E	Litz wire	No	3.7	71	-	66	[158]
10	20	H-bridge	Litz wire	Yes	2,000	85	-	-	[28]
10	-	-	-	Yes	3,300	-	-	90	[29]
15	6,700	HF transceiver	Loop + pancake coil	No	-	93	-	-	[159]
15	20	H-bridge	Litz wire	Yes	2,000	95	-	-	[139]
18	145	-	Litz wire	Yes	300-3,000	-	-	90	[143, 144, 160]
20	4,000	Class-E	Copper wire coil	No	2	-	50	-	[37]
20	20	H-bridge	Power lines	Yes	60,000	80	-	-	[31]
20	20	H-bridge	Power rail	Yes	27,000	-	-	74	[32]
30	3,700	HF transceiver	Surface spiral	No	220	95	-	-	[38]
18-30, 40*	20	H-bridge	-	Yes	3,000	-	-	> 85	[141, 142]
70	7,650	Signal generator	Loop + pancake coil	No	30	75	-	-	[35]
50	13,560	Class-E	Loop + rectangle coil	No	70	85	70**	-	[36]
50	27,000	HF transceiver	Loop + spiral coil	No	40	47	-	-	[30]
100	508.5	Class-D	Litz wire	No	5-35	76	-	-	[34]
200	9,900	Colpitts oscillator	Litz wire	No	60	50	-	15	[131]

*Maximum power transfer distance stated in the cited website [141]

**Calculated based on estimated value of η_{driver} [36]

In contrast, without coupling enhancement techniques, optimal frequency selection can allow an IPT system to be lightweight, while still achieve high Q-factors to compensate for low coupling factors. This approach presents its own difficulties, mainly due to the limitation of existing driving circuit topologies capable of operating at the optimal frequencies (tens of MHz), while working at medium power levels. This can be appreciated in Table 5.1, where all high power systems work below 200 kHz. Almost all of these high power IPT systems use conventional inverter topologies, such as a H-bridge. This circuit topology cannot achieve high efficiency at high frequencies and therefore, for high frequency IPT systems, signal generators and high-frequency transceivers were used. These COTS drivers dropped the dc-to-load efficiency of the system, since they were not designed to work at high power levels. To overcome this, different amplifier topologies have been used, such as Class-D and Class-E. These topologies proved to be more efficient due to their zero-crossing operation. In addition to the amplifier losses, complex and lossy impedance matching networks are required to match the TX coil to the 50 Ω impedance of both standard and bespoke drivers. This is also the case for high frequency systems that used 4 coil topologies, where a driving and receiving loop are used to match the 50 Ω termination of the system. Nevertheless, standard impedance systems have the advantage of allowing available RF systems, such as antenna tuners, decouplers and phase-locked loops to be easily implemented. Applying standard techniques and equipment to control IPT systems has proven to decrease the misalignment and distance sensitivity of the system, allowing for higher efficiencies across different scenarios. Alternatively, for systems that avoid a standard impedance, a sensitivity analysis on the driver's components, as well as the coupling factor region, helps to increase the distance and angular variation tolerance.

Even with high frequency driving systems, few attempts have been able to accomplish unloaded Q-factors above 1000. Complex Litz wire assemblies have been tested, but Litz wire can avoid skin and proximity effect losses only up to a few MHz. Therefore, high Q-factors with Litz wire have not been achieved. Alternatives to this approach have been presented by using copper wire and surface spirals.

The key elements to achieve high Q-factors with these two coil designs are selecting a conductor geometry that avoids current concentration and minimizing proximity effect losses between turns, which also create an uneven distribution of current, as shown before.

The challenge then is to realise a high frequency, cost effective and efficient solution for mid-range IPT in the absence of field-shaping techniques, allowing a light-weight system to be achieved. A system with a TX-RX coil size difference represents a more realistic system, where the receiver size is usually constrained by its application. This system must be able to achieve high efficiency for lower coupling factors, due to the smaller RX coil size. Furthermore, this system must be able to achieve high efficiencies even under situations where perfect alignment is not always achievable (*e.g.* aquatic wireless sensor charging). It is important to note that magnetic field exposure limits will not drive the design of the system, due to the aquatic scenario (no human presence) for which the system is intended.

The next sections show how the findings from the literature review prompted the design of high Q/light weight coils, as well as an efficient driver design. These factors, linked to a system optimization approach, are then used to achieve a high dc-to-load efficiency for wireless power transmission.

6 System Design

6.1 Introduction

Chapter 5 presented a review of existing work and the basic building blocks required for transferring power via an inductively coupled system. As demonstrated in the open literature, many research teams have successfully achieved high link or transfer efficiencies but have neglected the overall system performance. This chapter analyses the details of each one of the building blocks of an IPT system, to provide a new insight into how to manage and combine all the different variables that are key to increase the efficiency of the complete system. The system optimization approach that is presented in this chapter demonstrates how the efficiency of each building block can be increased even further if the system's efficiency is considered.

To identify suitable coil topologies for transferring efficiently tens to hundreds of watts across an air gap of tens of centimetres, a detailed analytical study and simulations were performed. These are presented here to highlight the system constraints and variables that are required to increase the link efficiency. One of these key variables is the frequency at which the transmitting coil has to be driven, in order to achieve a high quality factor on both coils. Furthermore, the system that is presented here has coil size and weight restrictions, since its initial application was intended for charging (wirelessly) water sensors from an unmanned aquatic vehicle. This application required the coils to have 30 cm and 20 cm diameters for the transmitter and receiver, respectively due to the size of the kayak and buoy. As will be shown in this Chapter, having a smaller receiver adds constraints to the efficiency of the complete system.

Several driver and amplifier technologies have been used to drive IPT systems but

few of these are capable of achieving the required power and frequency efficiently. Class-E amplifiers have been identified as ideal drivers for IPT applications, but their power handling capability at tens of MHz has been a crucial limiting factor, since the load and inductor characteristics are set by the requirements of the resonant inductive system. The frequency limitation of the driver restricts the unloaded Q-factor of the coils and thus the link efficiency. With a suitable driver, copper coil unloaded Q-factors of over 1,000 can be achieved in the low MHz region, enabling a cost-effective high Q coil assembly. The system presented in this chapter alleviates the use of heavy and expensive field-shaping techniques, by presenting an efficient IPT system capable of transmitting energy with a dc-to-load efficiency above 77% at 6 MHz, across a distance of 30 cm.

As a result of a bespoke Class-E amplifier design, for the fabricated coils presented in this work, complicated tuning techniques for misaligned scenarios are not necessary to achieve an efficient power transfer, even with skewed and displaced transmitting and receiving coils. An easy to implement, although not ideal, frequency tuning technique allows the system to achieve, in some misalignment scenarios, close to constant efficiency operation.

This chapter provides an overview of IPT theory, outlining the system architecture and key component selection that define the system's end-to-end and dc-to-load efficiencies. Cost-efficient coil design, simulations and measurements to achieve dc-to-load efficiencies above 70% for sub-metre distances are reported.

6.2 IPT theory

With the typical IPT systems architecture, shown in Fig. 5.3, the driver provides high frequency power to the TX coil, having an unloaded quality factor Q_{TX}, which couples as defined by k to the RX coil, having an unloaded quality factor Q_{RX}. It is well known that by using receiver (or secondary) resonance and optimising the load

impedance, the link efficiency can be maximized to give [161]:

$$\eta_{link} = \frac{k^2 Q_{TX} Q_{RX}}{(1 + \sqrt{1 + k^2 Q_{TX} Q_{RX}})^2} \qquad (6.1)$$

Each of the different components that constitute this equation will be explained in this section.

As can be seen from (6.1), the key to achieving high efficiency is to maximise $k^2 Q_{TX} Q_{RX}$, as shown in Fig. 6.1. To understand how to select the appropriate IPT topology and what key variables need to be optimized to increased the link efficiency, a detailed analysis, based on [41], is presented.
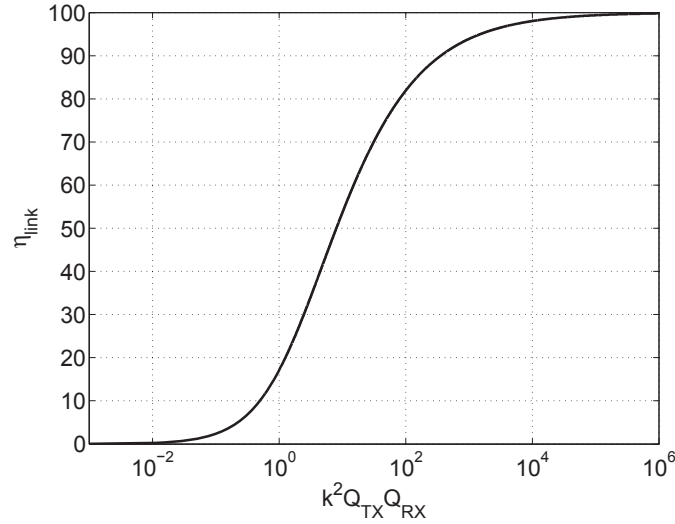
Figure 6.1: Link efficiency variation as a function of the dominating factor $k^2 Q_{TX} Q_{RX}$.

6.2.1 Optimal Load

To optimize the link efficiency, an optimal load impedance has to be selected. To achieve this, analytical expressions were introduced in [41], where the optimal load will vary depending on the selected IPT system configuration, of which there are six combinations. The transmitter can be non-resonant or achieve resonance by a capacitor in series or in parallel with the transmitter coil and the receiver can also be series resonant or parallel resonant.

The receiver or secondary resonance is needed to cancel the receiver coil leakage

inductance that contributes to losses in the transmitter, by forcing the voltage and current in the TX coil to increase.RX series resonance can only be used if the self-capacitance or parasitic capacitance of the inductor is assumed to be negligible. In contrast, this assumption is not needed in the parallel case, since the parallel resonator capacitor can absorb the parasitic capacitance of the coil. This also has the advantage of allowing higher operating frequencies, and therefore, smaller coils for applications where the receiver needs to be miniaturized. Furthermore, the coupled RX coil is always assumed to be operating at resonance; this way the equivalent optimal load on the transmitter, reflected from the receiver, will only be resistive, affecting only the damping of the transmitter tank [39, 41]. As will be described in Section 7.2, the transmitter in this work will be non-resonant, since an efficient Class-E driver topology was selected for driving the TX coil under very low coupling conditions, $k < 5\%$. It will be shown that this driver topology avoids a freewheeling operation, common for low coupling links, and its operation is based on having a non-resonant transmitter. The following analysis will therefore concentrate on analysing a non-resonant TX with a parallel resonant RX.

In this topology, the link efficiency is [41]:

$$\eta_{link} = \frac{k^2 Q_{TX} Q_{RX}^2}{\left(1 + \frac{Q_{TX}}{Q_L} + k^2 Q_{TX} QRX\right)(Q_L + Q_{RX})} \tag{6.2}$$

where $Q_L \equiv \omega_o C_{resRX} R_{load}$, ω_o is the operating frequency of the IPT system and the angular frequency of the receiver, C_{resRX} is the receiver's resonant tank capacitor and R_{load} is the resistive load on the receiver. It is important to note that (6.2) is also applicable to resonant transmitter topologies.

To maximize the link efficiency for a low coupled link, the optimal Q_L will be given by the inflection point of (6.2). For any given application where the TX and the RX coils are size constrained, as is the case of this work, the coils inductances and quality factors will be known. This gives the value for the optimal α as follows:

$$Q_{Lopt} = \frac{Q_{RX}}{\sqrt{1 + k^2 Q_{TX} Q_{RX}}} \tag{6.3}$$

Using α_{opt} to calculate the optimal load gives:

$$R_{load} = L_{RX}\omega_o \frac{Q_{Lopt}^2 + 1}{Q_{Lopt}} \tag{6.4}$$

where L_{RX} is the self inductance of the receiver. Substituting Q_{Lopt} in (6.2) gives (6.1). Once the link efficiency has been maximised, the link gain A_{link} can be calculated, since only the amplitude at a specific frequency ω_o is wanted

$$A_{link} = \frac{kn_{Lcoil}Q_{TX}}{1 + \sqrt{1 + k^2 Q_{TX}Q_{RX}}} \sqrt{\frac{1 + k^2 Q_{TX}Q_{RX} + Q_{RX}^2}{1 + k^2 Q_{TX}Q_{RX} + Q_{TX}^2}} \tag{6.5}$$

where the n_{Lcoil} is the coil inductance ratio defined by:

$$n_{Lcoil} = \sqrt{\frac{L_{RX}}{L_{TX}}} \tag{6.6}$$

where L_{TX} is the self inductance of the transmitter coil. With the optimal load defined, the rest of the parameters that increase the link efficiency are now analysed.

6.2.2 Coupling Factor

The coupling coefficient can be calculated with analytical expressions to confirm any assumptions during full wave simulation and experimentation. The coupling factor is related to the mutual and self inductances as follows:

$$k = \frac{M}{\sqrt{L_{TX}L_{RX}}} \tag{6.7}$$

where M is the mutual inductance and k can vary between 0 and 1. One meaning that both coils have exactly the same magnetic field and zero that the coils are fully decoupled. In addition, the self inductance L of a coil is calculated as follows:

$$L = N^2 r \mu_o \left\{ ln \left[\left(\frac{8r}{a} \right) - 2 \right] \right\} \tag{6.8}$$

where N is the number of turns, r is the radius of the coil, and a is the radius of the coil conductor. The vast amount of literature available on self inductance models

is due to the interest in achieving a high degree of precision when calculating L. Examples of closed analytical expressions and working formulae using approximation methods can be found in [49, 162, 163].

A good approximation for k can be found by applying the following analytical formula for two single turn loops that face each other. This formula provides a good approximation where the transmitter radius r_{TX} and the receiver radius r_{RX} comply with $r_{TX} \geq r_{RX}$ [49].

$$k = \frac{r_{TX}^2 r_{RX}^2}{\sqrt{r_{TX} r_{RX}} \left(\sqrt{r_{TX}^2 + D^2}\right)^3} \tag{6.9}$$

In the case where $r \ll D \ll \lambda$, where λ is the free space wavelength of the coil's driving signal, the coupling factor can be approximated as follows [164]:

$$k = \frac{M}{2\sqrt{L_{TX} L_{RX}}} \tag{6.10}$$

and, the mutual inductance M is:

$$M \approx \frac{\pi \mu_o \left(r_{TX} r_{RX}\right)^2}{2D^3} \tag{6.11}$$

where μ_o is the permeability of free space. From (6.10) and (6.7) the coupling factor is approximated as indicated below:

$$k \approx \frac{\left(r_{TX} r_{RX}\right)^{3/2}}{2D^3} \tag{6.12}$$

6.2.3 Quality Factor

The third important factor required to increase the efficiency of the power transfer is the quality factor of the coils. The quality factor or Q-factor describes how underdamped an oscillator is, or in other words, how much energy is lost per cycle compared to the energy that is stored. The Q-factor can also be used as a dimensionless figure of merit to compare different coil configurations. To achieve good link efficiencies for the present application, where k is typically around 0.01 for medium range air-gaps (10s of cm), the unloaded Q of the coils has to be above

1000. Achieving these values can be complicated and commercially available coils can only achieve Q-factors on the order of a few hundreds. A clear explanation of how the Q-factor can be maximized by choosing the correct operating frequency was described by Yates *et al.* [165] and the following section describes how to apply the relevant theory to IPT systems.

The Q-factor is calculated using the following equation:

$$Q = \frac{\omega L}{R} \tag{6.13}$$

where ω is the angular frequency and R is the equivalent series resistance of the coil. The series resistance is made by the radiation resistance R_{RAD} and the skin effect resistance R_{skin}.

$$R = R_{rad}(\omega) + R_{Skin}(\omega) \tag{6.14}$$

The radiation resistance can be seen as an analogous to ohmic resistance, where the main difference is that with radiation resistance energy is lost when it is converted to electromagnetic radiation, and with ohmic resistance energy lost when it is converted to heat. The radiation resistance of an electrically small multi-turn coil (loop antenna) is given by [166]:

$$R_{rad}(\omega) = N^2 \eta_o \left(\frac{\pi}{6}\right) (\beta_o(\omega)r)^4 \tag{6.15}$$

where η_o is the impedance of free space and the wave number $\beta_o(\omega) = 2\pi/\lambda$. This resistance is caused by the radiation of electromagnetic waves from the coil, due to the conduction of electrons, and is solely related to the geometry of the coil and not its material.

The skin effect resistance is due to a physical phenomena present within a conductor that is carrying alternating current; whereby the concentration of electrons will be higher closer to the surface (skin) of the conductor and will decrease exponentially into the conductor. The resistance due to the skin effect will increase as the frequency increases as described by the skin depth formula:

$$\delta = \sqrt{\frac{2}{\sigma\omega\mu}} \tag{6.16}$$

where δ is the classical skin depth, σ is the bulk conductivity at dc and μ is the permeability of the medium. If $\delta \ll 2a$ then the cross sectional area, A through which the current flow is:

$$A = 2\pi a\delta \tag{6.17}$$

Using (6.16) and (6.17) and the length of the coil being $l = 2\pi rN$, R_{skin} is [166]:

$$R_{skin}(\omega) \approx \frac{Nr}{a}\sqrt{\frac{\mu\omega}{2\sigma}} \tag{6.18}$$

In addition to the skin effect losses, the proximity effect losses should be taken into account for a multiturn coil, since the current distribution is not uniform, and for closely wound coils the proximity effect losses may dominate [167]. To take this into account and achieve accurate results, the losses due to the skin and proximity effects were calculated using Butterworth's numerical model [168, 169] and verified with full-wave simulations, as will be shown in Section 6.3. This makes equation (6.18) a useful approximation of skin-effect resistance that allows for a clear interpretation of the variables that increase or decrease the Q-factor

If it is assumed that $a = 1$ cm and $\delta = 27$ μm at 6 MHz and that the coil losses are dominated by the skin effect losses, the Q-factor can be approximated by substituting (6.8) and (6.18) in (6.13):

$$Q \approx \frac{\omega N^2 r\mu_o \left\{ ln\left[\left(\frac{8r}{a}\right) - 2\right]\right\}}{\frac{Nr}{a}\sqrt{\frac{\mu\omega}{2\sigma}}} \tag{6.19}$$

$$Q \approx Na\mu_o\sqrt{2\sigma\omega\mu}\left\{ ln\left[\left(\frac{8r}{a}\right) - 2\right]\right\} \tag{6.20}$$

To maximise Q, it is clear that the frequency, the number of turns and the wire radius for a given coil radius should be maximised. Clearly, for a given coil diameter there is a limit on the number of turns possible for a given wire radius.

As stated before, to increase the link efficiency, $k^2 Q_{TX} Q_{RX}$ has to be maximised.

To do this, a closed-form expression can be found by using (6.12) and (6.20), assuming that the radiation resistance is negligible at low frequencies and that both coils are fabricated with the same wire characteristics.

$$k^2 Q_{TX} Q_{RX} \approx \frac{r_{TX}^3 r_{RX}^3}{D^6} N_{TX} N_{RX} a^2 \mu_o^2 2\sigma\omega\mu$$
$$\left\{ ln\left[\left(\frac{8r_{TX}}{a}\right) - 2 \right] \right\} \left\{ ln\left[\left(\frac{8r_{RX}}{a}\right) - 2 \right] \right\} \qquad (6.21)$$

If the operating frequency is increased, the radiation resistance R_{rad} dominates. Substituting the circumference to wavelength ratio $c_\lambda = \omega r/c$ in (6.15), where c is the speed of light, gives:

$$R_{rad}(\omega) = N^2 \eta_o \left(\frac{\pi}{6}\right) c_\lambda^4 \qquad (6.22)$$

Substituting (6.8) and (6.15) in (6.13):

$$Q = \frac{6\mu_o c^4 \left\{ ln\left[\left(\frac{8r}{a}\right) - 2 \right] \right\}}{\eta_o \omega^3 r^3 \pi} \qquad (6.23)$$

To maximise $k^2 Q_{TX} Q_{RX}$ when R_{rad} dominates:

$$k^2 Q_{TX} Q_{RX} = \frac{36\mu_o^2 c^8 \left\{ ln\left[\left(\frac{8r_{TX}}{a}\right) - 2 \right] \right\} \left\{ ln\left[\left(\frac{8r_{RX}}{a}\right) - 2 \right] \right\}}{D^6 \eta_o^2 \omega^6 \pi^2} \qquad (6.24)$$

Having the expressions that approximate the $k^2 Q_{TX} Q_{RX}$ when the skin effect losses dominate and when the radiation losses dominate, it can be inferred that with a given set of coil dimensions the frequency of operation should be increased until $R_{rad} \approx R_{skin}$, thus:

$$N^2 \eta_o \left(\frac{\pi}{6}\right) c_\lambda^4 = \frac{Nr}{a} \sqrt{\frac{\mu\omega}{2\sigma}} \qquad (6.25)$$

$$\frac{r}{a} \sqrt{\frac{\mu\omega}{2\sigma}} = 20\pi^2 N c_\lambda^4 \qquad (6.26)$$

In addition, the size of the coils needs to be kept below a tenth of a wavelength to avoid radiation by having an electrically small antenna. As an example, if we assume a coil with $r/a = 20$:

$$c_\lambda = \left(\sqrt{\frac{\mu}{2\sigma\pi^4}}\right)^{1/4} \frac{\omega^{1/8}}{N^{1/4}} \tag{6.27}$$

$$c_\lambda = 0.01 \frac{\omega^{1/8}}{N^{1/4}} \tag{6.28}$$

For a coil with $N = 1$ and $f = 40$ MHz, $c_\lambda = 0.11$. Without taking into account proximity effect, the optimal length of the coil will be close to 0.1 wavelengths, matching the limit of an electrical small coil. For this work, where the primary and secondary coils are limited to different sizes, the optimal frequency will be determined by the larger coil. Beyond the frequency at which the radiation resistance begins to dominate the losses of the larger coil, $k^2 Q_{TX} Q_{RX}$ will decrease with ω^6 instead of increasing with ω, as shown by (6.24) and (6.21), respectively. Since k is independent of frequency, it is clear that the optimal frequency will correspond to that which makes $c_\lambda \approx 0.1$ for the larger coil.

Analysis on the interactions of the key variables presented in this section yields the following underlying principles for optimisation, as summarized in [39]:

- The loop radii should be maximized, in order to maximize the coupling factor.

- For a given constraint on loop dimensions, there is an optimal frequency, which is approximately the point at which the radiation resistance begins to be significant compared to the skin-effect resistance.

- The wire radius and the number of coil turns should be as large as possible (bearing in mind that the coils should remain electrically small, to limit the electric field and hence radiation).

- In the case where the loops are not of equal size, the maximum operating frequency will be mainly determined by the larger of the two coils; this also dictates the lowest self-resonance frequency.

6.3 Coil System Design and Characterization

The initial application of this work is to charge wirelessly sensors in an aquatic environment. The system should be capable of transmitting tens to hundreds of watts from and unmanned surface vehicle (USV) to a sensor node placed on a buoy at a distance of tens of centimetres. Matlab simulations, based on the expressions presented in Section 6.2, were undertaken to provide a clear understanding of the efficiency that could be reached for such a system. Furthermore, full-wave 3D electromagnetic simulations were used to compare simulation results with measurements.

6.3.1 Link Simulations

Fig. 6.2 shows the efficiency versus frequency for different loop diameters with identical transmit and receive circular cross-section copper coils. The existence of an optimal frequency and the dependence of the efficiency on coil dimensions can be clearly seen. The shape of the efficiency curves varies between coil sizes, mainly for the larger coils, due to the fast approximation to the 100% efficiency limit. Smaller coils that do not achieve 100% will all have the same efficiency curve shape as that of the 10 cm diameter coils.
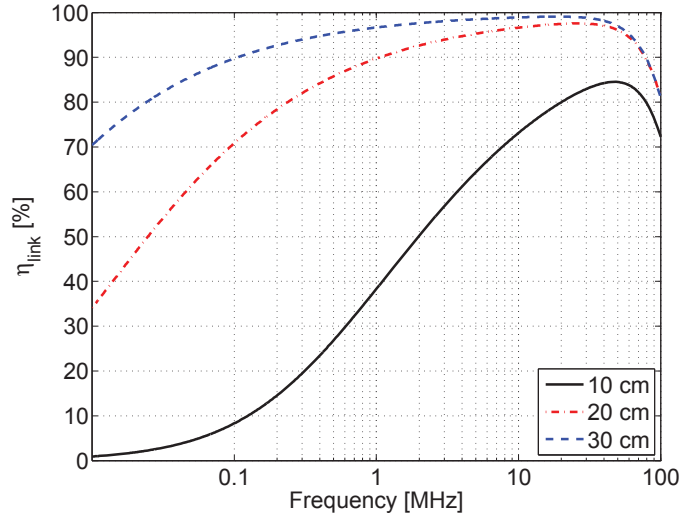
Figure 6.2: Link efficiency variation across frequency for 3 turn coils with different coil diameters at $D = 30$ cm and a wire diameter $a = 1$ cm.

To investigate how efficiency varies with different air-gaps, the link efficiency

against distance of several coil sizes is plotted. Fig. 6.3 illustrates that the efficiency drops rapidly with distance and provides a clear indication of the air-gap over which this technology can be effectively employed, for coil diameters in the low 10s of cm. These data prompts the use of a maximum air-gap between 30 and 60 cm for link efficiencies over 90% for coils < 30 cm diameter.
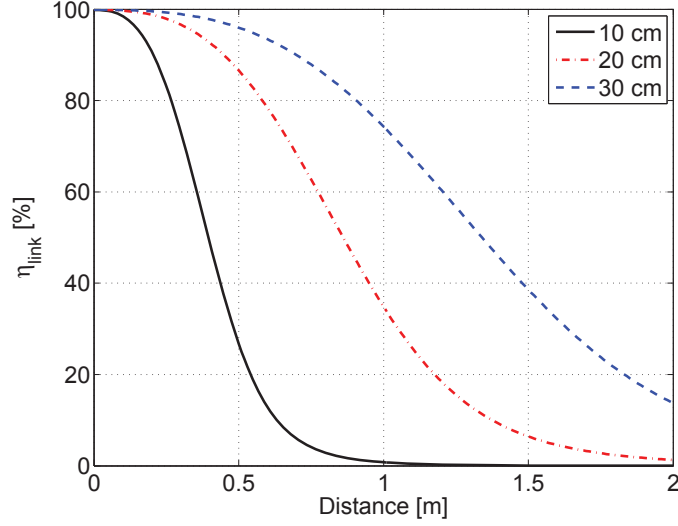
Figure 6.3: Link efficiency variation across different air-gaps for 3 turn coils with different diameters, an operating frequency $f_o = 6$ MHz and a wire diameter $a = 1$ cm.

Once the operating distance is defined, a set of simulations has to be performed to account for the intrinsic size limitations of the USV and the sensor node. Several coil size combinations are simulated and are presented in Fig. 6.4. This figure shows how the optimal frequency is determined mainly by the electrical size needed to maximise the unloaded Q of the largest coil. When the receiver coil size is constrained, this figure shows that the link efficiency can still be improved by increasing the primary coil diameter and tuning the operating frequency. In addition, the link gain can be increased to compensate for the RX size constraints, as presented in Section 6.2.

Given the fact that the TX would be placed on an unmanned aquatic vehicle (robotic kayak) and the RX on top of a buoy, the selected sizes for the water monitoring application are 30 cm and 20 cm for transmit and receive coils, respectively. With these sizes, link efficiencies above 90% are expected above 3 MHz.
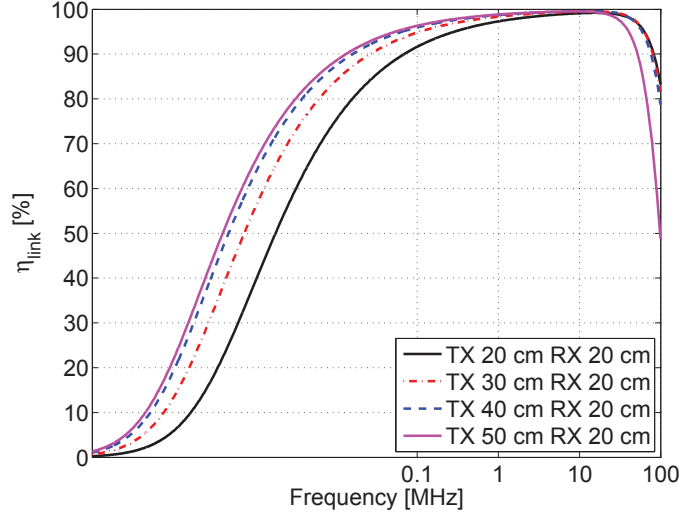
Figure 6.4: Link efficiency variation across frequency for different TX diameters with a fixed RX size. The TX coils have 3 turns and the receiver 5 turns. The air-gap is 30 cm and the wire diameter is $a = 1$ cm.

6.3.2 Coil Fabrication and Measurements

Q measurements are required for the TX and RX coils, to prove that the required Q-factors for achieving link efficiencies above 90% can be achieved, and that the models used during simulations provide results close to reality. Also, a proof-of-concept coil design is needed to see if a cost-effective solution for building coils from copper piping can yield high quality factors, alleviating the need for expensive Litz wire fabrication. For electromagnetic design reasons, the distance D from the centre-to-centre of the coils is used. However, it is important to note that the minimum distance between coils is $(D-7)$ cm throughout this work. As mentioned previously, a different sized TX and RX coil is used in the setup; this is thought to be more realistic for other applications. The coils are made from copper piping having a 1 cm diameter and 1 mm wall thickness. The wall thickness is selected based on material price and on $\delta = 38$ μm (6.16), for copper at 3 MHz, the lowest intended operating frequency.

Q-factor measurement techniques have been described in the open literature for more than fifty years. These techniques have been evolving due to the advancement of measurement equipment and its capabilities of working at higher frequencies. The measurement of inductor Q-factors has always been a challenging task, since

inductors are usually considered the weak links in resonating systems. One of the most famous methods of measuring Q-factors was with a Q-meter, where a known variable capacitor on a series RLC circuit was used to resonate with the inductor under test. When resonance was met, the voltages of the two reactances were equal. Since the current value was known, given that both the resistor and generator voltage were known, then the voltage on either reactance was known. This generated the following equation to calculate unloaded Q: [170].

$$V_C = \frac{V_{gen}X_L}{R} = \frac{V_{gen}X_C}{R} = V_{gen}Q \qquad (6.29)$$

where X_L and X_C are the inductor and capacitor reactances, respectively, V_{gen} is the voltage of the generator, R is the series resistance and V_C is the measured voltage on the variable capacitor. Using this equation one can clearly see that if V_{gen} is 1 V the Q-factor could be read directly from the meter.

With the advancement of communications, industry needed a tool to perform fast and effective methods to characterize the parameters of a network over a large range of frequencies. The vector network analyser (VNA) solved these needs and provided a new way of doing impedance measurements at very high frequencies, currently up to 1 THz, making the Q-meter obsolete. Two different approaches to measure the Q-factor can be performed with a VNA. One is using the voltage wave reflection coefficient [171], *i.e.* comparing the amplitude of the reflected wave to the incident wave. The other method uses the voltage wave transmission coefficient [172], *i.e.* comparing the amplitude of the transmitted wave to the incident wave.

To measure the Q-factor through insertion loss or transmission coefficient measurements, two loosely inductive coupled coils are used as measuring probes, as shown in Fig. 6.5. To avoid carrying the insertion loss error, as described by Kajfez *et al.* in [172], two conditions are required:

- The return loss of both measuring probes has to be the same, ensuring that the coupling coefficient from the probes to the coil is the same.

- The coupling between the probes and the coil needs to be very small, *i.e.* the

coupling has to be small enough so that the insertion loss at the resonant frequency will be far away from unity. This will ensure that the measuring probes will not be absorbing energy.
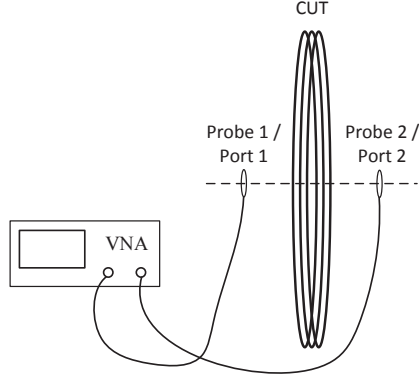
Figure 6.5: Q-factor from insertion loss measurements using two loosely coupled coils as probes.

The relationship between the transmission coefficient and the coupling factors between the probes connected to each port of the VNA (k_1 and k_2) and the coil under test (CUT) at a specific frequency (f_o) is defined by [172]:

$$|S_{21}(f_o)| = \frac{\sqrt{4k_1 k_2}}{1 + k_1 + k_2} \tag{6.30}$$

When both coupling factors are equal by ensuring that the mechanical tolerances of the test setup are the same for both probes:

$$k = 2k_2 \tag{6.31}$$

$$k = \frac{|S_{21}(fo)|}{1 - |S_{21}(fo)|} \tag{6.32}$$

New VNAs, such as the Agilent E5061A, used to conduct Q measurements, have the ability to calculate the loaded Q-factor automatically using a 3 dB bandwidth. Since the 3 dB Q measurements provided by the VNA are loaded, the unloaded Q-factor (Q_0) can be calculated with $Q_0 = Q_L(1 + k)$, where Q_L is the loaded Q.

Substituting the latter expression in (6.32) gives:

$$Q_0 = \frac{Q_L}{1 - |S_{21}(fo)|} \tag{6.33}$$

To meet the previous two conditions and minimise measurement errors, the mechanical tolerances of the test set up need to be the same for both probes. This ensures that both return loss coefficients are the same. In addition, all readings are taken with an $S_{21} \leq -10$ dB to ensure a low coupling and comply with the second condition.

A re-configurable test fixture was fabricated to hold the coils and allow for reproducible and easily adjustable operating scenarios, as will be described in the following sections. Perspex was used for both the stands and the coil spacers, to avoid the generation of eddy currents that could result in measurement errors. The coil spacers helped to maintain a fixed distance of 2 cm between windings, measured from the centres of the pipe, to reduce the proximity effect between turns.

Additionally, coaxial cables with the same length and with standard 50 Ω impedance were used. To connect to both coils, the inductive coupling probes consisted of single turn loops, with an area at least 300 times smaller than the coil under test. They were designed on single layer reinforced epoxy FR4 substrate with 50 Ω end-launch SMA connectors. To ensure that both probes, with their respective cables, had the same return loss, one-port measurements were conducted. Furthermore, it was necessary to ensure the same coupling factor from each probe to the coil under test (CUT). To achieve this, the probes were held by plastic stands placed at the same distance from both the VNA and the CUT. Additionally, the setup was placed on a wooden table far away from any metallic object. Figures 6.6, 6.7 and 6.8 show the test fixture for measuring the coil Q-factor, coupling factor and inductive power transfer at different separation distances, transverse offsets and angular misalignments between both coils.

Based on the simulated efficiency figures from Section 6.3.1, Q-factor measurements were performed for the 3 turn, 30 cm diameter coil and the 5 turn, 20 cm

Figure 6.6: IPT Perspex adjustable test fixture.
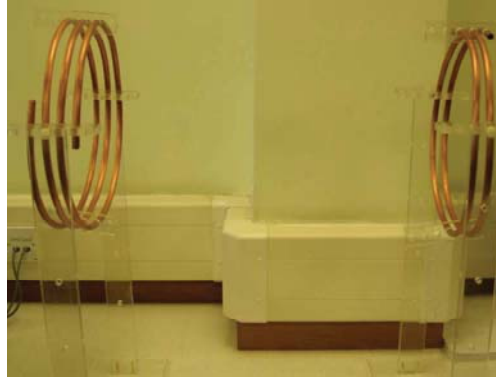
Figure 6.7: IPT Perspex adjustable test fixture.

coil. An array of high Q capacitors were used in parallel with the coil, to tune the operating frequency and conduct measurements at different frequencies [39]. Dielectric Lab C40AH series [173] capacitors were selected, due to their low effective series resistance $ESR \leq 18m\Omega$, high voltage capacity $V_{cap} = 7200$ V and high self-resonant frequency $SRF \geq 210$MHz. The lowest Q of the capacitors is $Q_{cap} \geq 10000$ at 10 MHz for 100 pF. With the Q of the capacitors provided by the manufacturer, the unloaded Q of the coil is calculated using (6.33) and the total measured loaded Q_T, shown in [39]:

$$Q_T = \frac{Q_L Q_{cap}}{Q_L + Q_{cap}} \tag{6.34}$$

As shown in Figures 6.9 and 6.10, full 3D electromagnetic simulations were performed and compared to measurements and simulations based on the expressions presented in Section 6.2.3. Figures 6.11 and 6.12 show these results. The mismatch
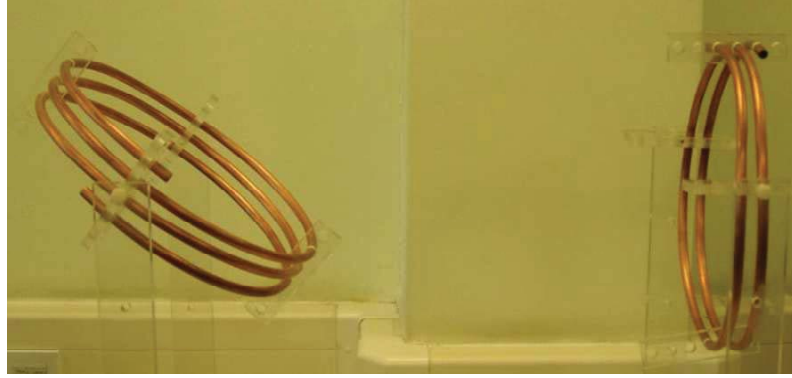
Figure 6.8: IPT Perspex adjustable test fixture [39].

between measurements and simulated results is mainly due to the fact that, even though rigorous procedures were taken to ensure that both probe coupling factors remained as equal as possible, it is likely that the mechanical characteristics of the cables, *e.g.* the sagging of the cables between the output ports of the vector network analyser and the probes, may be enough to increase the measurement error [174].
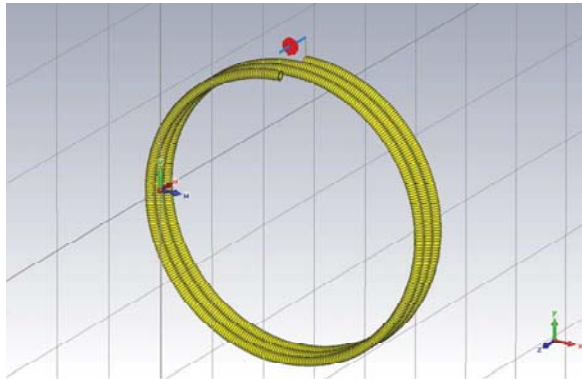
Figure 6.9: Drawn 3D model of the 3 turn 30 cm diameter TX coil

Additional curve fitting was undertaken to account for the variations of the capacitor's Q-factor with frequency. This was done by using the manufacturer's data sheet and creating 18 order polynomials. Scattering parameter tables and Q vs. frequency tables provided by the manufacturers were used to extrapolate Q values for the frequencies that are measured. Nevertheless, it is important to note that on the final design, where a fixed frequency is used, fewer capacitors are required, thus making the Q-factor of the resonant circuit higher. These simulations demonstrate that the transmission type measurement can be accurate for frequencies that are lower than
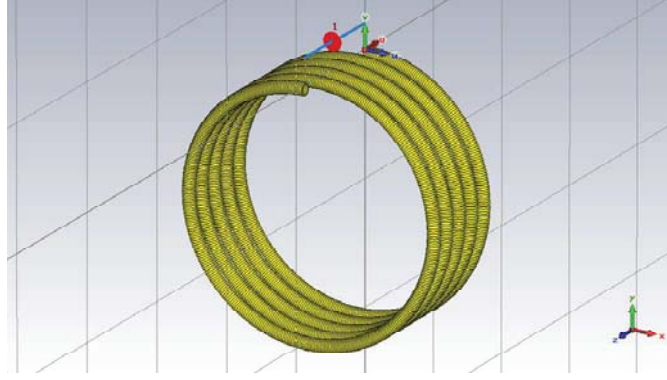
Figure 6.10: Drawn 3D model of the 5 turn 20 cm diameter RX coil
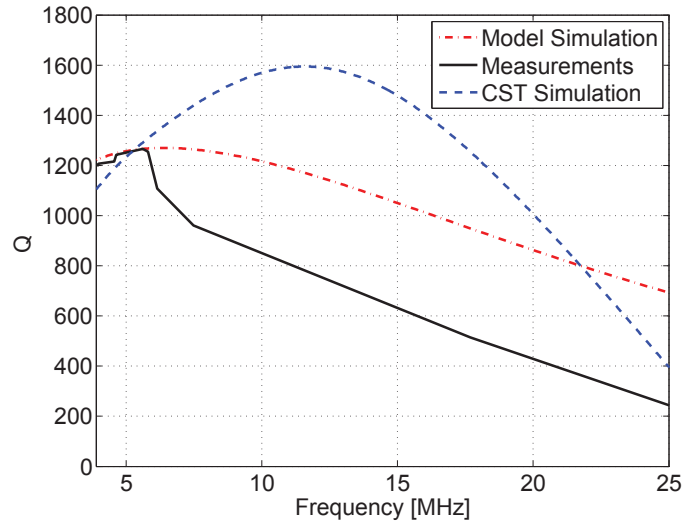
Figure 6.11: Q-factor simulation and measurement results for a 3 turn 30 cm diameter coil.

30% of the SRF of the CUT, which is 26.8 MHz and 29.2 MHz for the transmitter and the receiver, respectively. This is due to the fact that the parasitic capacitance reactance is negligible, far away from the SRF, where the inductor's reactance dominates, but its effect becomes noticeable as the measurement frequency gets closer to the SRF. Furthermore, these results show that, a combination of simplified unloaded Q models and full 3D electromagnetic simulations can only give approximate answers and carefull consideration of excitiations and mesh conditions needs to be taken into account to increase the accuracy of the simulations, as demonstrated in [175].

The highest Q for both TX and RX coils is found close to 6 MHz, where skin depth is only 27 μm. The maximum unloaded Q value for the 5-turn, 20 cm diameter RX
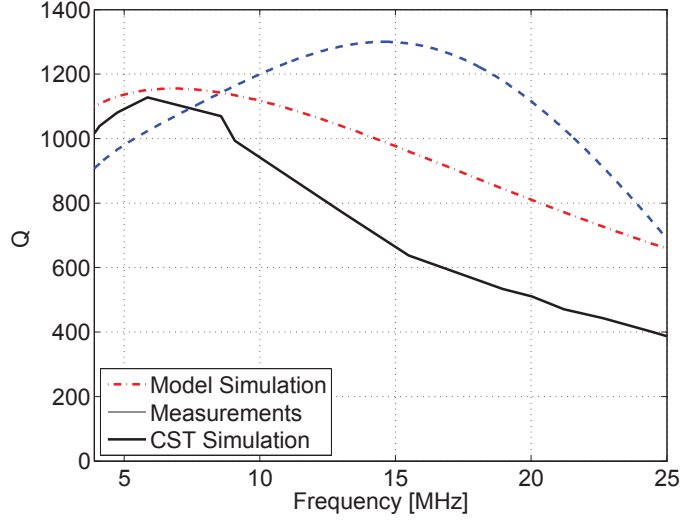
Figure 6.12: Q-factor simulation and measurement results for a 5 turn 20 cm diameter coil

coil is $Q_{RX} = 1,100$ and $Q_{TX} = 1,270$ for the 3-turn, 30 cm TX coil.

With the coil Q-factors measured, the only variable missing to calculate the link efficiency is the coupling factor. Using the test fixture previously described, coupling factor measurements were undertaken to characterize the coil coupling in an array of different scenarios [40]. Measurements were undertaken with different separation distances or against transverse coil offsets h, as illustrated in Fig. 6.13, or transmitter or receiver coil angular misalignment, θ_{TX} or θ_{RX}, respectively, as illustrated in Fig. 6.14. For experiments involving transverse offset or angular misalignment, the centre-to-centre distance was fixed at $D = 30$ cm (the minimum distance between coils is 23 cm). Data from these measurements was also used to predict the operating characteristics, as well as the expected efficiency of the IPT system.

The k measurements and calculations were performed with a well-known voltage transfer technique, as described in detail in [41]. In this k measurement technique, the coil terminals are connected to oscilloscope probes and a sinusoid signal from a TTI TGA12104 signal generator, at the operating frequency f_o, is passed through the TX coil and the voltage on both coils is recorded to obtain the voltage gain A_{TX}.

$$A_{TX} = \frac{v_{RX}}{v_{TX}} = kn \tag{6.35}$$
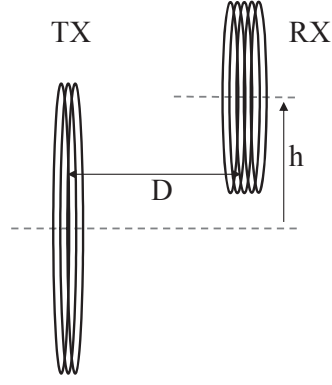
Figure 6.13: Experimental set-up for distance and transverse offset measurements.
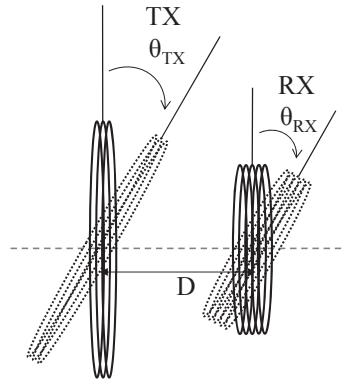
Figure 6.14: Experimental set-up for angular misalignment measurements.

where n is the link's or transformer's ratio. The RX gain A_{RX} is then measured the same way to obtain:

$$A_{RX} = \frac{v_{TX}}{v_{RX}} = \frac{k}{n} \tag{6.36}$$

which gives:

$$k = \sqrt{A_{TX} A_{RX}} \tag{6.37}$$

Figs. 6.15 and 6.16 show the coupling factor and link efficiency, calculated from the previous Q-factor measurements, for different distance and transverse offset measurements. Configurations which give rise to the same coupling coefficient are expected to achieve the same efficiency, *i.e.* perfectly aligned at a separation of $D = 40\ cm$

should achieve the same efficiency as an offset of $h = 21 \ cm$ at $D = 30 \ cm$.
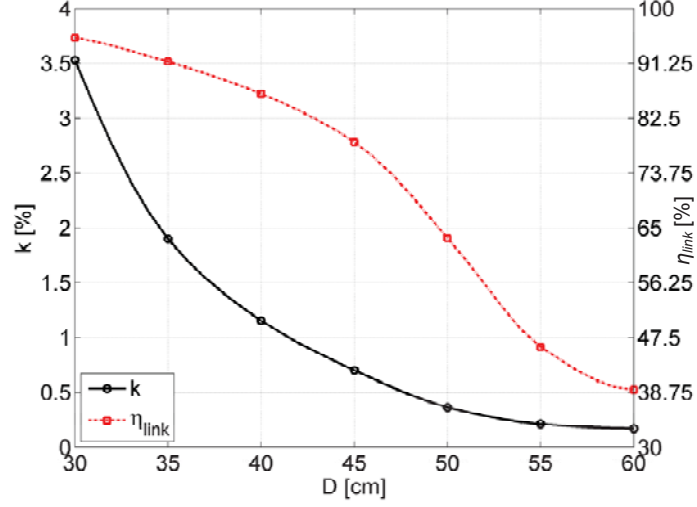
Figure 6.15: Measurements of coupling factor against coil separation distance in air, with perfectly aligned coils [40].
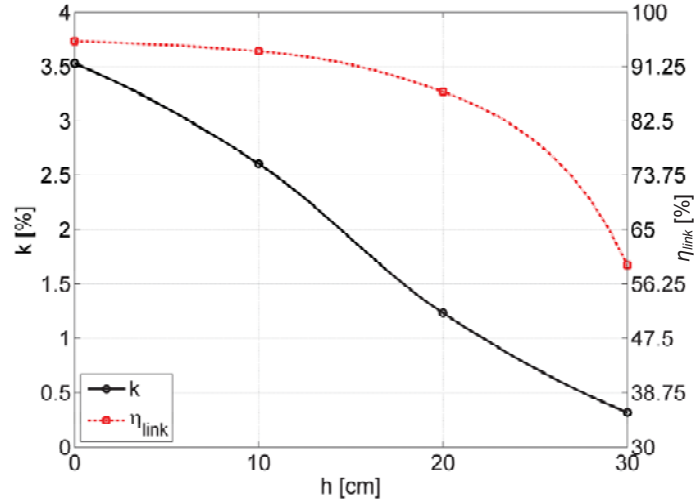
Figure 6.16: Measurements of coupling factor against coil transverse offset in air, at a distance of 30 cm [40].

Figs. 6.17 and 6.18 show k measurement results for TX and RX angular misalignment, respectively. In Fig. 6.17, while the TX coil angle increases, the distance between both coils reduces enough to compensate for angular misalignment. With the RX coil angle variation, a trough is seen at $\theta_{RX} = 75°$; this is the point at which the distance between the coils is not enough to compensate for the angular misalignment.

These conclusions will be supported in Section 7.3, where a clear correlation be-
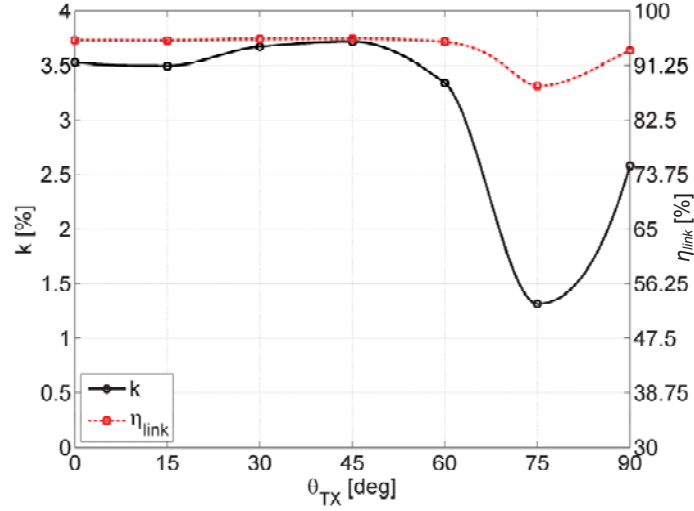
Figure 6.17: Measurements of coupling factor against transmitter coil angular misalignment, at a distance of 30 cm [40].

tween the coupling factor measurements and dc-to-load efficiency will be demonstrated.

6.4 Conclusion

The results and the measurement techniques given in this chapter provide an initial design framework that is used throughout the driver design, to achieve efficient inductive links for wireless power transfer. In addition, coil and test fixture fabrication procedures were conducted to achieve low cost, light weight and reproducible designs and results. It is important to emphasize how, by approaching the IPT system design with an overall view, not only the optimization of the link but the optimization of all the building blocks of the system can be achieved.

The analytic expressions that were presented highlighted the critical variables that are needed for an overall system optimization. It was shown how the specific application characteristics define the geometry of the IPT link, and it is around these constraints that the design of the coils is carried out to operate at the highest Q, thus helping to compensate for low coupling.

In order to achieve a light weight system, copper pipe was selected as an ideal candidate to achieve high unloaded Q-factors. Simulations based on analytical models
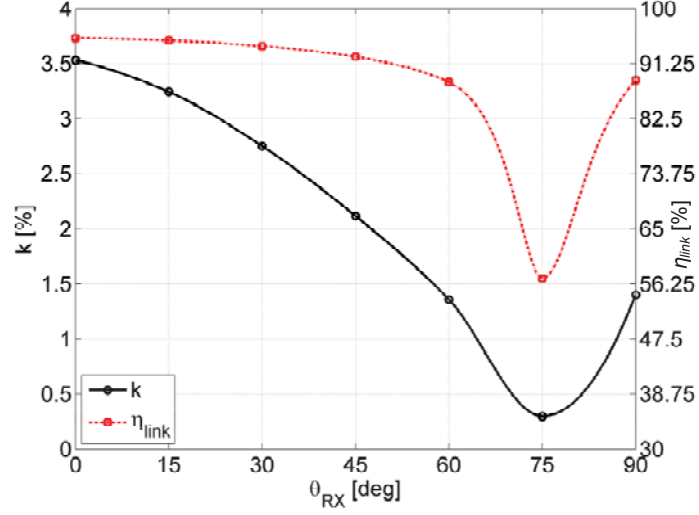
Figure 6.18: Measurements of coupling factor against receiver coil angular misalignment, at a distance of 30 cm [40].

were performed and a 3 turn, 30 cm diameter TX coil and a 5 turn, 20 cm RX coil were chosen as optimal coils for this application. Q-factor measurements and full 3D electromagnetic simulations showed Q-factor values above 1,000, proving that copper pipe coils are a extremely good alternative to expensive Litz-wire assemblies.

In addition, coupling factor measurements were performed to characterize the link in various misalignment conditions to prove that high system efficiencies can be achieved without expensive and heavy field-shaping techniques. Results from simulations and measurements were used to define the driver specifications, which will be presented in the following chapter. With all the key IPT system parameters analysed and measured, the challenge now lies in designing an efficient amplifier that can drive the coils at the optimal frequency and at the desired power levels.

7 Coil Driver Design

7.1 Introduction

Based on the previous coupling factor analysis and measurements of the coils' characteristics at high frequencies, a high power, high frequency driver is required to achieve link efficiencies above 90%. In a typical IPT system, this is achieved by driving the coils with a 50 Ω loop that is impedance matched to a high frequency COTS RF transmitter having an output power amplifier. In this typical RF scenario, the maximum power transfer is achieved, but not the desired maximum efficiency. The number of stages can be reduced if the 50 Ω impedance is avoided, by integrating the power amplifier and impedance matching circuits into one driver sub-system. This can be achieved by carefully designing an efficienct power amplifier capable of high frequency operation.

Previously, it was shown how the optimal operating frequency was in the low MHz region. Fig. 6.4 showed how with 30 cm and 20 cm coils, at a distance of 30 cm, efficiencies above 90% can be achieved with operating frequencies above 1 MHz. Furthermore, simulations and measurements shown in Section 6.3.2 prove that unloaded Q-factors above 1000, from the selected TX and RX coils, can be achieved at frequencies between 5 and 7 MHz.

The overall dc-to-load efficiency will be determined by the product of the link and amplifier efficiencies. For our application, the amplifier must be designed to handle 100 W at high frequencies. To carry out this task, the trade-offs between topology, device type, size, current and voltage handling capability, power transfer capability, switching losses and frequency all have to be carefully considered. These considerations include the selection of components, such as the technology that will

be used for the switching. As an example, whilst it is desirable to use MOSFETs, due to their faster switching speed and hence lower switching losses, MOSFETs have lower voltage and current ratings than other power devices, such as IGBTs. Correct topology choice is vital in allowing smaller, faster devices to be used, to reduce switching times and hence enable operation at higher frequency.

In weakly coupled links, as with this work, the large leakage inductance of the transmitter demands high peak voltages and large currents needed to generate the magnetic fields. The parallel resonant tank of a Class-C amplifier avoids the large currents going through the switch, but the high voltages are still present. The Class-D avoids the high voltages going through the switch by having a series resonant tank that cancels the leakage inductance of the transmitter, but the large currents are still present. The dual resonant tanks of the Class-E amplifier make it an ideal combination of Class-C and Class-D amplifiers, since zero-voltage and zero-current switching can be achieved with the appropriate choice of components. This chapter presents an analysis of Class-E amplifier design for weakly coupled IPT systems and shows the design procedures that are required to achieve an efficient operation, based on the constraints defined by a specific application. An extensive framework for driver modelling, component selection and layout considerations to achieve a low loss, high frequency dc-rf conversion, capable of delivering more than 100 W at a distance of 30 cm, will be demonstrated. Finally, a full system characterization under different misalignment scenarios is discussed. Experimental results and a thorough versatility analysis demonstrate the high dc-to-load efficiency that an overall system optimization can achieve.

7.2 Driver Design and Fabrication

Class-E amplifiers have been designed and used extensively since Sokal and Sokal demonstrated the operational characteristics of their zero-switching power amplifier [176]. It is important to note that even though this power amplifier topology is widely known, designing high power amplifiers capable of working at 100 W and switching at a few MHz is a non-trivial task. This is mainly due to the high power

rating and fast switching capabilities that only a suitable power RF MOSFET can achieve, as well as the need to employ high Q capacitors. Silicon Carbide transistors were not considered due to longer rise and fall times, (four times more than an RF MOSFET). Furthermore, since an atypical non-50 Ω power amplifier is needed, to avoid additional impedance matching network components and their associated losses, the resonant Class-E topology needs to be modified to suit the coils' characteristics.

Fig. 7.1 shows a simplified schematic of a Class-E amplifier, where R_{ps} is the TX coil series resistance, R_{seq} is the effective RX resistance reflected onto the transmitter side, L_{TX} is the TX inductance and the switch S is isolated from the high TX coil voltages through C_{ser}, that works as a voltage divider, and from the high TX coil currents through C_{par}. By separating the primary coil from the active element, S, a coil voltage, V_{TX}, of 10 times the voltage supply, V_{DD}, is possible [41]. The choke inductor L_{choke} ensures that dc current is forced through C_{par}, charging it and thus increasing the offset of the damped sinusoidal voltage that comes from the resonant tank. It is with the right selection of the tank damping, the current passing through the choke and the switch voltage period that a zero voltage and a zero slope of the drain-to source-voltage can be accomplished at the time of switching, as shown in Fig. 7.2. When these conditions are kept, the reminding current from the sinusoid current, coming from the series tank and the dc current from the power supply, will go through the switch but no energy will be dissipated, since the C_{par} voltage is zero. It is important to note that the Class-E amplifier is a non-resonant amplifier, since the operating frequency lies between the resonance of the series tank and the parallel tank, thus leaving an inductive reactance in the series branch. With this amplifier design, smaller and faster MOSFETs can be used, resulting in highly efficient circuits. For example, in [177] 450 W is provided to a 50 Ω load with a Class-E amplifier operating at 3.3 MHz at an efficiency of 96%. Constraints in the trade-offs between maximum switch voltage, maximum switch current and device switching time do limit the efficiency, as the power levels increase due to the non-zero fall time of the current when the device is switched ON.
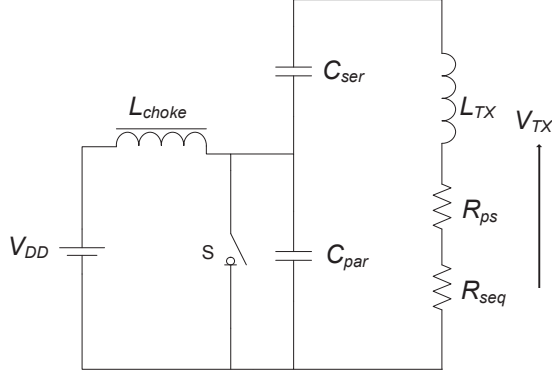
Figure 7.1: Class-E amplifier schematic.
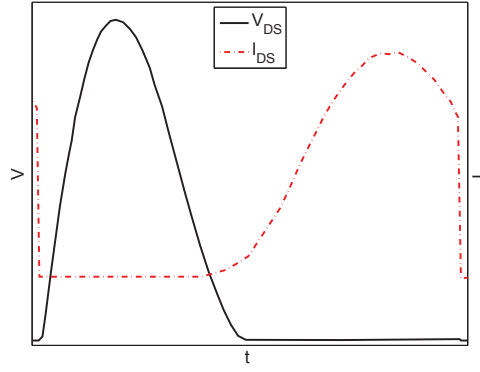
Figure 7.2: Class-E amplifier voltage and current waveforms.

With weakly coupled links and high Q coils, the amplifier is left with a very small load that does not drive the amplifier correctly. The solution to this problem is to increase the resistance of the amplifier, without increasing the inductance of the TX, thus avoiding higher circuit voltages. This can be accomplished by placing a capacitor in parallel with the coil, which absorbs the inductance of the transmitter and leaves an apparent resistance R_{app}, which is larger than the series resistance of the coil [41, 178]. This has the drawback that the amplifier would then require an extra inductance, typically added in series with the TX coil to increase the driver efficiency, as in [33].

This situation can be avoided by using a semi-resonant Class-E topology. Fig. 7.3 shows the circuit of a semi-resonant Class-E amplifier for the transmitter resonant tank, where the apparent load R_{app} (represented by R_{ps} and R_{seq}) and the apparent inductor L_{app} (represented by L_{TX} only, since the RX inductance is absorbed by the RX resonant capacitor), appear to be larger, thus helping to increase both driver

164
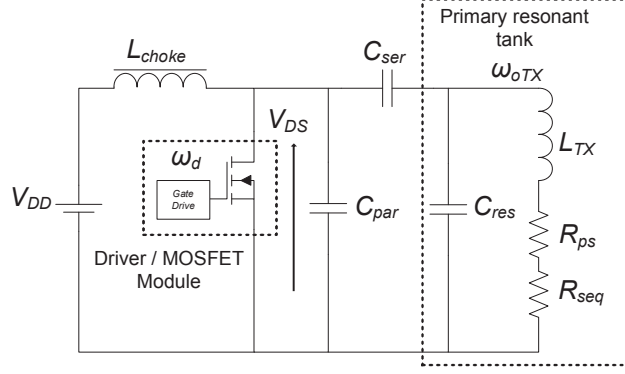
Figure 7.3: Semi-resonant Class-E topology, with $\omega_d < \omega_{oTX}$ [40].

and link efficiencies [40, 41]. This is achieved by tuning the primary resonant tank at a higher resonant frequency $\omega_{oTX} = (L_p C_{res})^{-\frac{1}{2}}$. This frequency is higher than the receiver's resonant tank driven resonant frequency $\omega_o = \omega_{oRX}$, at which the MOSFET gate driver switches at an operating frequency ω_d, where:

$$\omega_{oTX} > \omega_{oRX} \equiv \omega_d \tag{7.1}$$
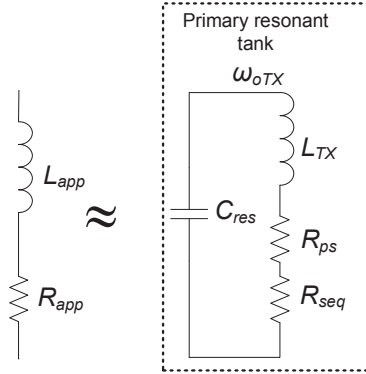
Figure 7.4: Apparent L_{app} and R_{app} of semi-resonant Class-E topology [41].

This semi-resonant operation avoids the losses associated with an extra inductor. As will be demonstrated in the following section, the use of semi-resonant operation allows for a simple but effective tuning mechanism; by modifying the frequency ratio ω_d/ω_{oTX}, the effective equivalent resistance and inductance of the primary tank can change for different operating scenarios.

7.3 Experimental Results

To fully characterize the practical IPT demonstrator system, shown in Fig. 7.5, a thorough experimental analysis was performed. The main goal of these experiments was to investigate its behaviour in different scenarios, by varying distance, transverse offset and angular misalignment; this allows a comparison against perfect alignment, to which the system was initially tuned (based on simulations). Furthermore, the results from these experiments were compared against results from frequency tuning the system for each different scenario.
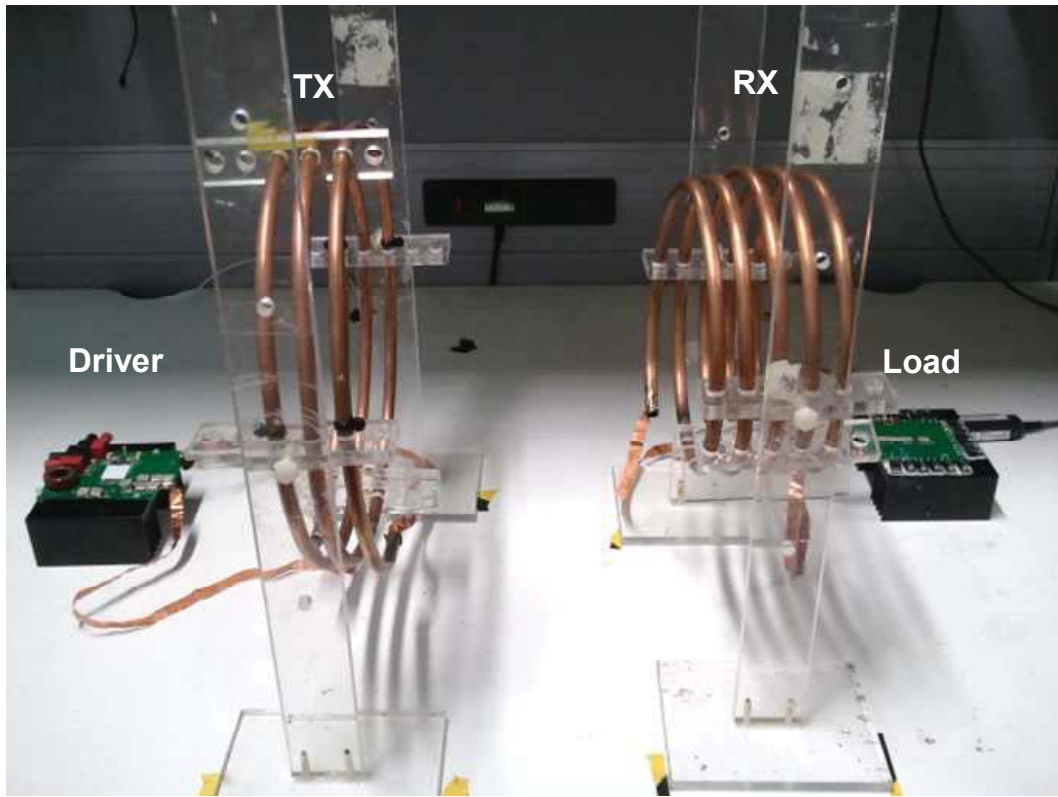
Figure 7.5: Perfectly aligned IPT test rig with $D = 30$ cm

.

In all experiments, the input voltage V_{DD} was kept constant at 60 V. This allowed sensible values of drain-source voltage to be obtained during operation, to which the output capacitance of the MOSFET is dependant, and helped to avoid replacing C_{par} in each experiment. A constant input dc power for all experiments could not be achieved. This is because, in several scenarios, driver operation was far away from Class-E operation, resulting in high losses during switching that could have

166

degraded or destroyed the driver/MOSFET module.

Due to the fact that the optimal load needs to be resistive, to avoid detuning the primary, a non-inductive resistor was used. Special considerations where taken to achieve the desired load with a resistive network, because a non-inductive resistor capable of handling more than 50 W is not commercially available. Metal film resistors where chosen, given their low inductance behaviour at high frequencies and capacity to handle a few watts (enough to withstand up to 100 W, once the load network was made). A major limitation for this type of resistor is that as its resistance and operating frequency increase the parasitic shunt capacitance also increases. In addition, as the resistor temperature increases its resistance varies. The parasitic capacitance for these resistors was calculated to be 2.8 pF at 6 MHz. This was taken into account when designing the load network and also the selection of the receiver's tuning capacitor. The total capacitance from the load resistor was absorbed by the calculated tuning capacitance, to ensure receiver resonance, thus avoiding the reflection of capacitive reactance to the transmitter side.

The dc-to-load efficiency of the system was initially measured using Agilent N2783A current probes, but, after several measurements, it was noted that the results were not reflecting the true operation of the circuit. Also, the current probes are not capable of measuring current accurately in the presence of significant electromagnetic noise [179]. The voltage across the load could not be measured with the oscilloscope probe, because the probe's capacitance is 15 pF; enough to detune the receiver coil from resonance. For these reasons, and the fact that the resistor's precise temperature dependence is unknown, an indirect method of measuring the dc-to-load efficiency was implemented [40]. Power was inferred from accurate steady-state heat-sink temperature measurements, since both the driver and the load (including the tuning capacitors) were placed over separated, isolated and over-specified heat sinks without forced-air cooling. The input dc power was also measured accurately and used together with the RX thermal measurements to calculate the dc-to-load efficiency using the following:

$$\eta_{dc\text{-}load} = \frac{T_{ssRX} - T_{amb}}{R_{thRX}(T)P_{dc}} \qquad (7.2)$$

where T_{amb} is the ambient temperature, T_{ssRX} is the heat sink steady-state temperature of the receiving coils and $R_{thRX}(T)$ is the lumped thermal resistance of the RX load. The temperature measurements were calibrated by applying a known dc power to the RX load until all temperatures reached steady state. Measurements under the same thermal experimental conditions, as when the IPT system was tested, were performed. Due to the RX load spatial distribution over the heat sink and the fact that the heat sink was positioned with the fins facing downwards on the bench, with a 333 K temperature gradient $R_{thRX} = 208$ K/W compared well to the manufacturers 203 K/W. Furthermore, by characterizing the load arrangement, the non-linear behaviour of the heat sink was accounted for, which can be as high as 25% to 50% of the dissipated heat, according to [180].

It is important to note that this is a conservative dc-to-load efficiency calculation, since T_{amb} will increase as T_{ssRX} increases; giving a lower $\eta_{dc\text{-}load}$ when compared to the scenario, where T_{amb} could be kept constant until the steady state of the system is reached. Even more important is the fact that as the temperature of the resistors increases the value of the load resistance will start to drift away from its optimal value; drifting away from maximum efficiency.

7.3.1 Tuning Procedure

To achieve a semi-resonant Class-E operation, similar to that observed by simulations, an iterative tuning process had to be performed. This establishes the appropriate values for the driver and the coil capacitors (taking into account their fabrication tolerances) and the coil Q variations (due to proximity of metallic objects, such as bench supports, during experiments).

First, the receiver resonator's capacitor had to be decreased, to account for the load resistor's equivalent shunt capacitance for correct receiver resonance. With an untuned receiver, the value of the transmitter resonator's capacitor would need to change, to account for the reflected reactance from the receiver onto the transmitter

and ensure that semi-resonance operation is still present. This changes the ratio of ω_d/ω_{oTX}, which creates the need for retuning C_{par} and C_{ser}. The major limitation of this scenario is that if the ratio ω_d/ω_{oTX} starts to increase, there is a point at which the required C_{par} needed to tune the driver is lower than the output capacitance C_{oss} of the MOSFET, which makes the MOSFET unsuitable for Class-E operation.

Once receiver resonance is obtained, a similar procedure can be followed to achieve zero switching operation, as described in [155]. Since C_{par} is implemented by an external physical capacitor and C_{oss}, which is dependant on V_{DS}, extra iterations are needed to achieve good operation. As seen from simulations, V_{DS} is a very useful guide to Class-E operation, therefore tuning the peak-to-peak voltage is as important as achieving zero-voltage, zero-current switching to increase the efficiency [181]. Based on empirical results from [176], if $V_{DS} > 3.56\ V_{DD}$, C_{par} needs to be increased in steps of 5 pF and if $V_{DS} < 3.56\ V_{DD}$, it should be decreased by the same amount until the correct V_{DS} is achieved. While doing this, C_{ser} may need a slight adjustment to bring back the driver to zero switching.

The component values can be tuned using Fig. 7.6, similar to the one presented in [155], as a reference. The main difference from tuning a semi-resonant Class-E amplifier for IPT, to a conventional Class-E amplifier, is that the inductor and the load resistor cannot be modified to tune the amplifier, because they are already predetermined by the TX coil and the optimal load. As can be seen, if V_{DS} is not zero, C_{ser} needs to be increased slightly and then adjust C_{par} to achieve a soft landing.

Since the load resistance value varies with temperature, several iterations were performed by increasing or decreasing the load resistance by $\pm 5\%$, until a maximum efficiency of 66% was achieved. For each iteration, receiver resonance was achieved and tuning of C_{par} and C_{ser} was performed, as previously described. Fig. 7.7 shows the drain-source voltage (simulated and measured) for the tuned IPT system, for an aligned set of coils at a separation distance of 30 cm; the total input dc power was 90 W.

Whilst the waveform generated from simulations has a smooth landing, a negative
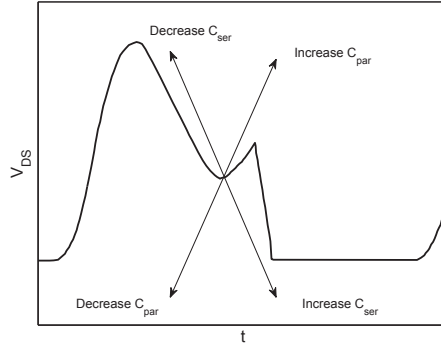
Figure 7.6: Class-E passive component tuning procedure based on drain-to-source voltage, V_{DS}
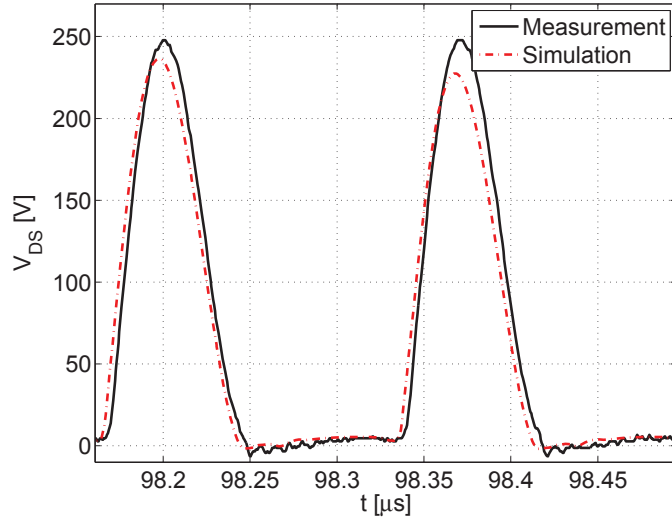
Figure 7.7: Drain to source voltage against time for the IPT system with a 30 cm separation distance and $P_{dc} = 90\ W$

.

ripple of less than 10 V can be seen when the MOSFET is ON. This negative ripple is generated by a small voltage still present at the drain, when the MOSFET is turned ON, due to a higher than expected loaded Q for the transmitter resonant circuit. This was the best possible switching achieved with the discrete capacitors available. The higher measured V_{DS} results could be decreased by adding more capacitance to C_{par}, but this change was not reflected in a measurable efficiency improvement. Therefore, to decrease the losses in the capacitor (due to ESR), no extra parallel capacitor was added and V_{DS} was left higher than expected in the simulation.

7.3.2 System Versatility Analysis

Once the IPT system was optimally tuned to achieve a high efficiency, while being perfectly aligned, measurements with different separation distances were performed to observe the operating capabilities without performing extra tuning. As can be seen in Fig. 7.8, the distance between the coils was varied between 30 and 60 cm. As D increases the efficiency decreases as the coupling factor decreases, detuning the driver and creating the need for different C_{par} and C_{ser} values to re-establish zero switching operation.

An easier tuning alternative is to change the operating frequency of the clock, thus relying on the semi-resonant operation of the driver. When this is performed, the receiver is no longer in resonance and the transmitter sees a reflected reactance. This extra reactance, in addition to the transmitter's reactance, is enough to improve the tuning of the semi-resonant Class-E driver, modifying ω_d/ω_{oTX} and shifting the driver's waveforms closer to zero-switching operation. As seen in Fig. 7.9, as the clock frequency is altered for each different measurement, the efficiency increased considerably over the untuned operation. The dc-to-load efficiency from the clock-frequency tuned version at a 50 cm separation distance was 25%, compared to 20%, as seen in Fig. 7.8. It is important to note that to achieve this increase in efficiency, a clock frequency change of less than 1% is required.

To analyse the efficiency of the IPT system, for a set of scenarios with different offsets, as shown in Fig. 6.13, measurements for both the perfectly aligned 30 cm impedance tuning with fixed clock frequency case and with clock frequency tuning were performed. Fig. 7.10 shows the results for IPT with different coil offsets. In this case, dc-to-load efficiency decreases; following a similar trend as the corresponding k measurements from Section 6.3. It can be seen that even with an offset of 10 cm, and no additional tuning, the IPT system performs with a dc-to-load efficiency above 58%.

With clock frequency tuning, as shown in Fig. 7.11, the dc-to-load efficiency is above 50%, with $h < 14\ cm$, and an efficiency increase of 5% is achieved with an offset of 20 cm. Although higher dc-to-load efficiencies could be achieved with tuning

Figure 7.8: Measurement of the dc-to-load efficiency against separation distance with fixed clock frequency and load resistance tuning to aligned 30 cm separation distance scenario.
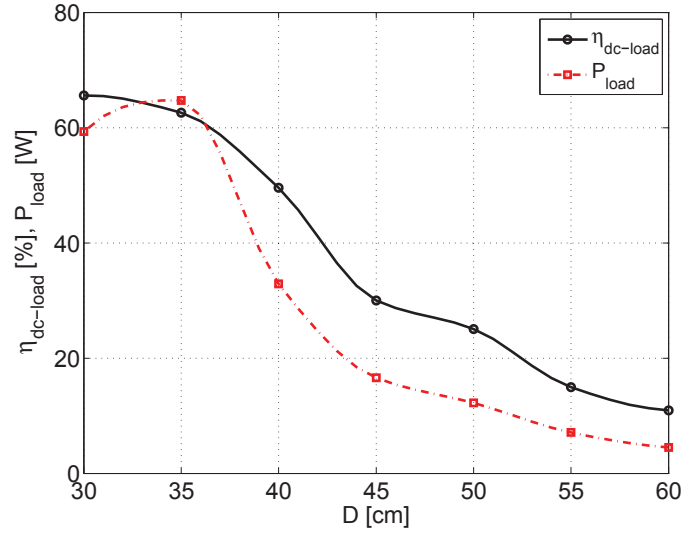
Figure 7.9: Measurement of the dc-to-load efficiency against separation distance with clock frequency tuning

.
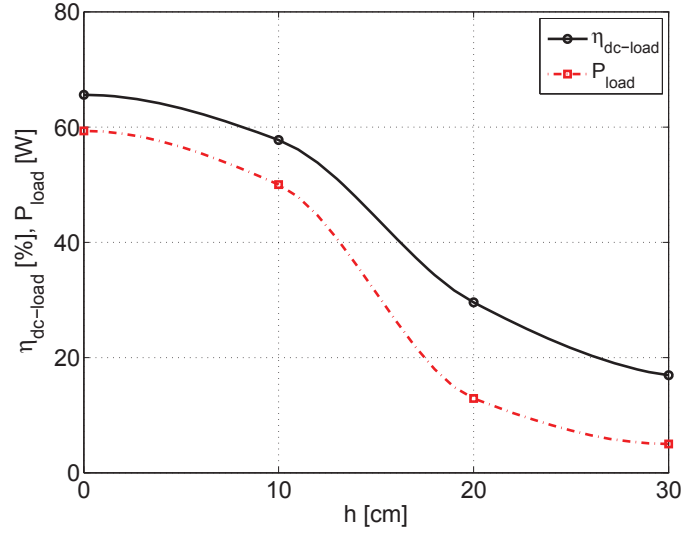
Figure 7.10: Measurement of the dc-to-load efficiency against coil transverse offset with fixed clock frequency and load resistance tuning to aligned 30 cm separation distance scenario.

the optimal load for each offset, the results presented in this figure demonstrates that efficiences above 50% can be achieved even at highly misaligned scenarios without the need for load tuning or complex and heavy coupling factor enhancement techniques.
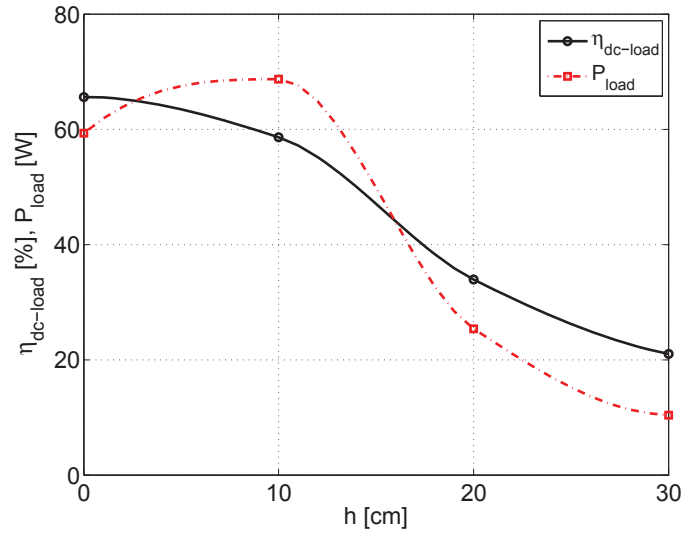
Figure 7.11: Measurement of the dc-to-load efficiency against coil transverse offset with only clock frequency tuning.

To characterise how the system operates, while varying coil misalignment angle θ, in both transmitter and receiver, measurements at a fixed distance of $D = 30\ cm$ were performed, as shown in Fig. 6.14. From Figs. 7.12 and 7.13, measurements for

a varying TX coil angle θ_{TX} were performed. As predicted, by the coupling factor measurements, a constant high efficiency is achieved for angles below $75°$, when clock frequency tuning is performed. In contrast, a decrease in efficiency, not clearly linked with k is seen with the fixed clock frequency scenario. This is due to the fact that with the fixed clock frequency and load resistance tuning case, the presence of a larger reflecting load from the receiver influenced efficiency more than with the relatively large and constant coupling factor in the tuning of the IPT system. With the clock frequency tuning scenario, the frequency variation is enough to tune the Class-E and exploit the benefit of almost constant k. DC-to-load efficiencies above 60% are achieved for almost all $\theta_{TX} < 72°$, with clock frequency tuning, showing the robust capabilities of the system to perform in a wide range of transmission angles with a fractional frequency variation of less than 6%.
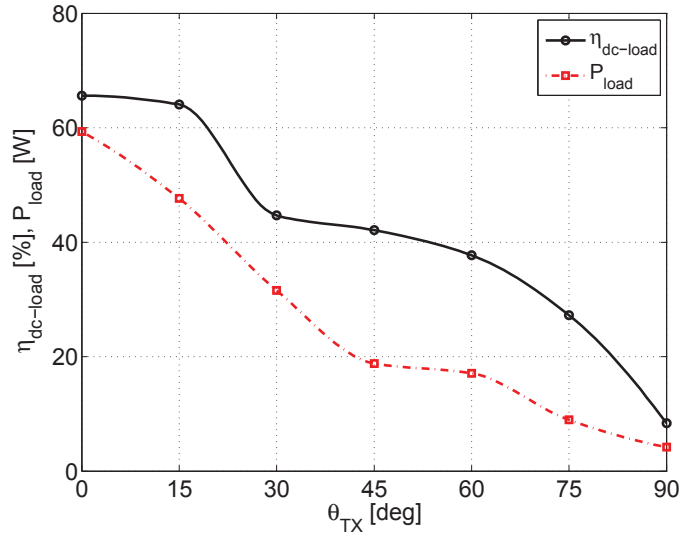
Figure 7.12: Measurement of the dc-to-load efficiency against TX coil angle with fixed clock frequency and load resistance tuning to aligned 30 cm separation distance scenario.

Finally, measurements with a varying θ_{RX} were performed, as shown in Fig. 7.14. The efficiency is almost constant and above 50% up to $\theta_{RX} = 52°$. Above this angle, the efficiency decreases dramatically, as predicted by the coupling factor measurements. A noticeable difference is appreciated in Fig. 7.15, with $\theta_{RX} = 45°$, where the dc-to-load efficiency is 56% in the clock frequency tuned case and only 40% in the fixed clock frequency impedance tuned version.
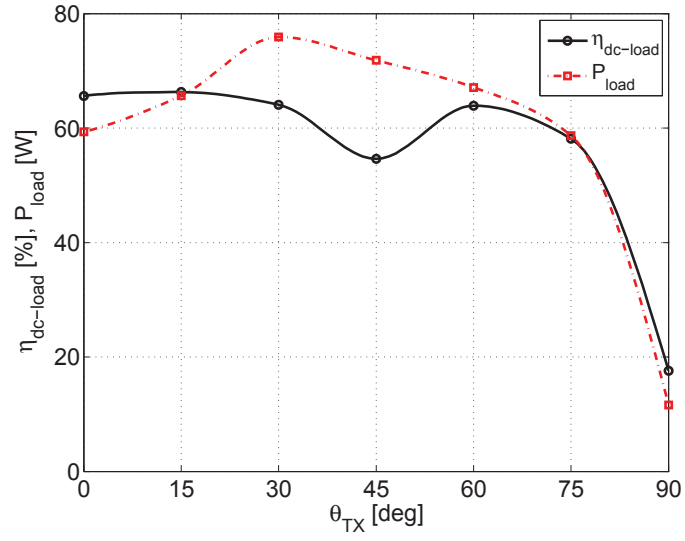
Figure 7.13: Measurement of the dc-to-load efficiency against TX coil angular mis-alignment with clock frequency tuning.
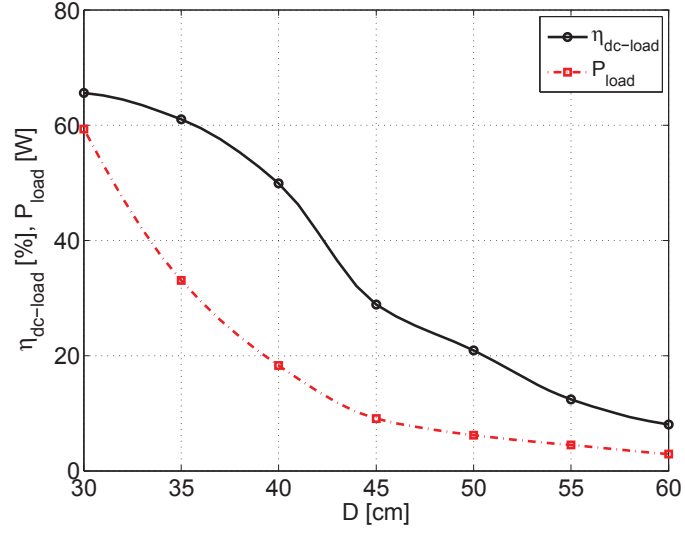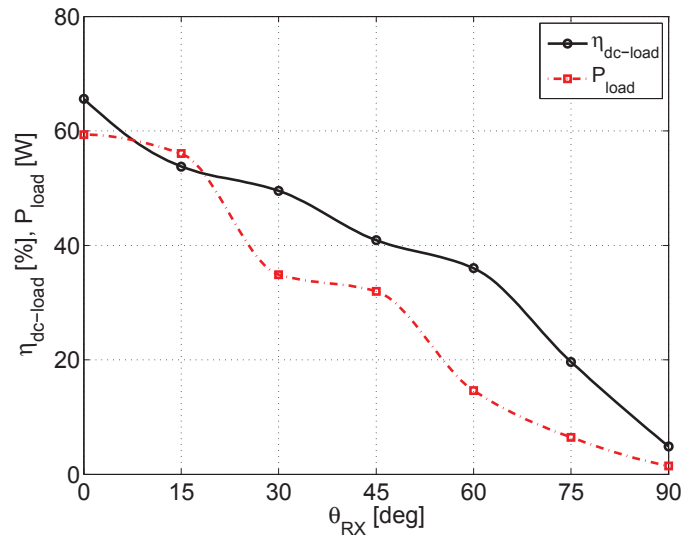

Figure 7.14: Measurement of the dc-to-load efficiency against RX coil angular mis-alignment with fixed clock frequency and load resistance tuning to aligned 30 cm separation distance scenario.
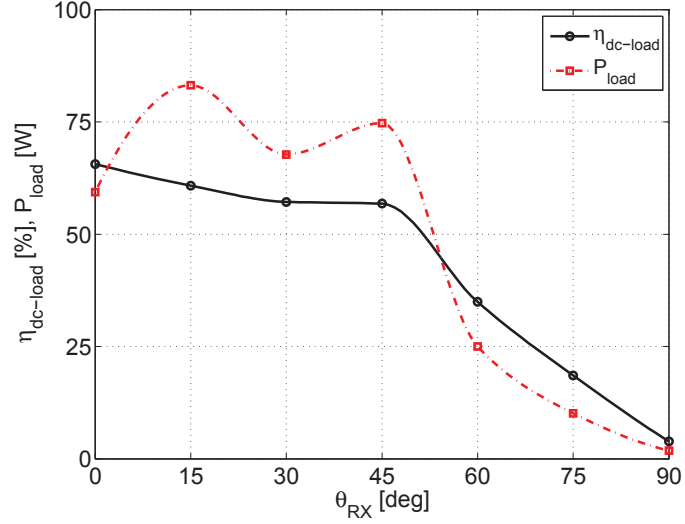
Figure 7.15: Measurement of the dc-to-load efficiency against RX coil angular misalignment with clock frequency tuning.

7.3.3 Maximum DC-to-Load Efficiency

Finally, the efficiency of the system was increased until the power dissipated by the load resistors caused them to overheat and fail. The highest dc-to-load efficiency achieved with the current prototype design is $\eta_{dc\text{-}load} = 77\%$ for an aligned set of coils at a distance of 30 cm with $P_{load} = 105\ W$. The calculated link efficiency based on the unloaded Q and k measurements was 95%. The dc-to-load efficiency of the system was increased, thanks to a higher V_{DD}, which allowed $C_{oss} = C_{par}$. This avoided the use of an external capacitor and allowed for a higher ω_d/ω_{oTX}, which increased the apparent driver inductance of the system. To the authors' knowledge, this is the highest dc-to-load efficiency ever presented for an IPT system, without k enhancement techniques. Table 7.1 compares the results from this with the state of the art of systems using either a coupling enhancement or an optimal frequency approach.

7.4 Conclusion

In this chapter, analysis and experimental results of an IPT system driven by a semi-resonant Class-E amplifier have been presented, demonstrating that by optimizing the systems key variables presented in the previous chapter the dc-to-load efficiency

Table 7.1: IPT Systems Comparison

D [cm]	fo [kHz]	Driver Technology	Coil Technology	Magnetic Material	P_{load} [W]	η_{link} [%]	$\eta_{dc\text{-}load}$ [%]	η_{ee} [%]	Ref.
0	134	Class-E	Litz wire	No	295	-	-	75.7	[33]
0	240	Class-E	Litz wire	No	3.7	71	-	66	[158]
10	20	H-bridge	Litz wire	Yes	2,000	85	-	-	[28]
10	-	-	-	Yes	3,300	-	-	90	[29]
15	6,700	HF transceiver	Loop + pancake coil	No	-	93	-	-	[159]
15	20	H-bridge	Litz wire	Yes	2,000	95	-	-	[139]
18	145	-	Litz wire	Yes	300-3,000	-	-	90	[143, 144, 160]
20	4,000	Class-E	Copper wire coil	No	2	-	50	-	[37]
20	20	H-bridge	Power lines	Yes	60,000	80	-	-	[31]
20	20	H-bridge	Power rail	Yes	27,000	-	-	74	[32]
30	3,700	HF transceiver	Surface spiral	No	220	95	-	-	[38]
30	**6,000**	**Class-E**	**Copper pipe coils**	**No**	**105**	**95**	**77**	-	**[this work]**
18-30, 40*	20	H-bridge	-	Yes	3,000	-	-	> 85	[141, 142]
70	7,650	Signal generator	Loop + pancake coil	No	30	75	-	-	[35]
50	13,560	Class-E	Loop + rectangle coil	No	70	85	70**	-	[36]
50	27,000	HF transceiver	Loop + spiral coil	No	40	47	-	-	[30]
100	508.5	Class-D	Litz wire	No	5-35	76	-	-	[34]
200	9,900	Colpitts oscillator	Litz wire	No	60	50	-	15	[131]

*Maximum power transfer distance stated in the cited website [141]

**Calculated based on estimated value of η_{driver} [36]

of the system can be maximized. This highlights the importance of designing a bespoke driver given a set of defined operation conditions. By doing this, the use of 50 Ω interconnections and impedance matching blocks is avoided and efficiency can be increased.

An indirect thermal method for measuring P_{load} has been presented for the first time with an IPT system to avoid measurement inaccuracies due to load resistance variations and high external electromagnetic fields in the current measurements. This method was compared against (6.1) and well-known coupling factor measurements presented in Chapter 6. A clear correlation can be seen, demonstrating the robustness of the efficiency measurement procedure.

Low cost, high Q coils and a complete design and operational analysis of a semi-resonant Class-E driver for this IPT system has been described. The driver topology and component selection, although constrained by the systems specifications, enabled high frequency, medium power, wireless power transfer for different transmitter and receiver coil sizes. A detailed transverse offset and angular misalignment characterization demonstrated efficiencies above 50%, for transverse offsets up to 14 cm and $\theta_{RX} = 52°$. In addition, dc-to-load efficiencies of 77% were demonstrated in a perfectly aligned scenario, for $D = 30\ cm$, having a link efficiency of 95%.

Finally, a simple but effective frequency tuning procedure proved to increase the efficiency by more than 5%, increasing even further the operational versatility of the system. Although this tuning procedure does not tune the system to perform to its maximum level, as it would if the load is changed for each specific scenario, it provided an effective and relatively simple to implement method of increasing the system's efficiency. This tuning procedure is, therefore, suitable for applications where the receiver or transmitter are constantly varying, such as the case of charging sensors in an aquatic environment.

Part IV

Conclusions and Future Recommendations

8 Conclusions and Future Work

The aim of this work has been to design RF energy harvesters and inductive power transfer systems that can provide power wirelessly at a distance. The technologies previously described in this thesis solve the research questions stated at the beginning of this work, regarding the possibility of harvesting ambient RF power to power a load and a system capable of transmitting tens to hundreds of watts wirelessly without perfect alignment. The main findings, design, optimization and characterizations of each technology are summarized below.

8.1 Overview and Main Findings

8.1.1 Ambient RF Harvesting

The introductory section and literature review of this part highlighted the importance of having a city-wide RF spectral survey as the starting point for the design of ambient RF harvesters. Although several surveys and measurements have been presented before, almost all of them define their measurements based on distance to the nearest transmitter. Throughout this work, it was highlighted why this type of measurements or even a power link budget calculation does not provide enough information about the power densities that could be encountered in an urban environment. Multipath, absorption, diffraction and reflection effects vary dramatically at each location and depend on many factors, such as construction materials, dynamic movement of vehicles and number of people present at the time of the survey, among many others. In addition, the literature review made clear how a harvester powered by a dedicated source varies from one designed to harvest ambient energy.

Using a dedicated transmitter allows to simplify the rectenna system, since the band of operation is generally narrow. This simplifies the antenna design and also allows one to predict the input power to the receiver. Using a dedicated transmitter also allows the rectenna to operate without a power management module, which needs to continuously track the maximum power point. Furthermore, rectifying topologies that are not very efficient, but that achieve higher output voltages, such as a voltage doubler, are generally preferred. In contrast, with an ambient harvester, the transmitter's location is unknown, the antenna needs to be designed to be as omnidirectional as possible, the rectenna topology and rectifying element need to be selected to operate at very low power levels ($<$ -15 dBm) and a power management module, capable of performing maximum power point tracking and providing useful voltage levels are required.

The London RF Survey dataset and analysis allowed us to identify the four largest contributors in an urban and a semi-urban environment. DTV, GSM900, GSM1800 and 3G BTx channels had the largest band power densities, while WiFi was highly dependant on traffic conditions. Multipath effects were highlighted by having more than two orders of magnitude between the average and the maximum power density levels. In addition, by applying an interactive filter in the londonrfsurvey.org website, the locations with the highest power density levels were identified. For all of the selected bands, more than half of the top density locations were found in an urban environment (zones 1-3 of the London Underground). The high power density locations outside these zones were caused by a base station transmitter located exactly on top of the station's exit.

These results helped to define the antenna characteristics needed to increase the input power level, while operating in an urban environment. A rectangular loop was selected as the optimal antenna due to its relatively high gain (4.5 dBi), scalability, ease of fabrication, quasi-omnidirectional radiation pattern and symmetrical front-to-back ratio. Folded dipoles were designed, fabricated and characterized for each one of the selected frequency bands, ensuring that the antennas covered all the selected channel frequencies. With the antennas characterised, the expected input

power level was calculated to be < -15 dBm, helping to determine a suitable rectenna configuration.

Analysis and simulations were performed to compare series, shunt and voltage doubler configurations using COTS Schottky diodes. For the available input power levels, the most efficient rectifying configuration was a single Schottky diode in series with the impedance matching stage. This configuration not only decreases the voltage drop, by using a single device, but allows more efficient impedance matching networks to be used. This is possible because the junction capacitance of the diode dominates the system's impedance and also allows a large smoothing capacitor to be used before the load. The SMS7630 proved to be the most efficient Schottky diode at the input power levels and frequencies target by this work.

Complete single and multi-band rectenna configurations were fabricated, tested and characterised in an urban environment. To cope with the variable input power levels, a power management module with a boost converter and MPPT (from Texas Instruments) was used. The highest end-to-end efficiency was achieved by the 3G rectenna with a distributed impedance matching network, which achieved a 40% efficiency. Series and parallel rectenna topologies were implemented to operate at lower power levels. The series rectenna topology, with a single PMM, proved to achieve a faster cold-start operation but with a very low efficiency due to the inability of the PMM to track the MPP of each band. In contrast, the parallel rectenna configuration, with multiple PMM, was able to cold-start at input power levels as low as -25 dBm.

It was proven that already deployed sources in an urban and semi-urban environment can provide enough power to charge a storage element and power an ultra-low power sensor node, without batteries or cables. It is expected that the harvesters presented in this work will be able to operate in more than 50% of the London Underground stations. In addition, a power density comparison was performed to compare the different prototypes of this work with other energy harvesting technologies. Power densities as high as 10 μW/cm^3 were achieved, making RF harvesting comparable to a thermal generator operated from a human source. This comparison

proves that an RF harvester could be an alternative solution for powering devices in locations where light, vibrations or a thermal gradient are not avaialable or are intermittent.

8.1.2 Inductive Power Transfer

In the second part of this Thesis, the different figures of merit that have been used to characterise and compare inductive power transfer systems were analysed. It was concluded that measuring the efficiency of the link, from the TX coil to the RX coil, provided a limited view of the systems performance and in many cases resulted in a very low end-to-end system efficiency. A detailed summary of the history and state of the art was presented and two main different design approaches were extracted from the analysis. The first one involves focusing on using field-shaping techniques to increase the coupling factor. The second approach relies on operating at the highest possible coil quality factor.

Given the design constraints of the desired system (low cost, lightweight and highly tolerant to misalignments) and the research questions outlined in the first section of this work, the second approach was selected as optimal. This approach implied the design of high Q-factor coils and high frequency power electronics. To start the design of high Q-factor coils, the theory of inductive power transfer systems was reviewed. A Matlab model was generated to design electrically small and efficient coils, by using 1 cm copper pipe. The designed and manufactured coils were characterized using a transmission type method and results were compared against analytic expressions and full-wave EM simulations in CST, where additional work can be performed if a better match between simulations and measurements is required for academic purposes.

Unloaded Qs above 1000 were achieved for both the 30 cm diameter, 3 turn TX coil and the 10 cm diameter, 5 turn coil. These Q-factors were required to achieve a high link efficiency >95%, given the loosely coupled scenario of operation ($k < 0.003$). Having high Q coils without the use of heavy and expensive field shaping techniques also helps to achieve a higher tolerance across variable separation distances, vertical

offsets and angular misalignments.

Once high unloaded Q-factors were achieved, the challenge was to drive the coils efficiently with enough power to deliver tens to hundreds of watts to the load. Given the fact that the optimal frequency was around 5 MHz for the designed coils, a high-power and high-frequency driver topology was required. Different classes of drivers were analysed and compared, such as H-bridges, Class-C, Class-D and Class-E amplifiers. From all of these, only the Class-E amplifier achieved zero-voltage and zero-current at the time of switching. This topology allows for the use of COTS ultra-fast MOSFETs, to be able to cope with the high currents and high voltages required to transfer power wirelessly at high frequencies.

To design the Class-E driver, which did not required an impedance matching network to drive a conventional 50 Ω load, a semi-resonant Class-E was proposed. In this circuit, the transmitter tank is tuned to a higher frequency than the operating frequency, so that the equivalent inductance and resistance of the TX coil and reflected load, appear to be larger. This contributes to higher efficiencies and avoids a free-wheeling operation, due to a low coupling factor that makes the reflected resistance from the RX side undetected by the transmitter. This modification also allowed the circuit to avoid the use of a lumped inductor, that would otherwise be required in series with the TX coil.

A Matlab model and Spice simulations were performed and agreed with measurements of the system in operation. The complete system was implemented and characterised across a broad range of misalignments. The system was able to achieve a dc-to-load efficiency of 77%, with a receive power at the load of 105 W and a separation distance of 30 cm.

During experiments, it was noted that a variation of less than 1% in the operating frequency increased the efficiency of the system by ensuring that proper Class-E operation was achieved, with a zero-voltage and zero-current at the time of switching. Efficiencies higher than 50% were achieved for vertical offsets lower than 14 cm and efficiency increments of more than 5% were achieved at a vertical offset of 20 cm. Efficiencies above 60% were achieved for TX angle variations as high as 75° and

above 40% for RX angle variations as high as 45°. It is important to note that these efficiencies have been achieved only by implementing frequency tuning and the load has not been optimized for each scenario, therefore limiting the maximum efficiency that could be achieved.

These results solve the research questions outlined at the beginning of this work and, according to the author, also show the highest dc-to-load efficiency achieved without coupling enhancement techniques. This work described a novel design for a low-cost, lightweight and efficient inductive power transfer system that will now be used in automotive, medical, industrial and defence applications.

8.2 Author's Contribution

The novel designs and know-how presented in this work have been patented and have attracted investors for the creation of a new enterprise. The main goal of the new enterprise is to continue the research and development of products that can be powered at a distance and without cables. The applications will span a broad range of industries, from ultra-low power and autonomous sensors to high power electric vehicle charging. This section summarizes the main contributions of this work to the fields of radiative and inductive wireless power transfer.

8.2.1 Ambient Power Transfer

The first major contribution of this work was to analyse in detail, compare and differentiate rectennas working from dedicated transmitters and those designed to work from ambient sources. This highlighted the need of a city-wide RF spectral survey, which was performed during this work and is now available online. This survey is the first city-wide RF spectral survey and provides valuable data not only to teams working on RF harvesting but also to health and medical purposes. The analysis performed in the data set allows, for the first time, any research team to know exactly where their RF harvesters should work in London. This survey may prove very valuable to many research teams and plans of expanding its coverage are on its way.

Another contribution was the analysis and comparison of rectifying topologies and rectifying COTS components for true ambient RF harvesting. By comparing rectenna topologies and components across a wide range of frequencies and input power levels, new insight into the pros and cons of each design were highlighted. This helps the designer to select the optimal rectenna design for a specific application. If the input power levels are below -15 dBm a single series rectifier should be used to decrease losses; if higher input power levels are available, a voltage doubler is more suitable. Likewise, depending on the frequency of operation, the analysis presented here allows the designer to choose the optimal Schottky diode for a specific channel.

One of the major contributions of this work was to demonstrate the operation of an RF energy harvester working from a wide range of ambient sources. The demonstration and measurement results were undertaken in a real urban environment, avoiding the use of dedicated sources used to emulate a base station transmitter. This experiments highlighted the variability of input power levels and frequencies that a real ambient harvesters needs to cope with. According to the author, this is the first time that an ambient harvester is capable of operating from frequency channels that span such a large bandwidth (from 0.5 - 2.5 GHz) and with high efficiencies.

Furthermore, series and parallel arrays of full operating harvesters, including maximum power point tracking and a boost converter, were presented. Analysis of the pros and cons of each architecture were presented and it was shown how this topologies can increase the freedom of operation with multi-band harvesters. In addition, ways of implementing a bypass circuit, with the use of a modified folded dipole and without the need of an additional diode, were described. These architectures were able to cold-start the harvester at input power levels as low as -29 dBm.

Finally, the last contribution of this section was to show the potential of RF energy harvesting as a real alternative to other energy harvesting technologies. Given the high power density achieved by the RF harvesting prototypes, RF energy harvesting can achieve similar or even higher power densities than harvesters that rely on vibrations and temperature fluctuations.

8.2.2 Inductive Power Transfer

The first contribution in this line of work was with the analysis, comparison and categorization of inductive power transfer systems. In this analysis, the division of systems by those using field shaping techniques and those using high Q-factor coils highlighted the importance of approaching the system design, by focusing in on the end-to-end efficiency of the system and not only the link efficiency. This also provided a clear understanding of all the system blocks, key differentiators and optimization possibilities in each one of them.

The second contribution came from developing models for the design of high Q-factor coils using conventional copper piping. The analysis presented in the corresponding section in this thesis provides the methodology to achieve unloaded Q-factor above a thousand, for lightweight, low cost and scalable coils. Reliable characterization techniques were presented for non-trivial Q measurements, highlighting the difficulties of each procedure.

The key contribution of this work was the design of a scalable semi-resonant Class-E coil driver. The coil driver is capable of driving directly the TX coil, without a complex and lossy impedance matching stage, whilst achieving high efficiencies at megahertz frequencies and power levels ranging from tens to hundreds of watts. This driver topology is capable of achieving the latter by using high frequency COTS driver/MOSFET modules. To achieve these efficiencies, Matlab codes, PSpice simulations, as well as know-how relating to the PCB layout and component selection was generated and is now protected (patent pending) to be used by the new enterprise.

By combining the previous two contributions, a high efficiency and flexible IPT system was designed and fabricated. The system's design allows it to work in a wide range of misalignment scenarios and the novel frequency tuning technique allows the system to achieve this with high efficiencies. The contribution related to frequency tuning allows for a simple but effective tuning mechanism that can be automated with existing technologies.

Furthermore, a contribution was undertaken in providing a novel but reliable efficiency measurement technique. The previously described thermal measurement

technique allows a consistent and accurate methodology for measuring WPT systems where high voltages, high currents and EM fields make the use of conventional probes unreliable. By using this technique, measurements can be done without needing current probe shielding or high voltage probes.

Finally, the last contribution of this work was to prove that power can be transferred wirelessly and efficiently without heavy and expensive ferromagnetic materials. Also, it proved that high misalignment tolerances can be achieved with a lightweight system, if the system is optimized as a whole and not by stages, as many teams have done in the past. This work provides a complete design framework to supply power at a distance, without cables, to a broad range of applications and scenarios.

8.2.3 Collaboration

This research has been the result of a collaborative work done together with Dr Stepan Lucyszyn, Dr Paul D. Mitcheson and Dr David C. Yates. Besides their continuous supervision, several of the ideas that have arisen from this work were generated in meetings or during experiments. More specifically, Dr Yates' Matlab models of inductive power transfer systems helped with the initial design of the coils and the modified Class-E amplifier. Dr Lucyszyn provided the initial design approach on the antennas and rectifiers, guidance with the design and measurement techniques of the RF energy harvesters and Dr Mitcheson provided ideas and solutions to system design problems and help with troubleshooting power electronics and RF systems. In addition, all of them contributed continuously to both technologies by providing insight into the various systems iterations. The London RF Survey was carried out by a team of ten graduate students from the Optical and Semiconductor Devices Group and Control and Power Group at ICL, shown in Fig. 8.1, and the londonrfsurvey.org website was designed by Dr James Dicken. Two undergraduate students, George Pappas and Gonzalo de Gisbert, provided valuable help with the initial IPT system design and experiments.

Figure 8.1: ICL team (from left to right): Dr Paul D. Mitcheson, Chen Wang, Fangjing Hu, Manuel Pinuela (above), Dr Stepan Lucyszyn (below), Stergios Papantonis, Alwyn Elliot, Elpida Episkopou, Mario D'Auria, Shuo Yang and, not shown, Dr James Dicken (web page developer)
.

8.3 Suggestions for Future Work

Throughout the life of this work, several potential research avenues have been identified and are now described. Some of these avenues have already been started to be explored in follow-on projects that have arisen from this work and will be further developed in the new enterprise.

8.3.1 Ambient RF Harvesting

Interest in the London RF Survey, from public and private companies, as well as governments, has generated the need of having an updated dataset and expand its coverage. With the full DTV switch-over happening a month after the initial survey ended and with the deployment of 4G in London, new channels have to be investigated. It is very likely that higher power densities are now available in London. For these reasons, a new survey covering all the pre-existing and the new channels should be performed in London and in other parts of the UK. The coverage of rural and open field scenarios would provide more information on the power density

distribution and would potentially shine light onto other applications. Furthermore, research agreements are being put in place with research institutions and companies abroad to expand the coverage of the survey to other countries. Finally, it would be very valuable to also cover different scenarios, such as buses, trains and offices and expand the potential locations where RF harvesters could be deployed.

More efficient antenna designs need to be explored. These new antennas should be omnidirectional and ideally integrate or simplify the integration with the rectifying circuit. This could be approached by fabricating modified monopoles in more efficient substrates than FR4, such as Rogers Duroid. The antenna could be also conjugately matched to the rectifier, to decrease the losses in the impedance matching stage. Conformal antennas should also be explored to increase the power density of the harvester. By having a conformal antenna that could be concealed or embedded into an existing surface, the total volume occupied by the harvester would decrease.

Other rectifying topologies, such as modified full-wave rectifiers could be explored and analysed in a similar fashion, as it was undertaken with the series, shunt and voltage doubler architectures. In addition, an updated COTS rectifier comparison should be performed including MOSFETS. Efficiency could also be increased and spaced saved by integrating and packaging the rectifier and the PMM.

Special effort could be placed into decreasing the cold-start voltage and power requirements of the Texas Instrument chip by stripping several of the system blocks that were originally implemented to make it a general solution for energy harvesters. The battery control blocks could be simplified, as well as the under or over voltage systems that are implemented to protect Li-Ion batteries.

In addition, rectenna arrays could be designed so that the harvester could achieve a cold-start voltage faster, by switching from a series to a parallel topology once the PMM starts to work. Once it is working, a single PMM could be used to hot-start the other PMM and increase the freedom of operation of the harvesting array. The array would also allow the user to harvest larger amounts of power in scenarios where power hungry applications are required, or also in locations where lower power densities are expected.

Finally, full autonomous systems powered by ambient RF energy could be integrated. This integrated systems could be remote wireless sensors, which could work in low duty cycles and sense and transmit data in application where continuous data streams are not required.

8.3.2 Inductive Power Transfer

Due to the range of applications that this technology will be applied to, smaller coil designs need to be approached. Coil designs such as the surface spiral, presented in the literature review, could potentially provide the same Q-factors, as with the current designs, but in a smaller form factor. Size constraints will not only require novel fabrication techniques, such as multilayered printable inductors, but also create new challenges relating to the possible Q-factors that can be achieved.

Although a larger transmitter would increase the separation distance that the IPT system can achieve, a drastic size difference will imply that one of the two coils will not operate at its highest Q. Analysis and simulations of the optimal point of operation needs to be performed, ideally with a full-wave 3D simulator. In addition to these simulations, a complete system simulation, which includes the driver circuitry and the link could be implemented and reduce the tuning iterations that are currently required to achieve Class-E operation.

An efficient oscillator needs to be integrated into the Class-E amplifier and ideally integrated into the gate driver and MOSFET module. By doing this, automated frequency tuning could be implemented by measuring the transmitted and received power levels. Implementing an automated frequency tuning circuit could increase the misalignment tolerances of the system and make it suitable for other applications, such as rotating machines.

On the receiver side, rectifier topologies should be investigated. Full-wave and resonant rectifier topologies, such as Class-E have great potential of achieving rectification at high frequencies and high power levels efficiently. Besides the rectification stage, a power conversion stage and load emulator are required, so that the IPT system always sees the optimal load even in dynamic conditions. This could

be implemented with a similar circuit to that applied in the RF energy harvesting power management module.

Due to the potential applications in the medical devices area, it would be interesting to test the system performance in ex-vivo experiments. This could be performed first with simulations using human models such as Visible Human Project. Experiments could then be carried to confirm simulations by using animals or artificial tissue.

It is key that a full investigation of EM fields surrounding the IPT system are carried out to comply with international regulations. Safety mechanisms, such as proximity detection with PIR sensors, need to be implemented to ensure that the system is safe. Complete simulations with human body models need to be carried out to ensure that the safety standards are met for each body part. In addition, magnetic fields should be measured to define an exclusion zone, where appropriate.

The current system requires and exclusion zone of less than 40 cm from the centre of the TX coil, but safety measures should be taken, especially if the system is to be used with higher power applications. Besides complying with international safety standards, the system must also comply with EMI regulations. Crude experiments have been performed by operating different electronic devices near the IPT system, with no problems. However, field probe testing should be performed across different devices. Finally, a fully integrated system needs to be designed by having an integrated rectifying and power conditioning stage.

8.4 Publications and Output

8.4.1 Patents

- M. Pinuela , P. D. Mitcheson, S. Lucyszyn and D. C. Yates (inventors), *Wireless power transfer system*, GB1215152.8, filed 24th Aug. 2012 (Patent Pending)

8.4.2 Journals

- M. Pinuela, P. D. Mitcheson and S. Lucyszyn, *Ambient RF energy harvesting in urban and semi-urban environments*, IEEE Transactions on Microwave Theory and Techniques, vol. 61, no. 7, pp. 2715-2726, July 2013.

- M. Pinuela, D. C. Yates, S. Lucyszyn, and P. D. Mitcheson, *Maximizing DC-to-Load Efficiency for Inductive Power Transfer*, IEEE Transactions on Power Electronics, vol. 28, no. 5, pp. 2437-2447, May 2013.

8.4.3 Conferences

- M. Pinuela, D. C. Yeats, P. D. Mitcheson and S. Lucyszyn, *London RF survey, suitable ambient RF energy harvesters and efficient DC-load inductive power transfer*, 7th EurAAP European Conference on Antennas and Propagation (EUCAP 2013), Gothenburg, Sweden, pp. 2752-2756, Apr. 2013 (Invited Paper)

- M. Pinuela, D. C. Yates, S. Lucyszyn, P. D. Mitcheson, *The New Wireless*, Energy Harvesting 2013, EPSRC Energy Harvesting Network, London, Mar. 2013 (Best Poster prize)

- M. Pinuela, D. C. Yates, S. Lucyszyn and P. D. Mitcheson, *Current state of research at Imperial College London in RF harvesting and inductive power transfer*, 2nd International Workshop on Wireless Energy Transport and Harvesting (IWWETH), Leuven, Belgium, May 2012 (Invited Paper)

- M. Pinuela, D. C. Yates, P. D. Mitcheson, S. Lucyszyn, *Maximising the link efficiency of resonant inductive coupling for wireless power transfer*, 1st International Workshop on Wireless Energy Transport and Harvesting (IWWETH), Eindhoven, The Netherlands, Jun. 2011 (Talk)

- M. Pinuela, *Exploring Innovations*, Unwired Exhibition, Royal College of Art, London, UK. 2011

- M. Pinuela, P. D. Mitcheson and S. Lucyszyn, *Analysis of scalable rectenna configurations for harvesting high frequency ambient radiation*, The 10th International Workshop on Micro and Nanotechnology for Power Generation and Energy Conversion Applications (PowerMEMS 2010), Leuven, Belgium, pp. 41-44, Nov. 2010

Bibliography

[1] W. C. Brown, "The history of power transmission by radio waves," *IEEE transactions on microwave theory and techniques*, vol. MTT-32, pp. 1230–1242, 1984.

[2] T. Le, K. Mayaram, and T. Fiez, "Efficient far-field radio frequency energy harvesting for passively powered sensor networks," *Solid-State Circuits, IEEE Journal of*, vol. 43, no. 5, pp. 1287–1302, 2008.

[3] C. Mikeka, H. Arai, A. Georgiadis, and A. Collado, "DTV band micropower RF energy-harvesting circuit architecture and performance analysis," in *2011 IEEE International Conference on RFID-Technologies and Applications (RFID-TA)*. IEEE, Sep. 2011, pp. 561–567.

[4] Y.-J. Ren and K. Chang, "New 5.8-GHz circularly polarized retrodirective rectenna arrays for wireless power transmission," *Microwave Theory and Techniques, IEEE Transactions on*, vol. 54, no. 7, pp. 2970–2976, 2006.

[5] S. Keyrouz, H. J. Visser, and A. G. Tijhuis, "Ambient RF energy harvesting from DTV stations," in *Antennas and Propagation Conference (LAPC), 2012 Loughborough*, Nov. 2012, pp. 1–4.

[6] S.A. Bhalerao, A.V. Chaudhary, R.B. Deshmukh, and R.M. Patrikar, "Powering wireless sensor nodes using ambient RF energy," in *Systems, Man and Cybernetics, 2006. SMC '06. IEEE International Conference on*, vol. 4, 2006, pp. 2695–2700.

[7] J. Y. Park, S. M. Han, and T. Itoh, "A rectenna design with harmonic-rejecting

circular-sector antenna," *Antennas and Wireless Propagation Letters, IEEE*, vol. 3, pp. 52–54, 2004.

[8] D. Bouchouicha, F. DuPont, M. Latrach, and L. Ventura, "Ambient RF energy harvesting," in *ICREPQ'10*, Granada, Spain, Mar. 2010, pp. 1–5.

[9] V. Rizzoli, G. Bichicchi, A. Costanzo, F. Donzelli, and D. Masotti, "CAD of multi-resonator rectenna for micro-power generation," in *Microwave Integrated Circuits conference, 2009. EuMIC 2009. European*, 2009, pp. 331–334.

[10] J. McSpadden, T. Yoo, and K. Chang, "Theoretical and experimental investigation of a rectenna element for microwave-power transmission," *IEEE Transactions on Microwave Theory and Techniques*, vol. 40, no. 12, pp. 2359–2366, Dec. 1992.

[11] International Commission on Non-Ionizing Radiation Protection, "Guidelines for limiting exposure to time- varying electric, magnetic, and electromagnetic fields (up to 300 GHz)," *Health Physics*, vol. 74, no. 4, pp. 494–522, 1998.

[12] S. M. Mann, T. G. Cooper, S. G. Allen, R. P. Blackwell, and A. J. Lowe, *Exposure to radio waves near mobile phone base stations*. National Radiological Protection Board, 2000.

[13] P. Frei, E. Mohler, G. Neubauer, G. Theis, A. Burgi, J. Frohlich, C. Braun-Fahrlander, J. Bolte, M. Egger, and M. Roosli, "Temporal and spatial variability of personal exposure to radio frequency electromagnetic fields," *Environmental Research*, vol. 109, no. 6, pp. 779–785, Aug. 2009.

[14] J. Moulder, K. Foster, L. Erdreich, and J. McNamee, "Mobile phones, mobile phone base stations and cancer: a review," Feb. 2005.

[15] T. G. Cooper, S. M. Mann, M. Khalid, and R. P. Blackwell, "Public exposure to radio waves near GSM microcell and picocell base stations," *Journal of Radiological Protection*, vol. 26, no. 2, pp. 199–211, 2006.

[16] Y.-H. Suh and K. Chang, "A novel low-cost high-conversion-efficiency microwave power detector using GaAs FET," *Microwave and Optical Technology Letters*, vol. 44, no. 1, pp. 29–31, 2005.

[17] Transport for London, "London undeground map," Aug. 2012. [Online]. Available: http://www.tfl.gov.uk/gettingaround/1106.aspx

[18] Agilent Technologies Inc., "Agilent FieldFox RF analyser N9912A 4/6 GHz (technical overview)," May 2012.

[19] Aaronia AG, "Biconical EMC broadband antennas - BicoLOG series (data sheet)," 2012.

[20] M. Pinuela, P. Mitcheson, and S. Lucyszyn, "Ambient RF energy harvesting in urban and semi-urban environments," *IEEE Transactions on Microwave Theory and Techniques*, vol. 61, no. 7, pp. 2715–2726, 2013.

[21] M. Pinuela, P. D. Mitcheson, and S. Lucyszyn, "Analysis of scalable rectenna configurations for harvesting high frequency ambient radiation," in *Proceedings of PowerMEMS 2010*, Leuven, Belgium, Dec. 2010.

[22] Texas Instruments, "BQ25540 datasheet: Ultra low power boost converter with battery management for energy harvester applications," 2012.

[23] P.D. Mitcheson, E.M. Yeatman, G.K. Rao, A.S. Holmes, and T.C. Green, "Energy harvesting from human and machine motion for wireless electronic devices," *Proceedings of the IEEE*, vol. 96, no. 9, pp. 1457–1486, 2008.

[24] R. Vullers, R. Schaijk, H. Visser, J. Penders, and C. Hoof, "Energy harvesting for autonomous wireless sensor networks," *Solid-State Circuits Magazine, IEEE*, vol. 2, no. 2, pp. 29–38, 2010.

[25] V. Leonov, P. Fiorini, S. Sedky, T. Torfs, and C. Van Hoof, "Thermoelectric MEMS generators as a power supply for a body area network," in *The 13th International Conference on Solid-State Sensors, Actuators and Microsystems,*

2005. Digest of Technical Papers. Tansducers '05, vol. 1, Jun. 2005, pp. 291 – 294 Vol. 1.

[26] J. C. Schuder, "Powering an artificial heart: Birth of the inductively coupled-radio frequency system in 1960," *Artificial Organs*, vol. 26, no. 11, pp. 909–915, 2002.

[27] D. Schneider, "Wireless power at a distance is still far away [electrons unplugged]," *Spectrum, IEEE*, vol. 47, no. 5, pp. 34–39, 2010.

[28] M. Budhia, G. A. Covic, and J. T. Boys, "Design and optimization of circular magnetic structures for lumped inductive power transfer systems," *IEEE Trans. Power Electron.*, vol. 26, no. 11, pp. 3096–3108, Nov. 2011.

[29] "Plugless Power," Feb. 2012. [Online]. Available: http://www.pluglesspower.com/

[30] B. Wang, K. H. Teo, T. Nishino, W. Yerazunis, J. Barnwell, and J. Zhang, "Experiments on wireless power transfer with metamaterials," *Applied Physics Letters*, vol. 98, no. 25, Jun. 2011.

[31] S. Ahn and J. Kim, "Magnetic field design for high efficient and low emf wireless power transfer in on-line electric vehicle," in *Proc. of the 5th European Conf. on Antennas and Propag. (EUCAP)*, Apr. 2011, pp. 3979–3982.

[32] J. J. Huh, S. W. Lee, W. Y. Lee, G. H. Cho, and C. T. Rim, "Narrow-width inductive power transfer system for online electrical vehicles," *IEEE Trans. on Power Electron.*, vol. 26, no. 12, pp. 3666–3679, Dec. 2011.

[33] Z. N. Low, R. Chinga, R. Tseng, and J. Lin, "Design and test of a high-power high-efficiency loosely coupled planar wireless power transfer system," *IEEE Trans. Ind. Electron.*, vol. 56, no. 5, pp. 1801–1812, May 2009.

[34] J. Garnica, J. Casanova, and J. Lin, "High efficiency midrange wireless power transfer system," in *Microwave Workshop Series on Innovative Wireless Power*

Transmission: Technologies, Systems, and Applications (IMWS), 2011 IEEE MTT-S International, May 2011, pp. 73–76.

[35] A. P. Sample, D. A. Meyer, and J. R. Smith, "Analysis, experimental results, and range adaptation of magnetically coupled resonators for wireless power transfer," *IEEE Trans. Ind. Electron.*, vol. 58, no. 2, pp. 544–554, Feb. 2011.

[36] N. Y. Kim and K. Y. Kim, "Automated frequency tracking system for efficient mid-Řrange magnetic resonance wireless power transfer," *Microwave and Optical*, vol. 54, no. 6, pp. 1423–1426, Jun. 2012.

[37] L. Chen, S. Liu, Y. Zhou, and T. Cui, "An optimizable circuit structure for high-efficiency wireless power transfer," *IEEE Trans. Ind. Electron.*, vol. PP, no. 99, pp. 1–1, Dec. 2011.

[38] S. H. Lee and R. D. Lorenz, "Development and validation of model for 95% efficiency, 220W wireless power transfer over a 30-cm air-gap," *IEEE Trans. on Ind. Appl.*, vol. 47, no. 6, pp. 2495–2504, Sep. 2011.

[39] M. Pinuela, D. C. Yates, P. D. Mitcheson, and S. Lucyszyn, "Maximising the link efficiency of resonant inductive coupling for wireless power transfer," in *1st International Workshop on Wireless Energy Transport and Harvesting*, Eindhoven, The Netherlands, Jun. 2011.

[40] M. Pinuela, D. C. Yates, S. Lucyszyn, and P. D. Mitcheson, "Maximizing DC-to-Load efficiency for inductive power transfer," *IEEE Transactions on Power Electronics*, vol. 28, no. 5, pp. 2437 –2447, May 2013.

[41] K. V. Schuylenbergh and R. Puers, *Inductive Powering: Basic Theory and Application to Biomedical Systems.* Springer, Jul. 2009.

[42] "Practical wireless," *Practical Wireless*, p. 835, Jan. 1965.

[43] T. Salter, G. Metze, and N. Goldsman, "Parasitic aware optimization of an RF power scavenging circuit with applications to smartdust sensor networks,"

in *Radio and Wireless Symposium, 2009. RWS '09. IEEE*, Jan. 2009, pp. 332–335.

[44] SENSIMED, "Triggerfish continuous IOP monitoring," Mar. 2012. [Online]. Available: http://www.sensimed.com/S-Trig-glaucoma.htm

[45] P. E. Glaser, "Power from the sun: Its future," *Science*, vol. 162, no. 3856, pp. 857–861, 1968.

[46] J. J. Schlesak, A. Alden, and T. Ohno, "A microwave powered high altitude platform," in *Microwave Symposium Digest, 1988., IEEE MTT-S International*, 1988, pp. 283–286.

[47] H. Visser and R. Vullers, "RF energy harvesting and transport for wireless sensor network applications: Principles and requirements," *Proceedings of the IEEE*, vol. Early Access Online, 2013.

[48] N. Shinohara, "Power without wires," *IEEE Microwave Magazine*, vol. 12, no. 7, pp. S64–S73, Dec. 2011.

[49] K. Finkenzeller, *RFID Handbook: Radio-Frequency Identification Fundamentals and Applications.* John Wiley, 2000.

[50] W. Joseph, G. Vermeeren, L. Verloock, M. M. Heredia, and L. Martens, "Characterization of personal RF electromagnetic field exposure and actual absorption for the general public," *Health Physics*, vol. 95, no. 3, pp. 317–330, Sep. 2008, PMID: 18695413.

[51] G. Thuroczy, F. Molnar, J. Szabo, G. Janossy, N. Nagy, G. Kubinyi, and J. Bakos, "Public exposure to RF from installed sources: Site measurements and personal exposimetry," in *Antennas and Propagation, 2006. EuCAP 2006. First European Conference on*, 2006, pp. 1–4.

[52] H. Visser, A. Reniers, and J. Theeuwes, "Ambient RF energy scavenging: GSM and WLAN power density measurements," in *Microwave Conference, 2008. EuMC 2008. 38th European*, 2008, pp. 721–724.

[53] P. Elliott, M. B. Toledano, J. Bennett, L. Beale, K. de Hoogh, N. Best, and D. J. Briggs, "Mobile phone base stations and early childhood cancers: case-control study," *BMJ*, vol. 340, no. 1, p. c3077, Jun. 2010.

[54] L. Guenda, A. Collado, N. Carvalho, A. Georgiadis, and K. Niotaki, "Electromagnetic geo-referenced footprints for energy harvesting systems," in *Radio and Wireless Symposium (RWS), 2012 IEEE*, Jan. 2012, pp. 339 –342.

[55] J. Y. Park, S. M. Han, and T. Itoh, "A rectenna design with harmonic-rejecting circular-sector antenna," *Antennas and Wireless Propagation Letters, IEEE*, vol. 3, pp. 52–54, 2004.

[56] "Nihon Dengyo Kosaku Co., Ltd," Jul. 2012. [Online]. Available: http://www.den-gyo.com/solution/solution01.html

[57] V. Marian, B. Allard, C. Vollaire, and J. Verdier, "Strategy for microwave energy harvesting from ambient field or a feeding source," *Power Electronics, IEEE Transactions on*, vol. 27, no. 11, pp. 4481 –4491, Nov. 2012.

[58] P. Vecchia, R. Matthes, G. Ziegelberger, J. Lin, R. Saunders, and A. Swerdlow, "Exposure to high frequency electromagnetic fields, biological effects and health consequences (100 kHz-300 GHz)," International Commision on Non-Ionizing Radiation Protection, Germany, Tech. Rep. ICNIRP 16/2009, 2009, ISBN 978-3-934994-10-2.

[59] G. Neubauer, M. Feychting, Y. Hamnerius, L. Kheifets, N. Kuster, I. Ruiz, J. SchÃijz, R. Uberbacher, J. Wiart, and M. RÃűÃűsli, "Feasibility of future epidemiological studies on possible health effects of mobile phone base stations," *Bioelectromagnetics*, vol. 28, no. 3, pp. 224–230, Apr. 2007, PMID: 17080459.

[60] "Electromagnetic fields and public health," May 2006. [Online]. Available: http://www.who.int/mediacentre/factsheets/fs304/en/index.html

[61] M. Riederer, "EMF exposure due to GSM base stations: measurements and

limits," in *Electromagnetic Compatibility, 2003. EMC '03. 2003 IEEE International Symposium on*, vol. 1, 2003, pp. 402–405 Vol.1.

[62] V. Nitu, G. Lojewski, and S. Nitu, "Electromagnetic field evaluation on an antennas shared," in *EUROCON 2009, IEEE*, 2009, pp. 70–75.

[63] Y. Kawahara, K. Tsukada, and T. Asami, "Feasibility and potential application of power scavenging from environmental RF signals," in *Antennas and Propagation Society International Symposium, 2009. APSURSI '09. IEEE*, Jun. 2009, pp. 1–4.

[64] J. B. Burch, M. Clark, M. G. Yost, C. T. Fitzpatrick, A. M. Bachand, J. Ramaprasad, and J. S. Reif, "Radio frequency nonionizing radiation in a community exposed to radio and television broadcasting," *Environmental Health Perspectives*, vol. 114, no. 2, pp. 248–253, Feb. 2006, PMID: 16451862 PMCID: 1367839.

[65] S. Henderson and M. Bangay, "Survey of RF exposure levels from mobile telephone base stations in australia," *Bioelectromagnetics*, vol. 27, no. 1, pp. 73–76, 2006.

[66] C. Bornkessel, M. Schubert, M. Wuschek, and P. Schmidt, "Measurement and calculation of general public electromagnetic exposure around GSM and UMTS cellular base stations," in *Antennas, 2007. INICA '07. 2nd International ITG Conference on*, 2007, pp. 225–229.

[67] P. Frei, E. Mohle, A. Burgi, J. Frohlich, G. Neubauer, C. Braun-Fahrlander, and M. Roosli, "A prediction model for personal radio frequency electromagnetic field exposure," *Science of the Total Environment*, no. STOTEN-11534, p. 7, Sep. 2009.

[68] Y. Hamnerius, "Measurements of human exposure from emerging wireless technologies," *The Environmentalist*, vol. 29, no. 2, pp. 118–123, Jun. 2009.

[69] R. Hamid, M. Cetintas, H. Karacadag, A. Gedik, M. Yogun, M. Celik, and

A. Firlarer, "Measurement of electromagnetic radiation from GSM base stations," in *Electromagnetic Compatibility, 2003. EMC '03. 2003 IEEE International Symposium on*, vol. 2, 2003, pp. 1211–1214 Vol.2.

[70] L. Challis, "Mobile telecommunication and health research programme report," Health Protection Agency Radiation Protection Division, Chilton, Didcot, Osfrodshire OX11 0RQ, UK, Tech. Rep. 2007, 2007.

[71] J. F. Viel, S. Clerc, C. Barrera, R. Rymzhanova, M. Moissonnier, M. Hours, and E. Cardis, "Residential exposure to radiofrequency fields from mobile phone base stations, and broadcast transmitters: a population-based survey with personal meter," *British Medical Journal*, vol. 66, no. 8, p. 550, 2009.

[72] "Cisco router." [Online]. Available: http://www.cisco.com/en/US/prod/prod_white_paper09186a0080088791.pdf

[73] "CES 2010: 'Airnergy' gadget promises wireless charging over wi-fi." [Online]. Available: http://www.guardian.co.uk/technology/2010/jan/11/ces-airnergy

[74] J.-F. Viel, E. Cardis, M. Moissonnier, R. de Seze, and M. Hours, "Radiofrequency exposure in the french general population: Band, time, location and activity variability," *Environment International*, vol. 35, no. 8, pp. 1150–1154, Nov. 2009.

[75] R. H. Chen, L. Y. C., and S. J. S., "Design and experiment of a loop rectenna for RFID wireless power transmission and data communication applications," in *PIERS Proceedings*, Beijing, China, Mar. 2009, pp. 528–531.

[76] T. Paing, J. Morroni, A. Dolgov, J. Shin, J. Brannan, R. Zane, and Z. Popovic, "Wirelessly-powered wireless sensor platform," in *Wireless Technologies, 2007 European Conference on*, 2007, pp. 241–244.

[77] S. Gregori, Y. Li, H. Li, J. Liu, and F. Maloberti, "2.45 GHz power and data transmission for a low-power autonomous sensors platform," in *Low Power Electronics and Design, 2004. ISLPED '04. Proceedings of the 2004 International Symposium on*, 2004, pp. 269–273.

[78] S. Riviere, A. Douyere, F. Alicalapa, and J.-D. Luk, "Study of complete WPT system for WSN applications at low power level," *Electronics Letters*, vol. 46, no. 8, pp. 597–598, 2010.

[79] Y.-J. Ren and K. Chang, "5.8-GHz circularly polarized dual-diode rectenna and rectenna array for microwave power transmission," *Microwave Theory and Techniques, IEEE Transactions on*, vol. 54, no. 4, pp. 1495–1502, 2006.

[80] K. Fujimori, K. Tada, Y. Ueda, M. Sanagi, and S. Nogi, "Development of high efficiency rectification circuit for mW-class rectenna," in *Microwave Conference, 2005 European*, vol. 2, 2005, p. 4 pp.

[81] J. McSpadden, L. Fan, and K. Chang, "A high conversion efficiency 5.8 GHz rectenna," in *Microwave Symposium Digest, 1997., IEEE MTT-S International*, vol. 2, 1997, pp. 547–550 vol.2.

[82] W.-H. Tu, S.-H. Hsu, and K. Chang, "Compact 5.8-GHz rectenna using stepped-impedance dipole antenna," *Antennas and Wireless Propagation Letters, IEEE*, vol. 6, pp. 282–284, 2007.

[83] S. Lucyszyn, J. Luck, G. Green, and I. Robertson, "Enhanced modelling of interdigitated planar schottky varactor diodes," in *Microwave Conference, 1992. APMC 92. 1992 Asia-Pacific*, vol. 1, 1992, pp. 273–278.

[84] S. Kitazawa, H. Ban, and K. Kobayashi, "Energy harvesting from ambient RF sources," in *Microwave Workshop Series on Innovative Wireless Power Transmission: Technologies, Systems, and Applications (IMWS), 2012 IEEE MTT-S International*, May 2012, pp. 39 –42.

[85] R. Vyas, V. Lakafosis, and M. Tentzeris, "Wireless remote localization system utilizing ambient RF/solar power scavenging RFID tags," ser. 2010 IEEE/MTT-S International Microwave Symposium - MTT 2010. Piscataway, NJ, USA: IEEE, 2010, pp. 1764–1767, copyright 2010, The Institution of Engineering and Technology.

[86] H. Nishimoto, Y. Kawahara, and T. Asami, "Prototype implementation of ambient RF energy harvesting wireless sensor networks," in *2010 IEEE Sensors.* IEEE, Nov. 2010, pp. 1282–1287.

[87] A. Sample and J. Smith, "Experimental results with two wireless power transfer systems," in *Radio and Wireless Symposium, 2009. RWS '09. IEEE*, Jan. 2009, pp. 16 –18.

[88] D. W. Harrist, "Wireless battery charging system using radio frequency energy harvesting," Master Thesis, University of Pittsburgh, 2004.

[89] C. E. Greene, D. W. Harrist, and J. G. Shearer, "Method and apparatus for implementation of a wireless power supply," Patent United States Patent 7 812 771, Oct., 2010.

[90] "Powercast corporation." [Online]. Available: http://www.powercastco.com/

[91] J. Ayers, K. Mayaram, and T. S. Fiez, "An ultralow-power receiver for wireless sensor networks," *Solid-State Circuits, IEEE Journal of*, vol. 45, no. 9, pp. 1759–1769, 2010.

[92] T. T. Le, T. S. Flez, and K. Mayaram, "RF harvesting circuit," U.S. Patent, Jun., 2009.

[93] T. Salter, K. Choi, M. Peckerar, G. Metze, and N. Goldsman, "RF energy scavenging system utilizing switched capacitor DC-DC converter," *Electronics Letters*, vol. 45, no. 7, pp. 374–376, 2009.

[94] H. Jabbar, Y. Song, and T. T. Jeong, "RF energy harvesting system and circuits for charging of mobile devices," *IEEE Transactions on Consumer Electronics*, vol. 56, no. 1, pp. 247–253, 2010.

[95] C. Mikeka and H. Arai, "Design of a cellular energy-harvesting radio," in *Wireless Technology Conference, 2009. EuWIT 2009. European*, 2009, pp. 73–76.

[96] R. J. Vullers, H. J. Visser, B. O. het Veld, and V. Pop, "RF harvesting using antenna structures on foil," *Proc. of PowerMEMS*, p. 10âĂŞ11, 2008.

[97] V. Rizzoli, D. Masotti, N. Arbizzani, and A. Costanzo, "CAD procedure for predicting the energy received by wireless scavenging systems in the near- and far-field regions," in *Microwave Symposium Digest (MTT), 2010 IEEE MTT-S International*, 2010, pp. 1768–1771.

[98] A. Costanzo, F. Donzelli, D. Masotti, and V. Rizzoli, "Rigorous design of RF multi-resonator power harvesters," in *Antennas and Propagation (EuCAP), 2010 Proceedings of the Fourth European Conference on*, 2010, pp. 1–4.

[99] A. Costanzo, A. Romani, D. Masotti, N. Arbizzani, and V. Rizzoli, "RF/baseband co-design of switching receivers for multiband microwave energy harvesting," *Sensors and Actuators A: Physical*, vol. 179, no. 0, pp. 158–168, Jun. 2012.

[100] G. Andia, A. Georgiadis, A. Collado, and S. Via, "Design of a 2.45 GHz rectenna for electromagnetic (EM) energy scavenging," in *2010 IEEE Radio and Wireless Symposium (RWS)*, New Orleans, LA, USA, Jan. 2010, pp. 61–64.

[101] A. Technologies, "Guide to harmonic balance simulation in ADS," 2004. [Online]. Available: http://cp.literature.agilent.com/litweb/pdf/ads2004a/pdf/adshbapp.pdf

[102] A. Georgiadis, G. Andia, and A. Collado, "Rectenna design and optimization using reciprocity theory and harmonic balance analysis for electromagnetic (EM) energy harvesting," *Antennas and Wireless Propagation Letters, IEEE*, vol. 9, pp. 444–446, 2010.

[103] DigitalUK, "Digital TV switchover in the UK," Aug. 2012. [Online]. Available: www.digitaluk.co.uk

[104] I. C. on Non-Ionizing Radiation Protection, "Guidelines for limiting exposure to time- varying electric, magnetic, and electromagnetic fields (up to 300 GHz)," *Health Physics*, vol. 74, no. 4, pp. 494–522, 1998.

[105] E. C. C. E. within the European Conference of Postal and T. A. (CEPT), "Revised ECC recommendation (02)04: Measuring non-ionising electromagnetic radiation (9 kHz - 300 GHz)." Oct. 2003.

[106] Imperial College London, "London RF survey," http://londonrfsurvey.org/, Aug. 2012. [Online]. Available: http://londonrfsurvey.org/

[107] N. F. P. Group, "United kingdom frequency allocation table, issue no. 16," 2010.

[108] "Ofcom sitefinder," Jan. 2012. [Online]. Available: www.sitefinder.ofcom.org.uk

[109] R. Vyas, V. Lakafosis, M. Tentzeris, H. Nishimoto, and Y. Kawahara, "A battery-less, wireless mote for scavenging wireless power at UHF (470-570 MHz) frequencies," in *2011 IEEE Antennas and Propagation Society International Symposium and USNC/URSI National Radio Science Meeting, 3-8 July 2011*, ser. Proceedings of the 2011 IEEE Antennas and Propagation Society International Symposium and USNC/URSI National Radio Science Meeting. Piscataway, NJ, USA: IEEE, 2011, pp. 1069–72, copyright 2011, The Institution of Engineering and Technology.

[110] J. L. Volakis, *Antenna engineering handbook.* McGraw-Hill, Jun. 2007.

[111] T. Ungan and L. Reindl, "Harvesting low ambient RF-Sources for autonomous measurement systems," in *Instrumentation and Measurement Technology Conference Proceedings, 2008. IMTC 2008. IEEE*, 2008, pp. 62–65.

[112] V. Marian, C. Vollaire, J. Verdier, and B. Allard, "Potentials of an adaptive rectenna circuit," *IEEE Antennas and Wireless Propagation Letters*, vol. 10, pp. 1393–1396, 2011.

[113] J.A. Hagerty, F.B. Helmbrecht, W.H. McCalpin, R. Zane, and Z.B. Popovic, "Recycling ambient microwave energy with broad-band rectenna arrays," *Microwave Theory and Techniques, IEEE Transactions on*, vol. 52, no. 3, pp. 1014–1024, 2004.

[114] J. A. Hagerty and Z. Popovic, "Rectenna arrays for recycling statistical broadband radiation," Tech. Rep., Sep. 2003.

[115] A. Costanzo, M. Fabiani, A. Romani, D. Masotti, and V. Rizzoli, "Co-design of ultra low power RF/Microwave receivers and converters for RFID and energy harvesting applications," in *Microwave Symposium Digest (MTT), 2010 IEEE MTT-S International*, 2010, p. 1.

[116] R. R. Buted, "Zero bias detector diodes for the RF/ID market," *Hewlett Packard Journal*, vol. 46, pp. 92–94, 1995.

[117] J. McSpadden, L. Fan, and K. Chang, "Design and experiments of a high-conversion-efficiency 5.8-GHz rectenna," *Microwave Theory and Techniques, IEEE Transactions on*, vol. 46, no. 12, pp. 2053–2060, 1998.

[118] V. Marian, C. Menudier, M. Thevenot, C. Vollaire, J. Verdier, and B. Allard, "Efficient design of rectifying antennas for low power detection," in *Microwave Symposium Digest (MTT), 2011 IEEE MTT-S International*. IEEE, Jun. 2011, pp. 1–4.

[119] W. Yeoh and W. Yeoh, "Wireless power transmission (wpt) application at 2.4 ghz in common network," 2010.

[120] Avago Technologies, "HSMS-285x series datasheet," May 2009.

[121] T. Paing, E. A. Falkenstein, R. Zane, and Z. Popovic, "Custom IC for ultralow power RF energy scavenging," *IEEE Transactions on Power Electronics*, vol. 26, no. 6, pp. 1620–1626, Jun. 2011.

[122] O. O. L. GmbH, "Series 336 low current LED datasheet," 2009.

[123] A. Nimo, D. Grgic, and L. Reindl, "Ambient electromagnetic wireless energy harvesting using multiband planar antenna," in *2012 IEEE 9th International Multi-Conference on Systems, Signals and Devices (SSD), 20-23 March 2012*, ser. 2012 IEEE 9th International Multi-Conference on Systems, Signals and Devices (SSD). Piscataway, NJ, USA: IEEE, 2012, p. 6 pp.

[124] H. Takhedmit, L. Cirio, B. Merabet, B. Allard, F. Costa, C. Vollaire, and O. Picon, "A 2.45-GHz dual-diode rectenna and rectenna arrays for wireless remote supply applications," *International Journal of Microwave and Wireless Technologies*, vol. 3, no. 03, pp. 251–258, Jun. 2011.

[125] S. Vemuru, P. Singh, and M. Niamat, "Modeling impact of bypass diodes on photovoltaic cell performance under partial shading," in *2012 IEEE International Conference on Electro/Information Technology (EIT)*, May 2012, pp. 1 –5.

[126] N. Tesla, "Apparatus for transmitting electrical energy," U.S. Patent 1 119 732, 1914.

[127] S. Y. R. Hui and W. C. Ho, "A new generation of universal contactless battery charging platform for portable consumer electronic equipment," in *Power Electron. Specialists Conf., 2004. PESC 04. 2004 IEEE 35th Annual*, vol. 1, June 2004, pp. 638–644.

[128] D. Schneider, "Wireless power at a distance is still far away [electrons unplugged]," *Spectrum, IEEE*, vol. 47, no. 5, pp. 34 –39, May 2010.

[129] G. Covic, G. Elliott, O. Stielau, R. Green, and J. Boys, "The design of a contact-less energy transfer system for a people mover system," in *Proc. PowerCon 2000., Int. Conf. on Power Syst. Tech.*, vol. 1, 2000, pp. 79–84.

[130] A. Karalis, J. D. Joannopoulos, and M. Soljacic, "Efficient wireless non-radiative mid-range energy transfer," *Annals of Physics*, vol. 323, no. 1, pp. 34–48, 2008.

[131] A. Kurs, A. Karalis, R. Moffatt, J. D. Joannopoulos, P. Fisher, and M. Soljacic, "Wireless power transfer via strongly coupled magnetic resonances," *Science*, vol. 317, no. 5834, pp. 83–86, Jul. 2007.

[132] J. C. Schuder, H. E. Stephenson, and J. F. Townsend, "High-level electromagnetic energy transfer through a closed chest wall," in *IRE International Convention Record*, vol. 9, 1961, p. 119.

[133] A4WP, "Alliance for wireless power." [Online]. Available: www.a4wp.org

[134] "Wireless Power Consortium." [Online]. Available: http://www.wirelesspowerconsortium.com/

[135] C.-G. Kim, D.-H. Seo, J.-S. You, J.-H. Park, and B.-H. Cho, "Design of a contactless battery charger for cellular phone," in *Fifteenth Annual IEEE Applied Power Electronics Conference and Exposition, 2000. APEC 2000*, vol. 2, 2000, pp. 769–773 vol.2.

[136] M. Dockhorn, D. Kurschner, and R. Mecke, "Contactless power transmission with new secondary converter topology," in *Power Electronics and Motion Control Conference, 2008. EPE-PEMC 2008. 13th*, 2008, pp. 1734–1739.

[137] Y. Matsuo, O. Kondoh, and F. Nakao, "Controlling new die mechanisms for magnetic characteristics of super-large ferrite cores," *IEEE Transactions on Magnetics*, vol. 36, no. 5, pp. 3411–3414, 2000.

[138] Australian Radiation Protection and Nuclear Protection and Nuclear Safety Agency (ARPANSA), "Maximum exposure levels to radiofrequency fiĄelds 3 kHz to 300 GHz," 2002.

[139] J. Villa, J. Sallan, J. Sanz, and A. Llombart, "High-misalignment tolerant compensation topology for ICPT systems," *IEEE Trans. Ind. Electron.*, vol. 59, no. 2, pp. 945–951, Feb. 2012.

[140] J. Sallan, J. Villa, A. Llombart, and J. Sanz, "Optimal design of ICPT systems applied to electric vehicle battery charge," *IEEE Transactions on Industrial Electronics*, vol. 56, no. 6, pp. 2140–2149, 2009.

[141] "HaloIPT," Feb. 2012. [Online]. Available: http://www.haloipt.com/#n_home-intro

[142] "Qualcomm," Feb. 2012. [Online]. Available: http://www.qualcomm.com/

[143] "WiTricity Corp." Feb. 2012. [Online]. Available: http://www.witricity.com/

[144] "Delphi wireless charging system," May 2012. [Online]. Available: http://delphi.com/shared/pdf/ppd/pwrelec/wireless-charging-system.pdf

[145] A. Karalis, A. B. Kurs, R. Moffatt, J. D. Joannopoulos, P. H. Fisher, and M. Soljacic, "Power supply system and method of controlling power supply system," U.S. Patent, Sep., 2011, publication number: US 2011/0221278 A1 U.S. Classification: 307/104.

[146] A. Karalis, A. B. Kurs, A. J. Campanella, K. J. Kulikowsky, K. L. Hall, M. Soljacic, and M. P. Kesler, "Wireless energy transfer with high-q resonators using field shaping to improve k," United States of America Patent US 2 011 043 049 (A1), Feb., 2011.

[147] J. D. Joannopoulos, A. Karalis, and M. Soljacic, "Wireless energy transfer with high-q at high efficiency," Patent US8 400 018 B2, Mar., 2013, international Classification: H03H9/00.

[148] G. A. Covic and J. T. Boys, "Power demand management in inductive power transfer systems," Patent US20 120 319 479 A1, Dec., 2012, international Classification: H01F38/14; H02J3/00 U.S. Classification: H02J 5/00T.

[149] D. R. Smith, J. B. Pendry, and M. C. K. Wiltshire, "Metamaterials and negative refractive index," *Science*, vol. 305, no. 5685, pp. 788–792, Aug. 2004.

[150] J. B. Pendry, "Negative refraction makes a perfect lens," *Physical review letters*, vol. 85, no. 18, pp. 3966–3969, Oct. 2000, PMID: 11041972.

[151] J. Kim, J. Kim, S. Kong, H. Kim, I.-S. Suh, N. P. Suh, D.-H. Cho, J. Kim, and S. Ahn, "Coil design and shielding methods for a magnetic resonant wireless power transfer system," *Proceedings of the IEEE*, pp. 1–11, 2013.

[152] S. Jung, H. Lee, C. Song, J. Han, G. Jang, and W. Han, "Optimal operation plan of the on-line electric vehicle system through establishment of DC distribution system," *IEEE Transactions on Power Electronics*, pp. 1–1, 2013.

[153] R. Laouamer, M. Brunello, J. Ferrieux, O. Normand, and N. Buchheit, "A multi-resonant converter for non-contact charging with electromagnetic coupling," in *Industrial Electronics, Control and Instrumentation, 1997. IECON 97. 23rd International Conference on*, vol. 2, 1997, pp. 792–797 vol.2.

[154] Y. Lu, K. W. E. Cheng, Y. L. Kwok, K. Kwok, K. Chan, and N. Cheung, "Gapped air-cored power converter for intelligent clothing power transfer," in *7th International Conference on Power Electronics and Drive Systems, 2007. PEDS '07*, 2007, pp. 1578–1584.

[155] N. O. Sokal, "Class-E RF power amplifiers," *QEX Commun. Quart*, no. 204, pp. 9–20, Jan. 2001.

[156] F. Raab, "Effects of circuit variations on the class e tuned power amplifier," *IEEE Journal of Solid-State Circuits*, vol. 13, no. 2, pp. 239–247, 1978.

[157] Y. Jang and M. Jovanovic, "A contactless electrical energy transmission system for portable-telephone battery chargers," in *Telecommunications Energy Conference, 2000. INâĎąEC. Twenty-second International*, 2000, pp. 726–732.

[158] J. J. Casanova, Z. N. Low, and J. Lin, "Design and optimization of a Class-E amplifier for a loosely coupled planar wireless power system," *IEEE Trans. on Circuits and Syst. II: Express Briefs*, vol. 56, no. 11, pp. 830–834, Nov. 2009.

[159] T. P. Duong and J. W. Lee, "Experimental results of high-efficiency resonant coupling wireless power transfer using a variable coupling method," *IEEE Trans. Microw. Wireless Compon. Lett.*, vol. 21, no. 8, pp. 442–444, Aug. 2011.

[160] A. Karalis, A. B. Kurs, R. Moffatt, J. D. Joannopoulos, P. Fisher, and M. Soljacic, "Power Supply System and Method of Controlling Power Supply System," U.S. Patent 20 110 221 278, 2011.

[161] G. Vandevoorde and R. Puers, "Wireless energy transfer for stand-alone systems: a comparison between low and high power applicability," *Sensors and Actuators A: Physical*, vol. 92, no. 1-3, pp. 305–311, Aug. 2001.

[162] M. A. Bueno and A. K. Assis, "A new method for inductance calculations," *Journal of Physics D: Applied Physics*, vol. 28, p. 1802, 1995.

[163] F. W. Grover, *Inductance calculations: working formulas and tables.* Courier Dover Publications, Mar. 2004.

[164] J. D. Jackson, *Classical electrodynamics.* Wiley, Nov. 1975.

[165] D. C. Yates, A. S. Holmes, and A. J. Burdett, "Optimal transmission frequency for ultralow-power short-range radio links," *IEEE Trans. on Circ. and Syst. I: Regular Papers*, vol. 51, no. 7, pp. 1405–1413, Jul. 2004.

[166] C. A. Balanis, *Antenna Theory: Analysis and Design*, 3rd ed. John Wiley, 2005.

[167] G. Smith, "Radiation efficiency of electrically small multiturn loop antennas," *IEEE Transactions on Antennas and Propagation*, vol. 20, no. 5, pp. 656 – 657, Sep. 1972.

[168] S. Butterworth, "On the alternating current resistance of solenoidal coils," *Proceedings of the Royal Society of London. Series A, Containing Papers of a Mathematical and Physical Character*, vol. 107, no. 744, pp. 693–715, Apr. 1925.

[169] F. E. Terman, *Radio engineer's handbook.* McGraw-Hill Book Company, inc., 1943.

[170] A. D. Helfrick and W. D. Cooper, *Modern electronic instrumentation and measurement techniques.* Prentice Hall, 1990.

[171] L. H. Chua and D. Mirshekar-Syahkal, "Accurate and direct characterization of high-q microwave resonators using one-port measurement," *Microwave Theory and Techniques, IEEE Transactions on*, vol. 51, no. 3, pp. 978–985, 2003.

[172] D. Kajfez, "Q factor measurements, analog and digital," *University of Mississippi Dept. of Electrical Engineering, www. ee. olemiss. eduldarko/rfqmeas2b. pdf.*

[173] "Dielectric Laboratories," Apr. 2012. [Online]. Available: http://www.dilabs.com/

[174] D. Kajfez, S. Chebolu, M. Abdul-Gaffoor, and A. Kishk, "Uncertainty analysis of the transmission-type measurement of q-factor," *Microwave Theory and Techniques, IEEE Transactions on*, vol. 47, no. 3, pp. 367–371, 1999.

[175] A. Vasylchenko, Y. Schols, W. De Raedt, and G. Vandenbosch, "Challenges in full wave electromagnetic simulation of very compact planar antennas," in *Antennas and Propagation, 2007. EuCAP 2007. The Second European Conference on*, 2007, pp. 1–6.

[176] N. O. Sokal and A. D. Sokal, "Class E-A new class of high-efficiency tuned single-ended switching power amplifiers," *IEEE J. of Solid-State Circuits*, vol. 10, no. 3, pp. 168–176, Jun. 1975.

[177] S. Hinchliffe and L. Hobson, "High power class-e amplifier for high-frequency induction heating applications," *Electronics Letters*, vol. 24, no. 14, pp. 886–888, 1988.

[178] R. J. Gutmann, "Application of RF circuit design principles to distributed power converters," *IEEE Transactions on Industrial Electronics and Control Instrumentation*, vol. IECI-27, no. 3, pp. 156 –164, Aug. 1980.

[179] "Agilent N2780A/B, N2781A/B, N2782A/B, and N2783A/B current probes, user's and service guide," Agilent Technologies Inc., U.S.A., 2010.

[180] S. Rea and S. West, "Thermal radiation from finned heat sinks," *IEEE Trans. Parts, Hybrids, and Packag.*, vol. 12, no. 2, pp. 115–117, Jun. 1976.

[181] M. W. Vania, "PRF-1150 1KW 13.56 MHz Class E RF generator evaluation module," Directed Energy, Inc., Technical Note 9200-0255 Rev. 1, 2002.